

AD624320

AFWL-TR-65-117

AFWL-TR
65-117

**MEASUREMENT OF THE GRUENEISEN PARAMETER AND
THE INTERNAL ENERGY DEPENDENCE OF THE SOLID
EQUATION OF STATE FOR ALUMINUM AND TEFLON**

**D. T. Morgan, M. Rockowitz,
and A. L. Atkinson**

**Research and Advance Development Division
AVCO Corporation
Wilmington, Massachusetts**

Contract AF 29(601)-6394

TECHNICAL REPORT NO. AFWL-TR-65-117

October 1965

**AIR FORCE WEAPONS LABORATORY
Research and Technology Division
Air Force Systems Command
Kirtland Air Force Base
New Mexico**

CLEARINGHOUSE FOR FEDERAL SCIENTIFIC AND TECHNICAL INFORMATION			
Hardcopy	Microfiche		
\$4.00	\$0.75	125pp	as
ARCHIVE COPY			

Code 1

AFWL-TR-65-117

MEASUREMENT OF THE GRUENEISEN PARAMETER AND THE
INTERNAL ENERGY DEPENDENCE OF THE SOLID
EQUATION OF STATE FOR ALUMINUM AND TEFLON

D. T. Morgan, M. Rockowitz, and A. L. Atkinson

Research and Advance Development Division
AVCO Corporation
Wilmington, Massachusetts
Contract AF 29(601)-6394

TECHNICAL REPORT NO. AFWL-TR-65-117

FOREWORD

This report was prepared by the Research and Advanced Development Division, AVCO Corporation, Wilmington, Massachusetts, under Contract AF 29(601)-6394. The research was performed under Program Element 7.60.06.01D, Project 5710, Subtask 15.018, and was funded by the Defense Atomic Support Agency (DASA).

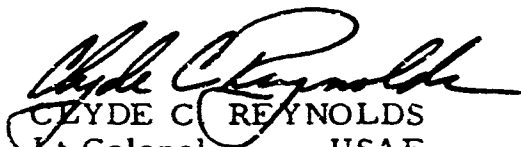
Inclusive dates of research were 1 May 1964 to 31 May 1965. The report was submitted for publication on 28 September 1965 by Lt R. J. Lawrence, Jr., AFWL (WLRP), Air Force program monitor

The authors would like to express their appreciation to the following individuals for their support and cooperation on this project: D. J. DeChristoforo, D. S. Duncklee, J. T. Smith, Dr. A. T. Stewart, and G. A. Theophanis.

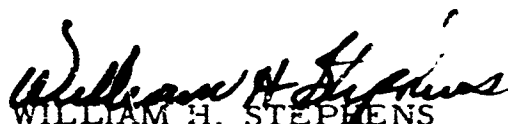
This report has been reviewed and is approved.



RAYMOND J. LAWRENCE, JR.
1Lt USAF
Project Officer



CLYDE C. REYNOLDS
Lt Colonel USAF
Chief, Physics Branch



WILLIAM H. STEPHENS
Colonel USAF
Chief, Research Division

ABSTRACT

Experimental measurements of the solid state equation of state of aluminum and Teflon, including the internal energy dependence, were made. The data for aluminum mesh well with the data of other investigators. Using the aluminum data, it was found that for initial aluminum densities of 1.36, 1.60, and 1.82 gms/cc, the thermal internal energy, E_{th} , is dependent only on the product VP_{th} where V is the specific volume and P_{th} is the thermal pressure. The Grueneisen parameter was found to be given by $100/(39.9 + 0.284 VP_{th})$ with VP_{th} in $(\text{cm}^3 \text{ kilobars})/\text{gm}$. At $VP_{th} = 0$, the Grueneisen parameter = 2.5.

The solid Hugoniot for Teflon was found to mesh well with lower pressure measurements by other investigators. The scatter in the porous Teflon samples was too large and the data were too limited to permit evaluation of the Grueneisen parameter.

CONTENTS

<u>Section</u>	<u>Page</u>
I. INTRODUCTION.....	1
1. Background	1
2. Form of Equation of State	1
II. SUMMARY	5
III. THEORY	8
1. Theoretical Basis for Method	8
2. Quantitative Relationships for Grueneisen Parameter Measurements	13
IV. DESCRIPTION OF EXPERIMENTS	21
1. Method of Generating Shock Waves in Solids	21
2. Technique of Measurement	39
3. Description of Equipment.....	47
4. Projectile Design.....	63
5. Method of Fabrication of Porous Materials	70
V. RESULTS.....	74
1. Aluminum	75
2. Teflon	80
VI. ANALYSIS OF RESULTS	88
1. Shock Velocity Versus Projectile Velocity.....	88
2. Pressure-Volume Relationships.....	88
3. Evaluation of Grueneisen Parameter.....	96
VII. CONCLUSIONS AND RECOMMENDATIONS	107
References	108
Distribution	111

ILLUSTRATIONS

<u>Figure</u>		<u>Page</u>
1	Sketch of Hugoniot for Solid and Foamed Materials ($m = \rho_0 / \rho_\infty$)	8
2	Qualitative Illustration for Hugoniot Equation of State for a Material Shock-Compressed from Foams of Different Initial Bulk Densities ($h = 1 + 2/\Gamma_0$ and $m = \rho_0 / \rho_\infty$ where ρ_∞ = bulk density of foam)	12
3	Solid Propellant Gun Used on Grueneisen Parameter Study	22
4	Schematic of Light Gas Gun	24
5	Ratios of x_0/L_f and T/d as a Function of Impact Velocity Aluminum - Aluminum ($m = 1.0$)	29
6	Ratios of x_0/L_f and T/d as a Function of Impact Velocity Aluminum - Porous Aluminum ($m = 1.50$)	30
7	Ratios of x_0/L_f and T/d as a Function of Impact Velocity Aluminum - Porous Aluminum ($m = 2.0$)	31
8	Ratios of x_0/L_f and T/d as a Function of Impact Velocity Aluminum - Teflon ($m = 1.0$)	32
9	Ratios of x_0/L_f and T/d as a Function of Impact Velocity Aluminum - Porous Teflon ($m = 1.50$)	33
10	Ratios of x_0/L_f and T/d as a Function of Impact Velocity Aluminum - Porous Teflon ($m = 2.50$)	34
11	$x - t$ Diagram for Plate Impact Experiment	36
12	Simplified Schematic of System Which Measures Impact and Shock Velocity	41
13	Plot of Relative Photomultiplier Anode Current as a Function of Projectile Displacement	44

ILLUSTRATIONS (Cont'd)

<u>Figure</u>		<u>Page</u>
14	Oscilloscope Record of Shot 107 - Aluminum on Solid Teflon ($m = 1$) Reference Time Marker Frequency is 5 MC - Sweep Speed 1 μ sec/cm	46
15	Orthogonal Shadowgraph Records of Shot 107 About 3.5 μ sec Prior to Impact - Magnification (2:1)	48
16	Grueneisen Parameter Tank Assembly - Vertical Plane ...	50
17	Grueneisen Parameter Tank Assembly - Horizontal Plane..	51
18	Photograph of Inside of Test Section Showing Target in Position in Target Holder	52
19	Photograph Showing Overall View of Vacuum Tank and Laser Optics Assembly on I-Beam	54
20	Schematic of Optical Instrumentation Used on Grueneisen Parameter Study	55
21	Block Diagram of Grueneisen Parameter Electronics	58
22	Schematic of PM 1	59
23	Schematic of Pedestal Pulser Power Supply for PM 2	61
24	Schematic of PM 2	62
25	Apparatus for Grueneisen Parameter Study	64
26	View of Photomultiplier and Slit Assembly Inside Light Tight Box	65
27	Photograph of 1-1/2 inch Projectile Used on Grueneisen Parameter Study	67
28	Schematic of 1-1/2 inch Projectile Used on Grueneisen Parameter Study	68
29	Schematics of 0.060 Caliber Projectiles Used on Grueneisen Parameter Study	69

ILLUSTRATIONS (Concl'd)

<u>Figure</u>		<u>Page</u>
30	Photograph of 1-1/2 inch Diameter Target Samples Used on Grueneisen Parameter Study	73
31	Shock Velocity versus Projectile Impact Velocity for Al - Al, $m = 1$	76
32	Shock Velocity versus Projectile Impact Velocity for Al 1100 on Porous Al, $m = 1.5$	77
33	Shock Velocity versus Projectile Impact Velocity for Al 1100 on Porous Al, $m = 2.02$	78
34	Shock Velocity versus Projectile Impact Velocity for Al 1100 on Teflon, $m = 1.0$	82
35	Shock Velocity versus Projectile Impact Velocity for Al 1100 on Porous Teflon, $m = 1.42$	83
36	Shock Velocity versus Projectile Impact Velocity for Al 1100 on Porous Teflon, $m = 2.23$	84
37	Shock Velocity versus Projectile Velocity for Aluminum ...	89
38	Shock Velocity versus Projectile Velocity for Teflon	90
39	Pressure - Volume Relationship for Aluminum	95
40	Pressure - Volume Relationship for Teflon	97
41	Effective Grueneisen Parameter for Aluminum	100
42	Internal Energy as Function of Pressure for Aluminum	101
43	Thermal Internal Energy: E_{th} , versus VP_{th} for Aluminum ..	103
44	Grueneisen Parameter as Function of Thermal Internal Energy for Aluminum	104
45	Effective Grueneisen Parameter for Teflon	106

TABLES

<u>Table</u>		<u>Page</u>
I	Equation of State Constants	28
II	Summary of Data—Aluminum on Aluminum	75
III	Summary of Data—Aluminum on Teflon	81
IV	Linear Equations Giving Shock Velocity as Function of Projectile Velocity	91
V	Calculated Shock Parameters for Aluminum	93
VI	Calculated Shock Parameters for Teflon	94

ABBREVIATIONS AND SYMBOLS

C_{ot}	Longitudinal wave velocity behind the shock front, km/sec
C_v	Specific heat at constant volume, (ergs/gm - °K)
E	Specific internal energy, ergs/gm
E_o	Specific internal energy along the 0°K isotherm
E_t	Target internal energy
E_{th}	Thermal component of internal energy
L_f	Projectile thickness, cm
P	Pressure, dynes/cm ²
P_f	Projectile pressure
P_H	Hugoniot pressure
P_o	Pressure along the 0°K isotherm
P_t	Target pressure
P_{th}	Thermal component of target pressure
T	Target thickness, cm
U'	Velocity of shock front with respect to material ahead of shock, km/sec
U_f	Projectile velocity
v	Specific volume, cm ³ /gm
v_o	Specific volume along the 0°K isotherm
d	Projectile diameter, cm
h	$1 + 2/\Gamma_o$
k_θ	Isothermal bulk compressibility, (cm ² /dyne)

ABBREVIATIONS AND SYMBOLS (Cont'd)

m	Ratio of solid to porous material densities
t	Time, sec
u'	Velocity of shocked material with respect to material ahead of shock, km/sec
u_{1f}	Velocity of projectile shock with respect to the undisturbed projectile material, km/sec
u_{1t}	Velocity of target shock with respect to the undisturbed target material
u_{sf}	Velocity of shocked projectile material with respect to the projectile shock
u_{st}	Velocity of shocked material with respect to the target shock, km/sec
x	Distance, cm
x_0	Distance in target at which rarefaction from projectile overtakes the shock front
Γ	Grueneisen parameter, dimensionless
Γ_0	Grueneisen constant
θ	Temperature, °K
β	Volumetric coefficient of thermal expansion (°K ⁻¹)
μ	$\rho/\rho_0 - 1$
μ_f	$\rho_f/\rho_{of} - 1$
μ_t	ρ_t/ρ_{ot}
ρ	Density of shocked material, gms/cm ³
ρ_f	Shocked projectile density
ρ_0	Initial solid material density

ABBREVIATION AND SYMBOLS (Concl'd)

ρ_{of}	Initial projectile density
ρ_{ot}	Initial target density
ρ_t	Shocked target density
ρ_{∞}	Initial porous material density
τ	Time for rarefaction in target to reach target shock, sec

SECTION I

INTRODUCTION

1. Background

Recent advances in nuclear weapon technology have increased the importance of the internal energy dependence of the solid-state equation of state in vulnerability analyses and it has therefore become necessary to determine this dependence much more exactly than has been necessary in the past. Accordingly, AFWL has sponsored two concurrent programs, one at the Stanford Research Institute (SRI) and the other at the Avco Research and Advanced Development Division (Avco RAD), for determination of the internal energy dependence of the solid-state equation of state of selected materials. This report presents the results obtained with Teflon and aluminum at Avco RAD using a technique first developed by Krupnikov (reference 1) and Kormor (reference 2) and other Russian workers. Briefly, the technique involves Hugoniot measurements in materials by impacting porous and solid specimens of the material with a hypervelocity projectile. The internal energy in the shock-compressed material is varied over a wide range by using open-celled porous samples of variable density (as well as the solid material) as the target. The basic theory of the technique is explained in more detail in Section III and the experimental apparatus is described in Section IV. The results for aluminum and Teflon are presented in Section V and discussed in Section VI.

2. Form of Solid-State Equation of State

At pressures considerably greater than the yield strength of the material, which is the region of interest in this work, the stresses in the shock-compressed material should be isotropic, that is, the same in all directions. Assuming that thermal equilibrium exists in the shock-compressed material, the usual thermodynamic functions can be applied to the solid material at high

pressures, namely:

P = Compressive stress in material under conditions where the stresses are isotropic, that is, the same in all directions (dyne/cm²).

V = Specific volume (cm³/gm)

E = Specific internal energy (ergs/gm)

θ = Temperature (°K).

Only three of these properties are required to characterize the state of material; for example, E and θ are related as follows:

$$C_V(V, \theta) = \left(\frac{\partial E(V, \theta)}{\partial \theta} \right)_V \quad (1)$$

where $C_V(V, \theta)$ is the heat capacity of the material at constant volume ergs/(gm-°K). In this report, P , V , and E are used as the variables.

An important parameter in the equation of state of solid materials is the Grueneisen parameter defined as:

$$\Gamma(V, E) = V \left(\frac{\partial P(V, E)}{\partial E} \right)_V = \frac{V\beta}{C_V k_\theta} \quad (2)$$

where

$\Gamma(V, E)$ = Grueneisen parameter as a function of specific volume and specific internal energy (dimensionless)

$P(V, E)$ = Pressure as a function of volume and internal energy (dyne/cm²).

$\beta = \frac{1}{V} \left(\frac{\partial V}{\partial \theta} \right)_P$ = Volumetric coefficient of thermal expansion (°K⁻¹)

$k_\theta = -V \left(\frac{\partial P}{\partial V} \right)_\theta$ = Isothermal bulk compressibility (cm²/dyne).

On a microscopic scale, the internal energy of a material and the pressure corresponding to that energy can be split into two separate contributions, the

potential internal energy and potential pressure due to changes in spacing of the atoms in their lattice and the thermal internal energy and the thermal pressure due to vibrations of the atoms in their lattice. The zero degree (0°K) $P_0 - V_0 - E_0$ isotherm represents the potential contribution only since no thermal contribution is present at 0°K . The thermal components of internal energy and pressure can thus be written as:

$$E_{th}(V, P_{th}) = E(V, P) - E_0(V) \quad (3)$$

$$P_{th}(V, E_{th}) = P(V, E) - P_0(V) \quad (4)$$

where

E_{th} = Thermal component of internal energy, ergs/gm

$E_0(V)$ = Specific internal energy at volume V and a temperature of 0°K , ergs/gm

P_{th} = Thermal component of pressure, dynes/cm²

$P_0(V)$ = Pressure at a volume V and temperature of 0°K .

With these definitions, equation (2) can also be written as:

$$\Gamma(V, E) = \Gamma(V, E_{th}) = V \left(\frac{\partial P_{th}(V, E_{th})}{\partial E_{th}} \right)_V \quad (5)$$

This expression can be integrated at constant volume to give the following expression for the pressure:

$$\int_0^{P(V, E) - P_0(V)} dP_{th}(V, E_{th}) = \frac{1}{V} \int_0^{E(V, P) - E_0(V)} \Gamma(V, E_{th}) dE_{th} \quad (6)$$

or

$$P(V, E) = P_0(V) + \frac{1}{V} \int_0^{E(V, P) - E_0(V)} \Gamma(V, E_{th}) dE_{th} \quad (7)$$

For calculational purposes, $P_0(V)$ can be represented as a polynomial expansion in volume so that the equation-of-state, using a cubic expansion for $P_0(V)$, appears as follows:

$$P(V, E) = P_0 + C\mu + D\mu^2 + S\mu^3 + \rho_0(1 + \mu) \int_0^{E(V, P) - E_0(V)} \Gamma(V, E_{th}) dE_{th} \quad (8)$$

where

$$\mu = (\rho/\rho_0) - 1$$

$$\rho_0 = \frac{1}{V_0} = \text{Density of material at zero } ^\circ\text{K and } P_0, \text{ the ambient pressure, gm/cm}^3$$

C , D , and S = Empirically determined constants (dyne/cm²).

Assuming $\Gamma(V, E)$ is known as a function of V and E_{th} , and the zero $^\circ\text{K}$ isotherm is known, this relation permits calculation of the pressure in the solid corresponding to a given volume, V , and given total internal energy E . It was the purpose of this project to determine the solid-state equation of state including internal energy dependence for Teflon and aluminum.

SECTION II

SUMMARY

Experimental measurements of the solid state equation of state of aluminum and Teflon, including the internal energy dependence, were made. The experimental technique involved planar impact of a high velocity flat-faced projectile onto solid and porous targets of each material. The use of measurements on porous samples with varying porosities as well as on the solid material is a convenient method of varying the internal energy in the compressed material at a given pressure over a wide range and thus determining the internal energy dependence of the equation of state. For each impact, the projectile velocity and shock velocity in the target were measured from which the pressure, volume, and internal energy in the shock-compressed material can be calculated using the Rankine-Hugoniot relations.

The projectiles were accelerated by means of a powder gun for low velocities (1 to 2 km/sec) and by a light gas gun for high velocities (>2 km/sec). The projectile velocity range covered in the present work was from approximately 1 up to 3 km/sec. The target was held about 1/2 inch in front of the gun barrel end inside a vacuum chamber to eliminate air cushion effects. The projectile and shock velocities were measured using a laser-photomultiplier arrangement. For the projectile velocity measurements, the laser beam was swept past two slits on a photomultiplier by reflection from the projectile face, thus establishing the time required to travel a predetermined distance. The moment of impact was also measured by monitoring the impact flash on the photomultiplier, providing a second projectile velocity measurement. For the shock velocity measurement, a second laser beam was reflected from the rear surface of the target onto the edge of a slit in a second photomultiplier so that very slight movement of the surface swept the beam past the slit. The measured impact time and time of shock arrival together with the target thickness thus provided the shock velocity. To check planarity of impact, two orthogonal Kerr cell shadowgraphs were taken just prior to impact.

Measurements for aluminum were made at Avco RAD on the solid material and on porous materials with porosities of $m = 1.50$ and 2.02 ($m = \text{normal solid density divided by the bulk density of the porous material}$). The range of pressures covered was 127 to 263 kilobars for solid aluminum, 65 to 173 kilobars for a porosity of 1.50, and 47 to 129 kilobars for a porosity of 2.02; a total of 18 data points were obtained. The data were plotted on a pressure versus volume plot and on an internal energy versus pressure plot along with the higher pressure data of SRI which included data at porosities of 1.40, 1.70 and 2.0. The two sets of data meshed very well and appeared to be consistent; the solid Hugoniot data meshed well with Soviet measurements. Using the zero degree $P_0 - V_0 - E_0$ isotherm, the pressure and internal energy due to thermal vibrations alone were computed for porosities of 1.50, 1.70, and 2.02. For these porosities it was found that the thermal internal energy, E_{th} , was a function of VP_{th} alone and could be represented by the equation:

$$E_{th} = 39.9 (VP_{th}) + 0.142 (VP_{th})^2 \quad (9)$$

where E_{th} is in joules/gm and VP_{th} is in $\frac{\text{cm}^3 \text{ kilobar}}{\text{gm}}$. From this relation, the Grueneisen parameter is given by:

$$\Gamma = v \left(\frac{\partial P_{th}}{\partial E_{th}} \right)_v = \frac{100}{39.9 + 0.284 VP_{th}} \quad (10)$$

It is apparent that the Grueneisen parameter is thus a function of the thermal internal energy, E_{th} , alone. For $VP_{th} = \text{zero}$, $\Gamma = 2.5$.

Data obtained by SRI at a porosity of 1.40 did not agree with equation (10), and this suggests the need for additional data on aluminum at this porosity.

Measurements for Teflon were made on the solid material and on porous material with porosities of 1.42 and 2.23. The range of pressures covered was 67 to 198 kilobars for the solid material, 58 to 132 kilobars for a porosity of 1.42, and 34 to 90 kilobars for a porosity of 2.23; a total of 16 data points were obtained. For the solid material, the data were compared with previous measurements by other investigators at lower pressures. The previous data

meshed well with the Avco RAD data so that a smooth curve representing the solid-state Hugoniot could be drawn through all the data. The scatter of the data for the porous samples was very large, particularly for the most porous material ($m = 2.23$). As a result, more data must be obtained before any definite conclusions regarding the internal energy dependence of the equation of state of Teflon can be made.

SECTION III

THEORY

1. Theoretical Basis of Method

Measurement of the Grueneisen constant is essentially a measurement of the P-V-E relationship of the material from which the Grueneisen constant can be calculated over the range of conditions covered in the experiment. Measurements of the P-V relationship of the shock-compressed material behind a shock front can be made using techniques which have been developed in the extensive experimentation of this type performed on solid materials (reference 3). The additional feature in this work is the use of similar measurements on foamed samples with different porosities (as well as on the solid material) as a convenient method of varying the internal energy of the compressed material behind the shock front over a wide range.

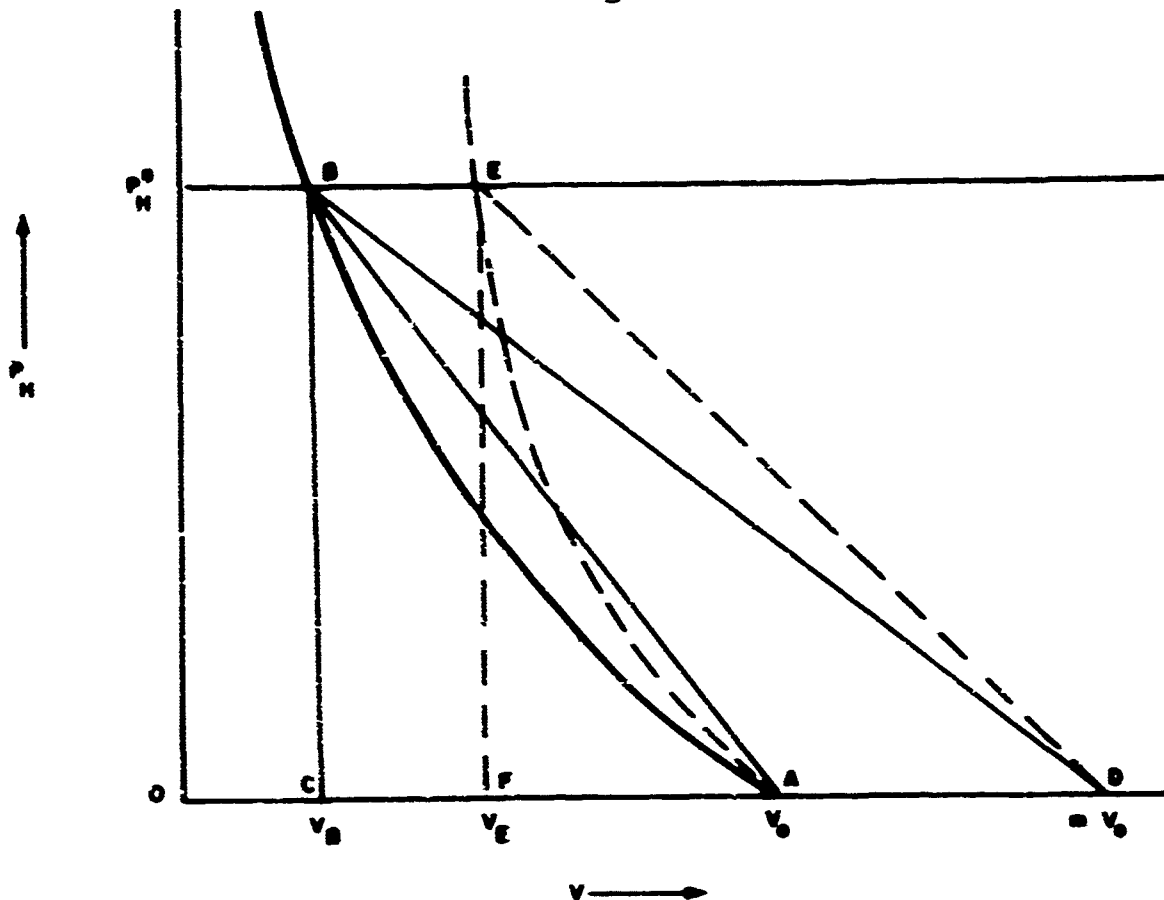


Figure 1. Sketch of Hugoniot for Solid and Foamed Materials ($\gamma = \rho_0 / \rho_c$)

Consider the sketch of figure 1 representing the Hugoniot equation of state where $v_0 = 1/\rho_0$ is the specific volume of the nonporous material at zero pressure ($P_0 = 0$) and the reference temperature T_0 . The Rankine-Hugoniot relations show that the internal energy in the shocked state at B relative to the internal energy at $P=0$ and $V=v_0$ is:

$$E = 1/2 P_H^B (v_0 - v_B) \quad (11)$$

This energy is thus represented by the area under the triangle ABC in the sketch.

Suppose now that a foamed sample of the same material with a volume mv_0 (with crushing strength $< P_H^B$) where $m = \rho_0 / \rho_\infty$ and ρ_∞ is the bulk density of the foam. The internal energy in the shocked material in this case is:

$$E = 1/2 P_H^B (mv_0 - v_E) \quad (12)$$

where v_E represents the volume corresponding to the pressure P_H^B for a sample with the initial porosity m . If v in the compressed material were at v_B , it is obvious that the internal energy, represented in this case by the area DBC, would be much greater than that obtained when the material is shocked to P_H^B starting from the normal, nonporous state. The volume for a sample shocked from the foamed state will thus be greater than that when shocked from the nonporous state due to the larger thermal energy in the shocked material and, for a porosity m , the Hugoniot will follow the dotted curve AE. The internal energy in the material shocked from the porous state to P_H^B is thus:

$$E = 1/2 P_H^B (mv_0 - v_E) \quad (13)$$

or the area of the triangle DEF. The larger the porosity (or m), the greater will be the internal energy relative to the state shocked from the solid, nonporous state.

To give a better idea of the variation in the Hugoniot equation of state which can be attained in this manner, it is useful to consider the idealized

case where the Gruneisen parameter is constant . The Hugoniot equation of state can be written as follows:

$$P_H(V) = P_o(V) + \rho \Gamma_o E \quad (14)$$

$$E = \frac{1}{2} P_H (mV_o - V) \quad (15)$$

Substitution of equation (15) into (14) gives:

$$P_H(V) = \frac{P_o(V)}{1 - \frac{\Gamma_o}{2} \left(\frac{mV_o - V}{V} \right)} \quad (16)$$

Solution of this equation for V gives:

$$V = mV_o \left[\frac{\Gamma_o P_H(V)}{P_H(V) [\Gamma_o + 2] - P_o(V)} \right] \quad (17)$$

Now, from this last equation, when $V = V_o$ (where $P_o(V) = \text{zero}$), $P_H(V)$ cancels out of the equation giving:

$$V = mV_o \left(\frac{\Gamma_o}{\Gamma_o + 2} \right) \quad (18)$$

Thus, the condition for $V = V_o$ for any Hugoniot pressure P_H is:

$$1 = m \frac{\Gamma_o}{\Gamma_o + 2} \quad \text{or} \quad m = 1 + \frac{2}{\Gamma_o} \quad (19)$$

In other words, compression of a foam with porosity $m = 1 + \frac{2}{\Gamma_o}$ to any pressure results in a volume V_o in the compressed state irrespective of the pressure obtained in the compressed state, and the Hugoniot equation of state for this condition is just a vertical straight line from V_o on a P - V plot.

Now, define this value of m as h , that is,

$$h = 1 + \frac{2}{\Gamma_o} \quad \text{or} \quad \Gamma_o = \frac{2}{h - 1} \quad (20)$$

Substitution in equation (17) gives:

$$V = mV_o \left[\frac{\left(\frac{2}{h-1}\right) P_H(V)}{\left(\frac{2h}{h-1}\right) P_H(V) - 2 P_o(V)} \right] \quad (21)$$

The limiting value of V as $P_H \rightarrow \infty$ can be derived from this equation:

$$\begin{aligned} \lim_{P_H \rightarrow \infty} V &= \lim_{P_H \rightarrow \infty} mV_o \left[\frac{\left(\frac{2}{h-1}\right)}{\left(\frac{2h}{h-1}\right) - \frac{2 P_o(V)}{P_H(V)}} \right] \\ &= \frac{m}{h} V_o \end{aligned} \quad (22)$$

Thus, for a given porosity foam, the limiting volume obtained after compression to infinite pressure is $\frac{m}{h}V_o$.

The properties derived above for a constant Grueneisen parameter are illustrated qualitatively in figure 2. It will be noticed that for any pressure:

$$\begin{aligned} m < h & \quad V < V_o \\ m = h & \quad V = V_o \\ m > h & \quad V > V_o \end{aligned} \quad (23)$$

For a variable Grueneisen parameter, the curve will be similar to the dotted curve of figure 2, sketched for the case where $m > h$ at low pressures. The limiting volumes at infinite pressure are also illustrated.

The use of Hugoniot measurements on foamed samples of a material at several porosities is thus a convenient method of determining the $P - V - E$ relationship over a large range of internal energies which cannot be obtained in any other way.

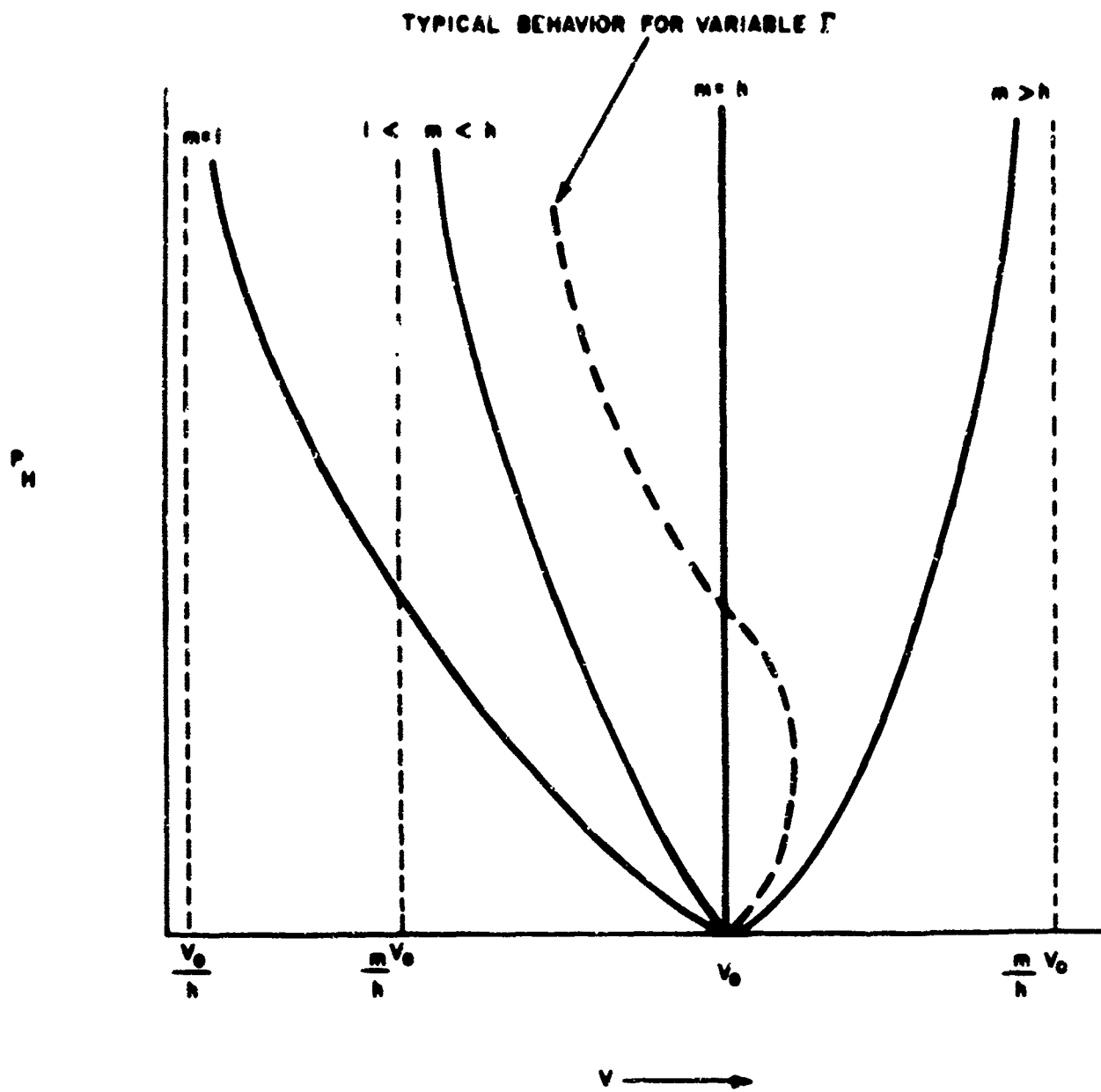
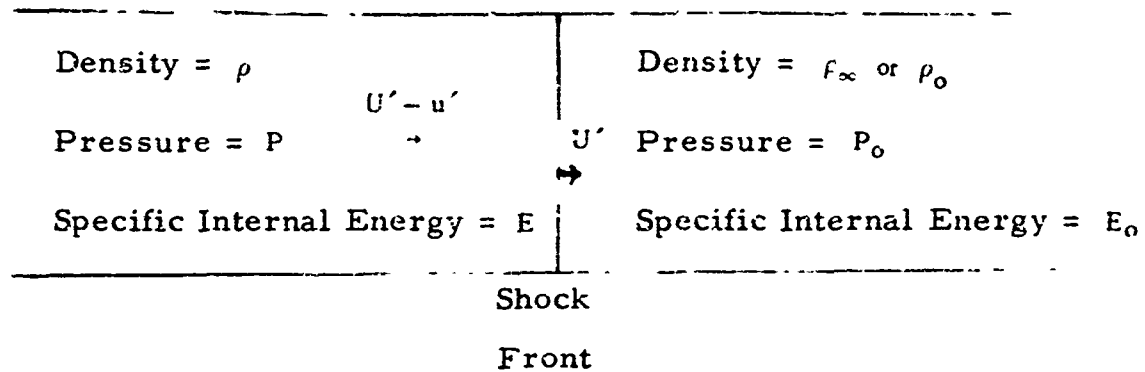


Figure 2. Qualitative Illustration for Hugoniot Equation of State for a Material Shock-Compressed from Foams of Different Initial Bulk Densities
 ($h = 1 + 2/\Gamma_0$ and $m = \rho_0/\rho_\infty$ where ρ_∞ = Bulk Density of Foam)

2. Quantitative Relationships for Grueneisen Parameter Measurement

a. Equations for Measurement of P-V-E Relationship

Consider the following sketch of the one-dimensional propagation of a shock wave through a foamed or solid material with the reference axis at rest with respect to the shock front:



For a foamed material, the bulk density of the uncompressed foam is ρ_∞ ; for compression of a solid material, the density of the uncompressed material is identical with ρ_0 , the normal density of the material at a pressure P_0 . U' represents the shock velocity relative to the material ahead of the shock front, and u' represents the material velocity in the shocked region with respect to a fixed coordinate system.

If the following assumptions are valid, then the Rankine-Hugoniot relations, including the energy conservation equation, apply to shock compression of the foamed and solid materials:

- (1) The specific internal energy (ergs/gm) of the material at zero pressure is the same in the foam as in the solid material.
- (2) The compressive strength of the foam is negligible; that is, a very small stress collapses the foam to its normal density.
- (3) The shock front must be narrow enough so that the compression is essentially instantaneous, or, if the shock front does have a finite thickness, the wave must be time invariant, that is, the shock pressure and shape must not change as it propagates through the material.

(4) The high stress states immediately behind the steep stress profile are hydrostatic.

(5) The states immediately behind the steep stress profile are in thermodynamic equilibrium.

The first assumption should be an excellent one for all solid materials. The second assumption can be met by constructing foams which collapse easily to the solid state at normal density, by performing the tests on open-cell foams which are impacted in a vacuum to eliminate the effect of trapped gases, and by performing measurements at shock pressures which are much greater than the crushing strength of the foam. The third condition is met (1) by experimentally ensuring that a rarefaction wave does not affect the shock during the measurement, thus ensuring a time-invariant shock front, and (2) by making the target macro-structure small to prevent appreciable spreading of the shock front. Condition (4) is fulfilled, provided the pressure is above the limit where the shear rigidity of the material contributes to the stresses and providing the material is homogeneous and isotropic. The fifth condition has been studied by Poczatek (reference 4) and Zener (reference 5) with the conclusion that the time required to achieve thermal equilibrium behind a shock front is on the order of 10^{-12} second for most materials.

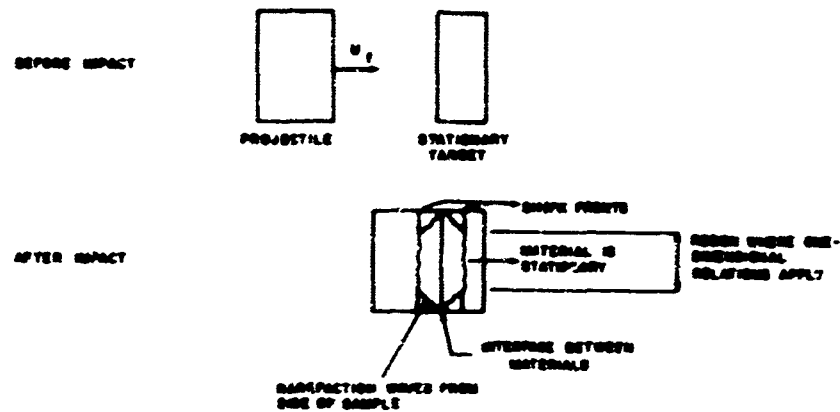
Thus, it is seen that the necessary conditions are all fulfilled and that the Rankine-Hugoniot relations apply to the case of shock compression of foamed materials as well as solid materials. These relations, taking P_0 and E_0 to be zero, are:

$$\text{Continuity:} \quad \rho (U' - u') = \rho_{\infty} U' \quad (24a)$$

$$\text{Force balance:} \quad P + \rho (U' - u')^2 = \rho_{\infty} (U')^2 \quad (24b)$$

$$\text{Energy balance:} \quad E + P/\rho + 1/2 (U' - u')^2 = 1/2 (U')^2 \quad (24c)$$

The required equations and measurements for experimental determination of the P-V-E relationship of a material will now be derived by extending the work of Bade (reference 6) for compression of solid materials by plate impact to the case of compression of foams. Consider the following sketch illustrating the impact of the hypervelocity projectile on a target made of the sample material.



The impact creates a pair of shock waves, one advancing into the target, the other traveling back into the flyer plate. The shock motion will be one-dimensional in those regions where rarefactions from the sides of the sample have not occurred. The equations to be used are based on one-dimensional propagation of the shock waves.

Let:

- U_f = velocity of projectile just before impact (km/sec)
- u_{1t} = velocity of target shock with respect to the undisturbed target material (km/sec) = U'
- u_{st} = velocity of shocked target material with respect to the target shock (km/sec) = $U' - u'$
- u_{1f} = velocity of projectile shock with respect to the undisturbed projectile material (km/sec)

u_{sf} = velocity of shocked projectile material with respect to the projectile shock (km/sec)

Thus, for the target, which can initially be either a foamed or solid material, equations (24) can be converted to the form:

$$m(1 + \mu_t) u_{st} = u_{lt} \quad (25a)$$

$$P_t + \rho_{ot}(1 + \mu_t) u_{st}^2 = \frac{1}{m} \rho_{ot} u_{lt}^2 \quad (25b)$$

$$E_t = \frac{P_t}{\rho_{ot}(1 + \mu_t)} + \frac{1}{2} u_{st}^2 = \frac{1}{2} u_{lt}^2 \quad (25c)$$

For the projectile which will not be foamed:

$$(1 + \mu_f) u_{sf} = u_{lf} \quad (26a)$$

$$P_f + \rho_{of}(1 + \mu_f) u_{sf}^2 = \rho_{of} u_{lf}^2 \quad (26b)$$

Boundary conditions at the contact surface between the projectile and target are continuity of pressure and velocity:

$$P_t = P_f \quad (27a)$$

$$u_{lt} - u_{st} = u_{sf} - u_{lf} = U_f \quad (27b)$$

It will now be assumed that the Hugoniot equation of state of the projectile is known and will be used as a known input into the experiment.

The familiar form of the Hugoniot equation of state is,

$$P_f = A\mu_f + B\mu_f^2 + F\mu_f^3 \quad (28)$$

Equations (25a) through (28) represent eight equations with the 10 unknowns as follows:

$$\mu_t, u_{st}, u_{lt}, P_t, E_t$$

$$\mu_f, u_{sf}, u_{lf}, P_f, U_f$$

Known quantities are:

$$m, \rho_o, \rho_o f, A, B, F$$

Thus, two quantities must be determined experimentally to provide a closed solution for all of the unknowns. A convenient pair of variables to measure experimentally are the projectile velocity at impact U_f and the shock velocity in the target u_{lt} . The equations will now be solved assuming U_f and u_{lt} are known from experimental measurements.

Let:

$$P_t = P_f = P \quad (29a)$$

$$P = A\mu_f h_f(\mu_f),$$

where

$$h_f(\mu_f) = 1 + \frac{B}{A} \mu_f + \frac{F}{A} \mu_f^2 \quad (29b)$$

Now eliminating P from (25b) and (26b),

$$-\rho_o t (1 + \mu_t) u_{st}^2 + \frac{1}{m} \rho_o t u_{lt}^2 = -\rho_o f (1 + \mu_f) u_{sf}^2 + \rho_o f u_{lf}^2 \quad (30a)$$

Substituting (29b) into (26b),

$$\rho_o f u_{lf}^2 - \rho_o f (1 + \mu_f) u_{sf}^2 = A\mu_f h_f(\mu_f) \quad (30b)$$

Equations (25a) and (26a) can be used to eliminate u_{st} and u_{sf} from equations (27b), (30a), and (30b):

$$U_f = u_{lt} \left(1 - \frac{1}{m(1 + \mu_t)} \right) + u_{lf} \left(\frac{\mu_f}{1 + \mu_f} \right) \quad (31a)$$

$$\frac{1}{m} \rho_{ot} u_{1t}^2 \left[1 - \frac{1}{m(1+\mu_t)} \right] = \rho_{of} u_{1f}^2 \left[\frac{\mu_f}{1+\mu_f} \right] \quad (31b)$$

$$\rho_{of} u_{1f}^2 = A(1+\mu_f) h_f(\mu_f) \quad (31c)$$

Elimination of u_{1f} from equation (31a) and (31b) by (31c) gives:

$$U_f = u_{1t} \left(1 - \frac{1}{m(1+\mu_t)} \right) + \mu_f \sqrt{\frac{A h_f(\mu_f)}{\rho_{of}(1+\mu_f)}} \quad (32a)$$

$$\frac{1}{m} \rho_{ot} u_{1t}^2 \left[1 - \frac{1}{m(1+\mu_t)} \right] = A \mu_f h_f(\mu_f) \quad (32b)$$

Elimination of $\left(1 - \frac{1}{m(1+\mu_t)} \right)$ from equation (32a) by (32b) gives:

$$U_f = \frac{m}{\rho_{ot} u_{1t}} A \mu_f h_f(\mu_f) + \mu_f \sqrt{\frac{A h_f(\mu_f)}{\rho_{of}(1+\mu_f)}} \quad (33a)$$

With U_f and u_{1t} known, solution for μ_f can be made by a trial and error procedure from equation (33a). Once μ_f is known, the other quantities characterizing the motion of the two shock waves produced by the plate impact can be explicitly calculated. Specifically:

$$u_{1f} = \sqrt{\frac{A(1+\mu_f) h_f(\mu_f)}{\rho_{of}}} \quad (33b)$$

$$\mu_t = \frac{1}{m \left[1 - m \frac{\rho_{of} u_{1f}^2}{\rho_{ot} u_{1t}^2} \frac{\mu_f}{1+\mu_f} \right]} - 1 \quad (33c)$$

$$u_{st} = \frac{u_{lt}}{m(1 - \mu_t)} \quad (33d)$$

$$u_{sf} = \frac{u_{lf}}{1 + \mu_f} \quad (33e)$$

$$P = \rho_{ot} \left[\frac{1}{m} u_{lt}^2 - (1 + \mu_t) u_{st}^2 \right] \quad (33f)$$

$$= A\mu_f h_f(\mu_f)$$

$$\begin{aligned} E_t &= \frac{1}{2} \left[u_{lt}^2 - u_{st}^2 \right] - \frac{P_t}{\rho_{ot}(1 - \mu_t)} \\ &= \frac{1}{2} \frac{P}{\rho_{ot}} \left(\frac{m(1 - \mu_t) - 1}{1 + \mu_t} \right) \end{aligned} \quad (33g)$$

Measurement of U_f and u_{lt} thus permits determination of the desired quantities, namely P , μ_t , and E_t .

It should be noted that the above relations become much simpler if the target and projectile are the same material and the target is nonporous. In this case, the relations for determining the pressure and compression from the measured projectile and shock velocities become:

$$P = \frac{1}{2} \rho_o u_{lt} U_f \quad (33h)$$

$$\mu = \frac{U_f}{2 u_{lt}} \frac{1}{1 - \frac{U_f}{u_{lt}}} \quad (33i)$$

In the experiment performed, 1100 aluminum was used as the projectile material, and its Hugoniot equation of state was determined experimentally.

SECTION IV

DESCRIPTION OF EXPERIMENT

1. Method of Generating One-Dimensional Shock Waves in Solids

In order to generate a one-dimensional shock wave in the solid target, flat-faced cylindrical projectiles were launched against flat-faced cylindrical discs, using both a solid propellant gun and a light gas gun. The region of application for each launching device is a function of the efflux velocity of the gas, i. e., the transient centered expansion velocity into a vacuum of the gas acting on the base of the projectile. The efflux velocity of a gas is an inverse function of the molecular weight of the gas, and typically for nitro-cellulose powders (molecular weight about 25 gms/mole) the practical limit of efflux velocity has been observed to be in the neighborhood of 3.00 km/sec (reference 8). On the other hand, using either hydrogen or helium (molecular weights 2 and 4 respectively), the practical limit of efflux velocity is in the neighborhood of 9.00 km/sec (reference 8). Thus for impact velocities up to 2.5 km/sec, the solid propellant gun was used, and for velocities above this value, the light gas gun using hydrogen was utilized as the launching device. This section will describe in detail both guns used in the study, along with a description of the method used to generate projectile and target design requirements, namely the minimum projectile and maximum target thickness such that no rarefactions influence the process.

a. Solid Propellant Gun for the Lower Velocities

The solid propellant gun, commonly referred to as a powder gun, utilizes a high explosive powder which is converted to a high pressure gas in a combustion chamber. The gas is constrained to the chamber volume by a shear disc which is an integral part of the projectile to be launched. When the pressure reaches the shear-disc rupture pressure, the projectile is accelerated down a launch tube. Figure 3 is a schematic

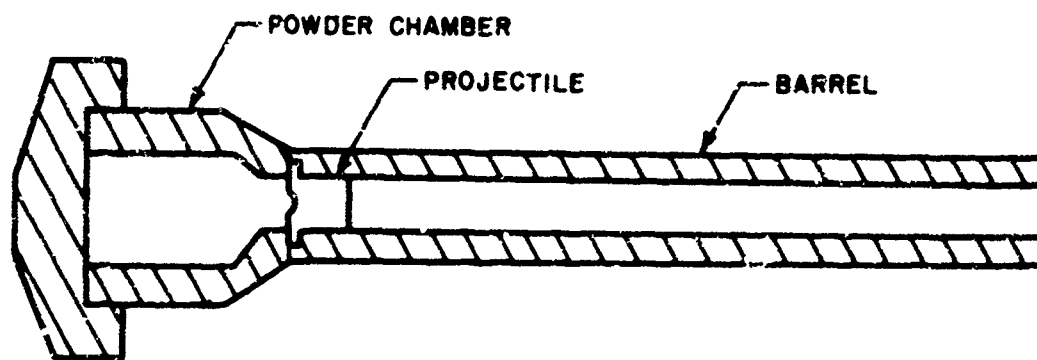


Figure 3. Solid Propellant Gun Used on Grueneisen Parameter Study

of the powder gun. Two sizes of bores were used for the low velocity firings. The breech and pump tube sections of the 0.060 caliber light gas gun were used as the combustion chamber and launch tube of a 1 1/2 inch diameter powder gun. The launch tube was 85 inches long. Utilizing a powder charge of 185 gms of powder, a maximum velocity of about 1.68 km/sec was achieved. By modifying the combustion chamber, and utilizing a 0.060 caliber launch tube (diameter 0.590 inch), the 1 1/2 inch powder gun was converted to a 0.060 caliber powder gun which proved capable of launching projectiles to about 2.29 km/sec. The length of the launch tube was 6 ft.

b. Light Gas Gun for High Velocities

The light gas gun is a two-stage gun utilizing a solid propellant to launch a piston, which in turn compresses a light gas such as hydrogen or helium to a high pressure and temperature. The projectile is separated from the high pressure reservoir by a shear disc, which eventually ruptures, allowing the gas to accelerate the projectile to high velocities. Figure 4 is a schematic of the gun used in this experiment.

There has been a good deal of work (references 8 and 9) done on analyzing the interior ballistics of light gas guns, and the subject will not be discussed here. For most of the firings made in this program, the gas used was hydrogen with helium used later in the program; the initial gas pressure was varied between 300 to 500 psi. The piston was a three-piece cylinder having a total mass of 660 gms, consisting of polyethylene, steel, and polyethylene in that order, as the three elements of the piston. The piston was accelerated to subsonic velocities such that the gas compression can be considered to be adiabatic. The shear disc used was an integral part of the projectile and this will be discussed more fully later in the report.

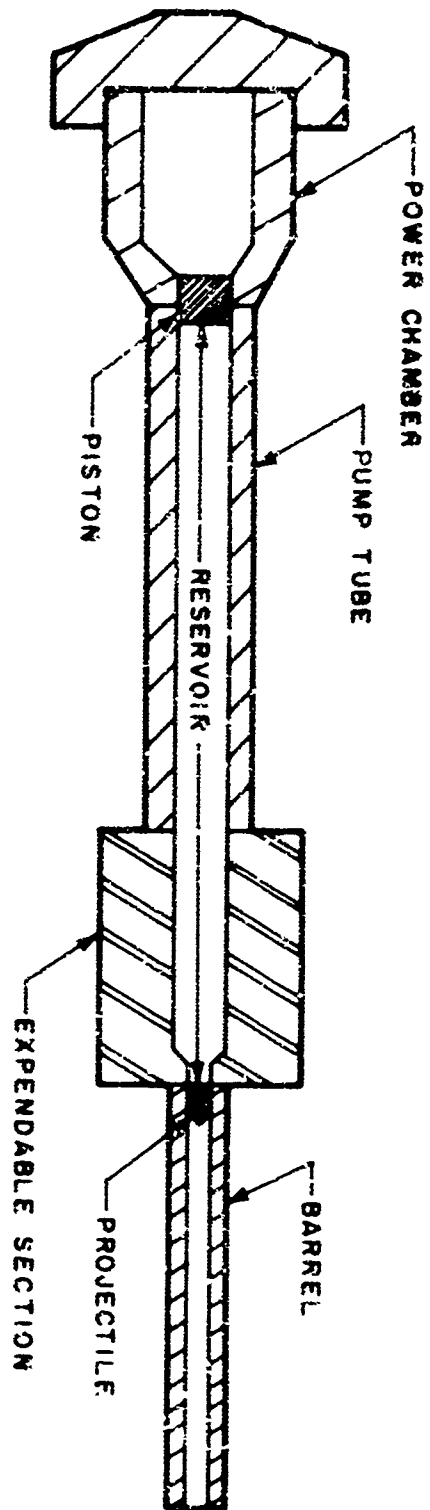
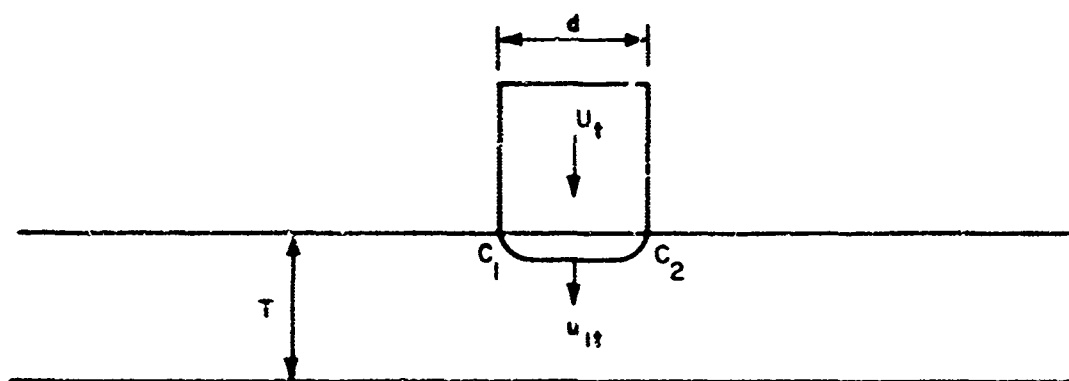


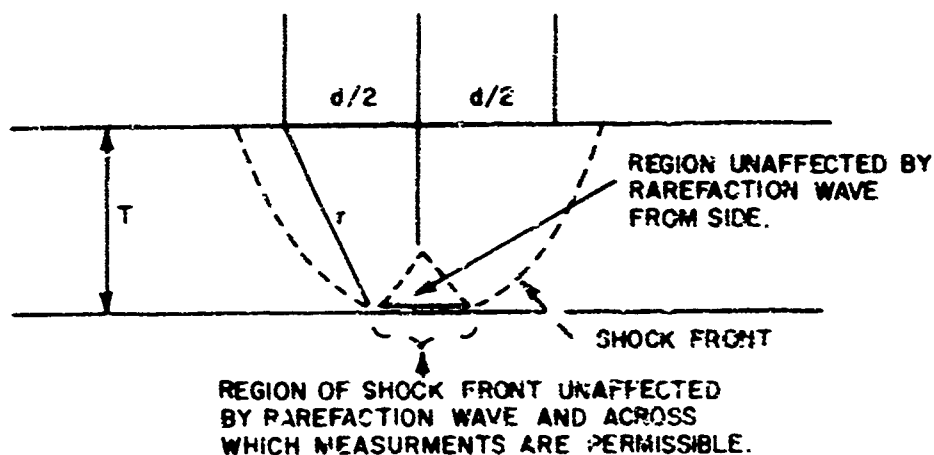
Figure 4. Schematic of Light Gas Gun

c. Target Design

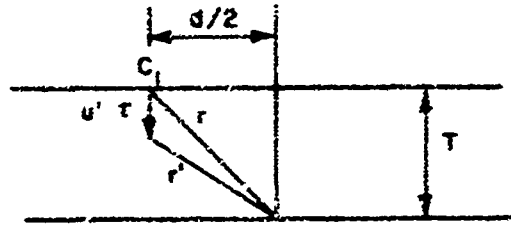
In order to insure that the measurement is made on a one-dimensional shock, i. e., one that is not influenced by rarefactions from the sides of the target or rear face of the flyer plate, it is necessary to determine the maximum permissible thickness of the target sample. The maximum sample thickness which can be used can be approximately evaluated as follows: Consider the following sketch



At impact a shock is generated and propagates with a velocity u_{lt} . From C_1 and C_2 , a rarefaction wave propagates spherically; at a later time, the shock cross section will be as follows:



When the rarefaction has propagated a distance r of $\sqrt{(d/2)^2 + r'^2}$, the entire shock front will have been affected by the rarefaction. In using the rarefaction wave velocity to determine the time required for the rarefaction to reach the center of the sample, correction must be made for the particle velocity. The material originally at C_1 and C_2 will move a distance $u' \tau$ where τ is the time required for the rarefaction to reach the center of the shock front and u' is the particle velocity behind the shock. Thus, with the condition that the rarefaction reaches the center of the shock front just when the shock reaches the rear of the sample, the following relations apply:



$$r' < \sqrt{(T - u' \tau)^2 + (d/2)^2} \quad (34a)$$

$$r' = C_{or} \tau \quad (34b)$$

$$\tau < \frac{T}{u_{lt}} \quad (34c)$$

Substitution gives:

$$\frac{C_{ot} T}{u_{lt}} = \sqrt{\left(T - u' \frac{T}{u_{lt}}\right)^2 - \left(\frac{d}{2}\right)^2} \quad (35)$$

Solution of T gives:

$$T = \frac{d}{2} \sqrt{\frac{1}{\frac{C_{ot}^2}{u_{lt}^2} - \left(1 - \frac{u'}{u_{lt}}\right)^2}} = \frac{d}{2} \sqrt{\frac{1}{\left(\frac{u' - C_{ot}}{u_{lt}}\right)^2 - 1 - \frac{2u'[u' - C_{ot} - u_{lt}]}{u_{lt}^2}}}$$

Using the relations of section III. 2, values of u' and u_{lt} can be calculated for a given impact velocity. The sound speed behind the shock front C_{ot} can be predicted from the equation of state using the relation:

$$C_{ot} = \sqrt{\left(\frac{\partial P}{\partial \rho}\right)_S} \quad (37)$$

where the subscript S represents partial differentiation at constant entropy.

Assuming a constant Grueneisen parameter, the following expression can be derived for the sound velocity in the shock compressed material.

$$C_{ot}^2 = \frac{C_t}{\rho_{ot}(1 - \mu_t)} \left[g(\mu_t) - \mu_t(1 - \mu_t) g'(\mu_t) - (\Gamma_0 + 1) \frac{P_t}{C_t} \right] \quad (38a)$$

where

$$g(\mu_t) = 1 + \frac{D}{C} \mu_t + \frac{S}{C} \mu_t^2 \quad (38b)$$

$$g'(\mu_t) = \frac{\partial g(\mu_t)}{\partial \mu_t} \quad (38c)$$

Calculations of the ratio T/D were made using aluminum 2024 as the projectile material with the values for the constants presented in table I. The data which will be presented later, show good agreement of the 1100 aluminum data with the 2024, which substantiates the use of 2024 in the calculations. To account for uncertainties in the calculated sound speed in the compressed region due to effects such as elastic wave propagation in the compressed material the velocities calculated using equation (38) were increased by a factor of 25 percent to insure a reasonable safety margin in the design thickness. The results of the calculations plotted as a function of impact velocity are shown in figures 5 through 10.

Table I
EQUATION OF STATE CONSTANTS

1. Aluminum Projectile Hugoniot Curvefit³

$$P_f = A\mu_f + B\mu_f^2 + F\mu_f^3$$

$$\rho_o = 2.785 \text{ gm/cm}^3, \quad A = 765 \text{ kb}, \quad B = 1659 \text{ kb}, \quad F = 428 \text{ kb}$$

2. Targets¹⁴

Material	$\rho_{ot} \left(\text{gm/cc} \right)$	C_t	D_t	S_t	Grueneisen Constant
Aluminum	2.785	765	829	-1500	2.17
Teflon	2.16	80.4	104.9	37.0	0.75

d. Projectile Design

Three requirements must be fulfilled in the design of a projectile to be used in shock wave measurements using guns as the accelerator. The first condition is that the thickness of the driver material be at least equal to or greater than the minimum thickness required to insure that no rare-

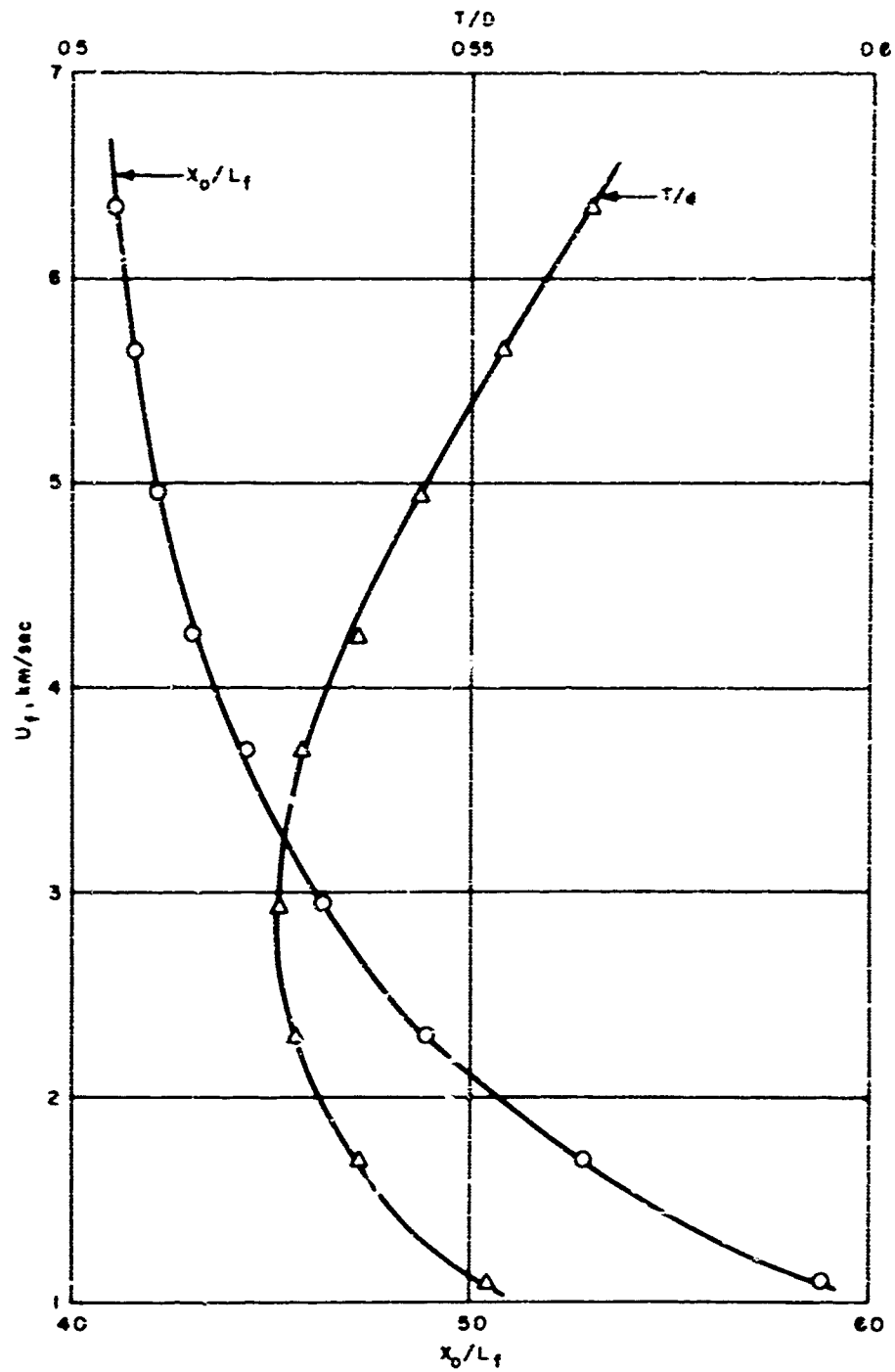


Figure 5. Ratios of x_0/L_f and τ/d as a Function of Impact Velocity
Aluminum - Aluminum ($\mu = 1.0$)

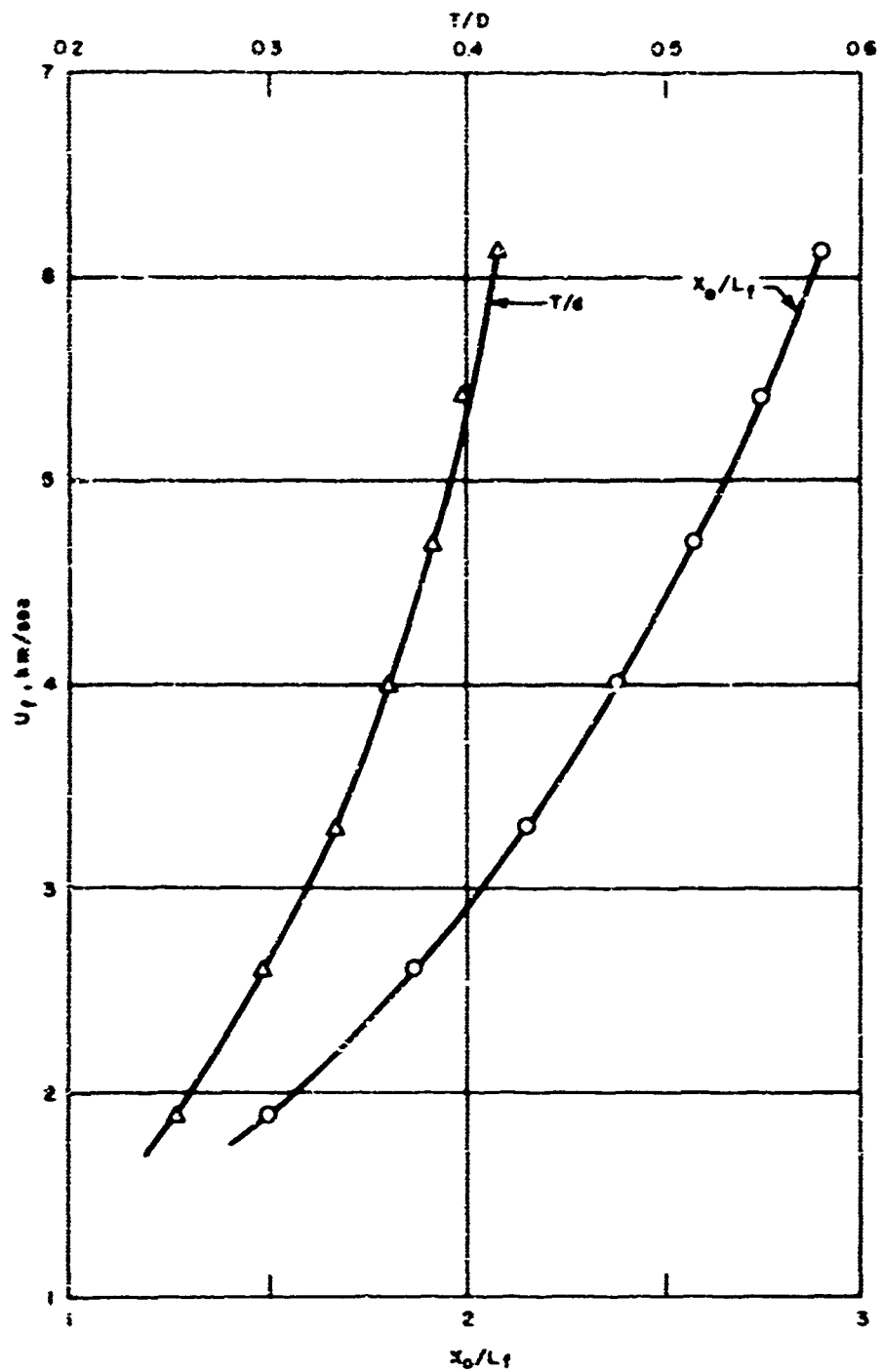


Figure 6. Ratios of x_0/L_1 and τ/δ as a Function of Impact Velocity
Aluminum - Porous Aluminum ($\nu = 1.50$)

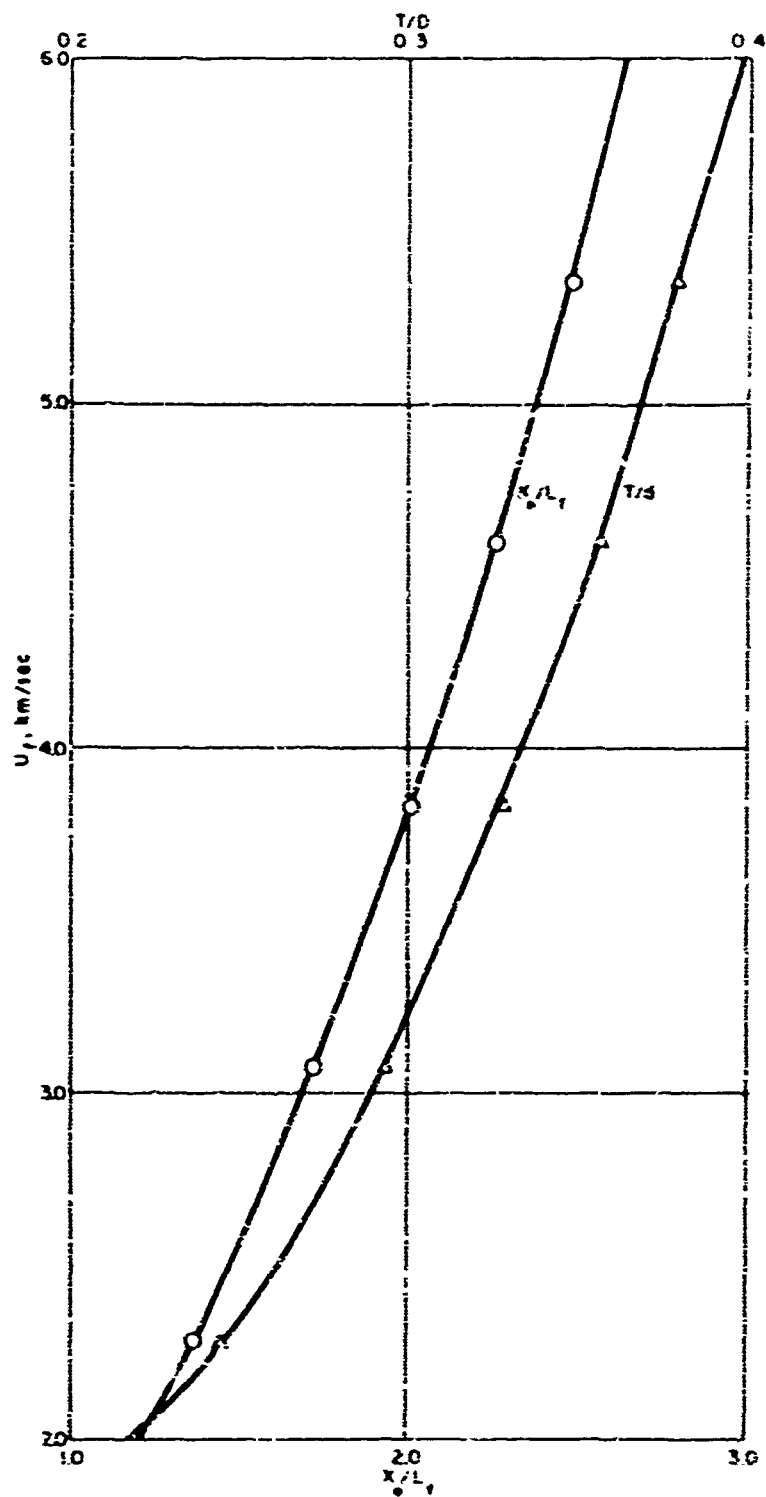


Figure 7. Ratios of x_p/L_p and τ/s as a Function of Impact Velocity
Aluminum - Porous Aluminum ($\lambda = 2.0$)

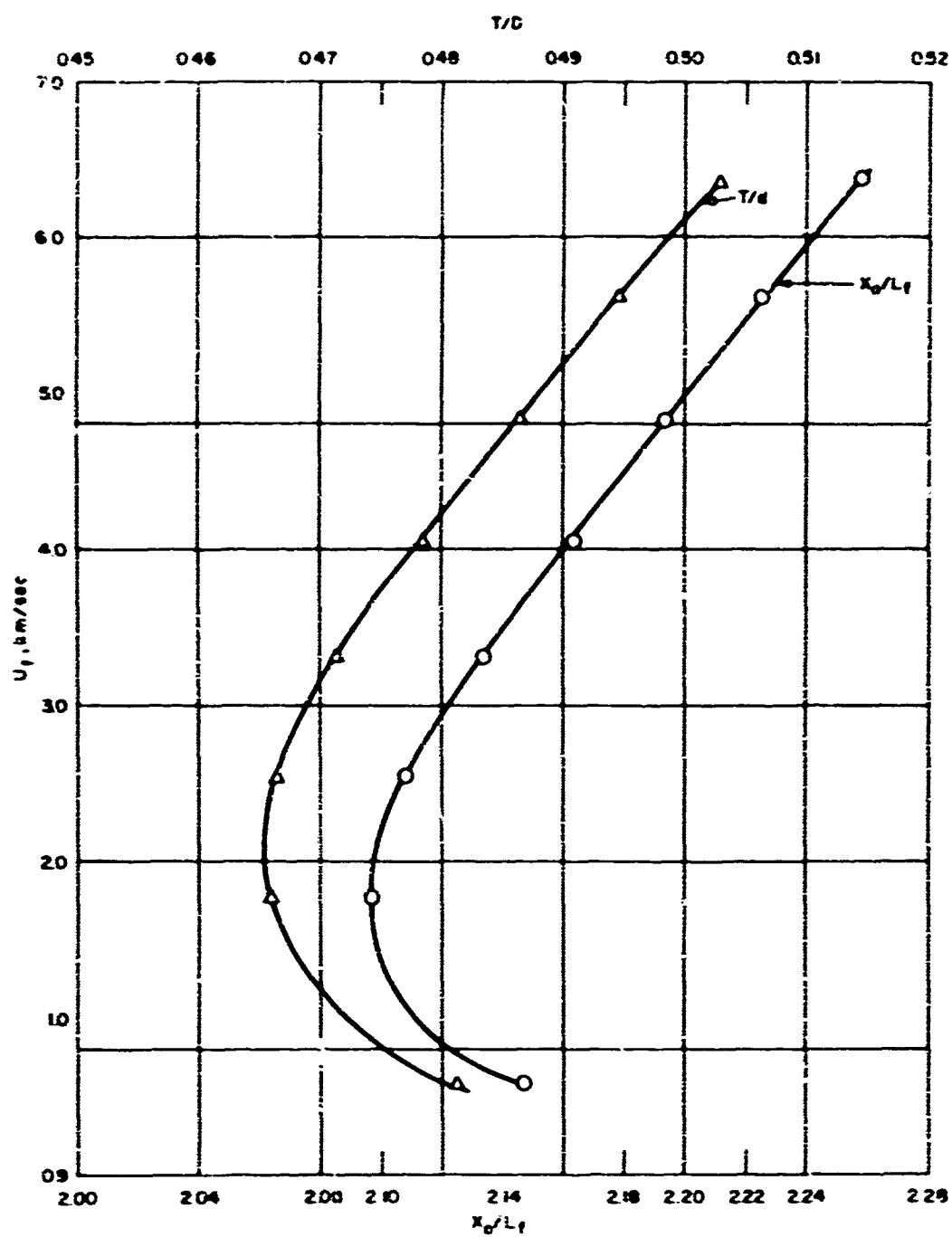


Figure 8. Ratios of x_0/L_1 and T/δ as a Function of Impact Velocity
Aluminum - Teflon ($\mu = 1.0$)

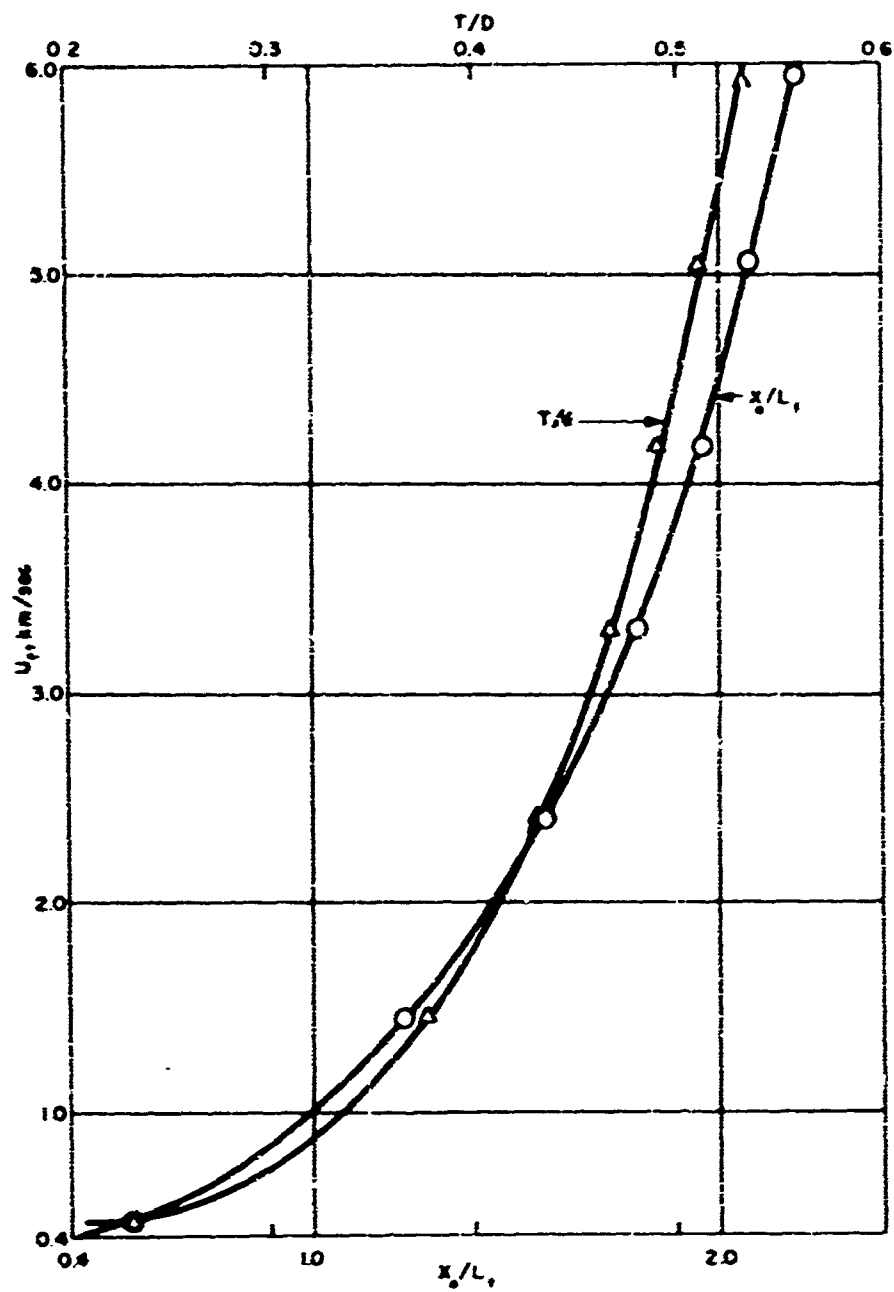


Figure 9. Ratios of x_0/L_1 and τ/μ as a Function of Impact Velocity
 Aluminum - Porous Teflon ($\sigma = 1.50$)

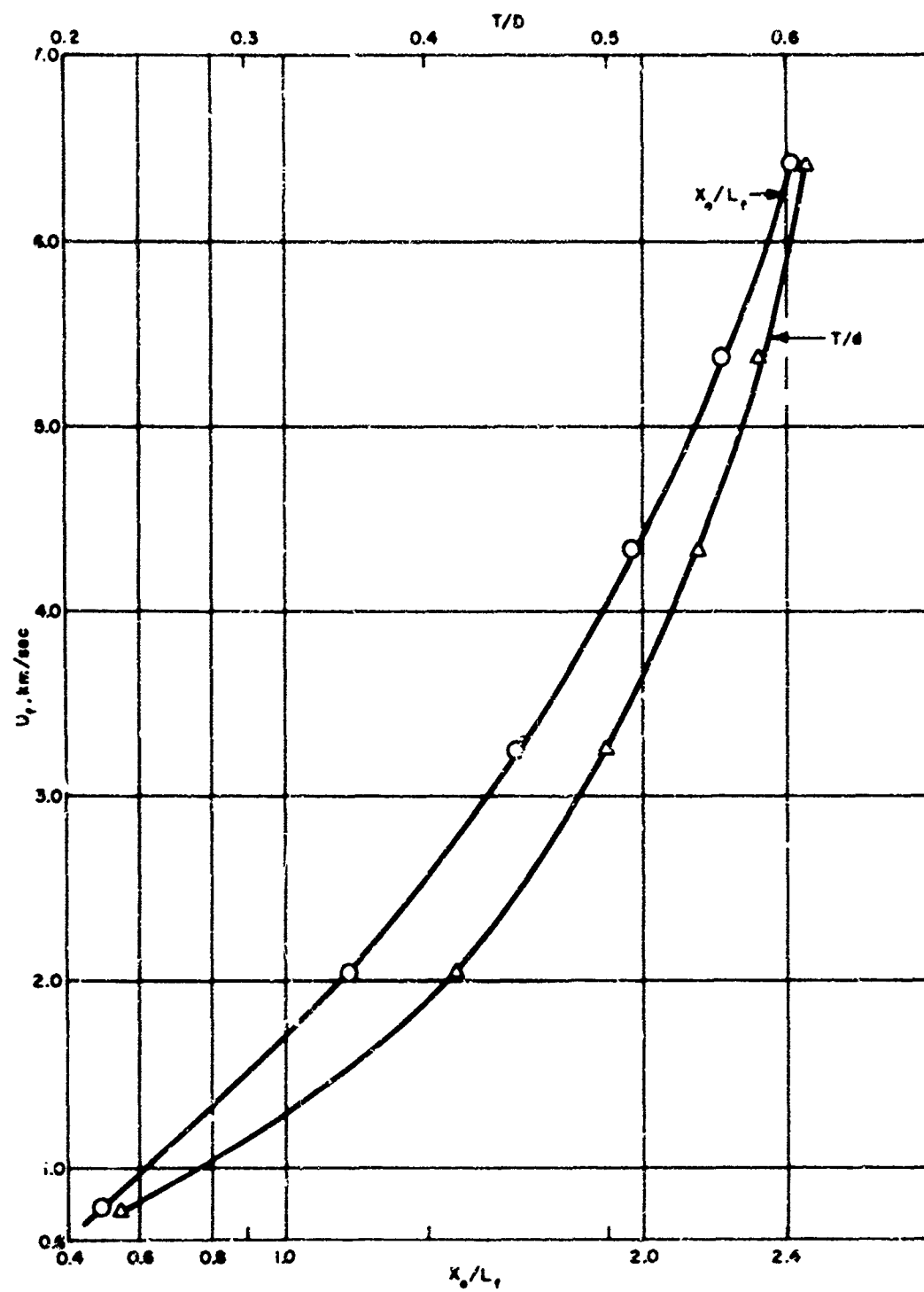


Figure 10. Ratios of x_0/L_r and τ/d as a Function of Impact Velocity
Aluminum - Porous Teflon ($m = 2.50$)

faction wave emanating from the back face of the projectile reaches the shock front in the target before the shock wave measurement is made. The second condition is a consequence of the method being used in this study, that is, to prevent the accelerating gas from leaking around and ahead of the projectile during the launch phase. This is commonly referred to as "blowby gas," and the elimination or reduction of this gas to a reasonable level is essential so as not to disturb the target either prior to or during the time the measurement is made. The third condition is that the projectile be of sufficient length so that the impact between projectile and target take place while part of the projectile is in the launch tube, insuring a planar impact.

The first condition arises because one is interested in launching projectiles to high velocities and therefore, it follows that one must consider ways of minimizing the projectile mass. Thus one is interested in the minimum driver thickness that one can work with. Bade (reference 6) has developed relations for predicting the minimum thickness required to insure no rarefaction. Consider the following model. At time $t = 0$, a projectile with thickness L_f and velocity U_f comes into contact with a semi-infinite target body. The motion is assumed to be one-dimensional. The impact creates a pair of shock waves, one advancing into the target, the other traveling back into the flyer plate. The shock in the flyer plate is reflected from the free surface as a rarefaction wave which traverses the flyer plate, passes through the contact surface into the target and eventually overtakes the shock in the target. Figure 11 shows the $x-t$ diagram for this sequence of events.

The relations for calculating all shock parameters in both the target and projectile are given in Section III.2. The sound velocity in the compressed material behind the shock front can be determined from equation (38) for both the target and projectile using these calculated

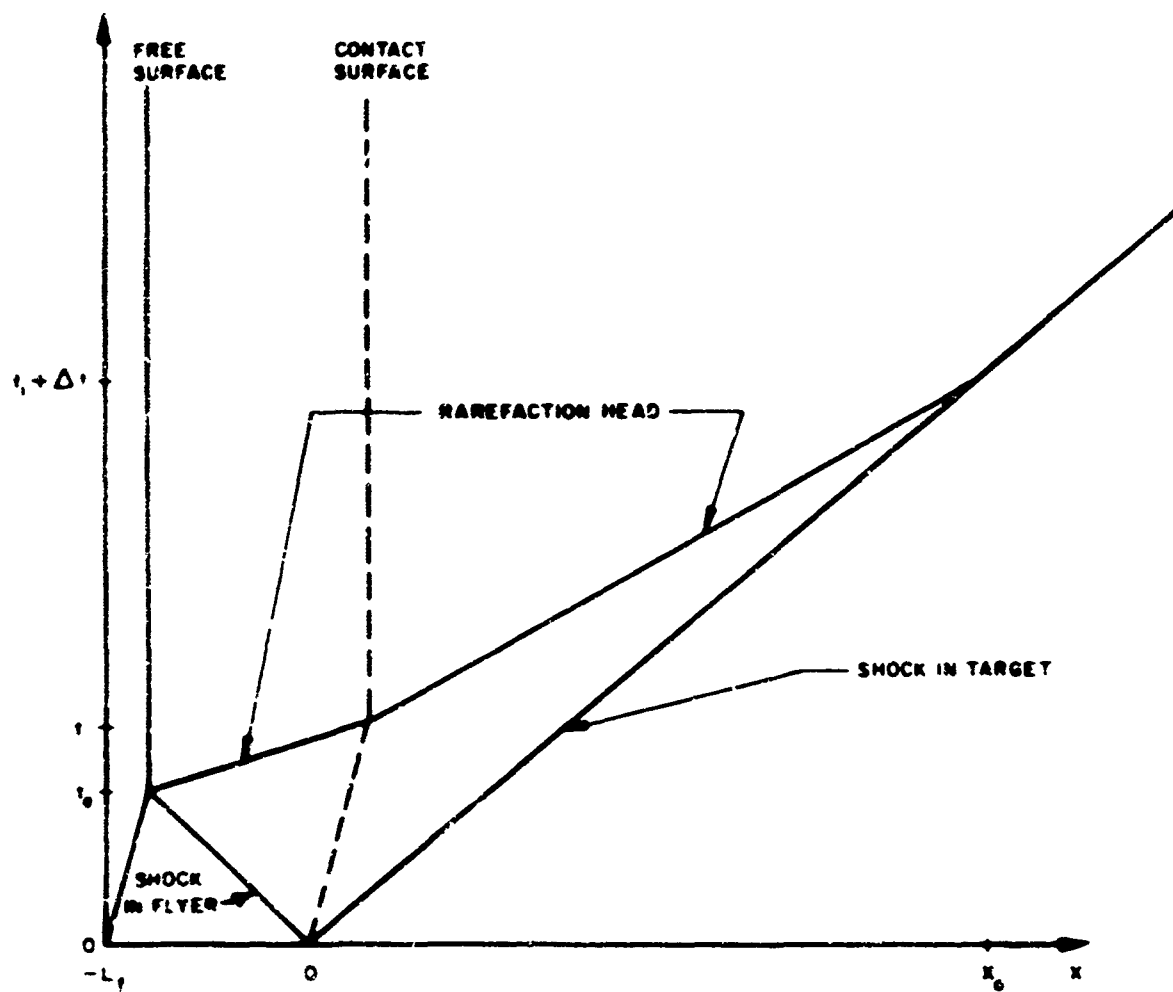


Figure 11. $x - t$ Diagram for Plate Impact Experiment

shock parameters. Following Bade (reference 6) then, the time for the shock in the flyer plate to reach the free surface is:

$$t_0 = \frac{L_f}{u_{1f}} \quad (39)$$

where u_{1f} is the velocity of the shock relative to the undisturbed material. The time for the rarefaction from the 1. surface to reach the contact surface is:

$$t_1 - t_0 = \frac{L_f}{(1 + \mu_f) C_{of}} \quad (40)$$

since the thickness of the flyer plate after shock compression is $L_f (1 + \mu_f)$. Let Δt be the time interval between crossing of the contact surface by the rarefaction and overtaking of the shock in the target by the rarefaction. The thickness of the shocked layer in the target at the time of overtaking is then:

$$\frac{x_0}{m(1 + \mu_t)} = \frac{u_{1t}(t_1 + \Delta t)}{m(1 + \mu_t)} \quad (41)$$

Hence,

$$C_{ot} \Delta t = \frac{u_{1t}(t_1 + \Delta t)}{m(1 + \mu_t)} \quad (42)$$

so that

$$\Delta t = \frac{u_{1t} t_1}{1 + \mu_t} \cdot \frac{1}{m C_{ot} - \frac{u_{1t}}{1 + \mu_t}} \quad (43)$$

The ratio of the Lagrangian depth x_o at which overtaking occurs to the initial flyer plate thickness L_f is then from equations (40), (41), and (43):

$$\frac{x_o}{L_f} = \frac{\frac{1}{u_{1t}} + \frac{1}{(1 + \mu_f) C_{ot}}}{\frac{1}{u_{1t}} - \frac{1}{m(1 + \mu_t) C_{ot}}} \quad (44)$$

Calculations have been made of the ratio x_o/L_f , using equation (38) for C_o , with the calculated sound speeds increased by 25 percent for a safety factor. Plots of the ratio x_o/L_f as a function of flyer projectile velocity U_f are also presented in figure 5 through 10.

Thus given a bore diameter, one can specify the maximum target thickness and minimum projectile thickness as a function of impact velocity from figures 5 to 10 for an aluminum projectile impacting on aluminum and Teflon respectively.

It was planned to experimentally verify the above calculations by firing a projectile of a given thickness into targets of varying thicknesses, at a constant velocity. The pattern of the shock velocity as a function of target thickness would then be an indication of the target thickness at which rarefactions would influence the phenomena. Since rarefactions would have the effect of lowering the pressure at the shock front, and thus decreasing the shock velocity, a plot of shock velocity versus target thickness would show a constant shock velocity with increasing target thickness in the region where no rarefactions were present, and then the shock velocity would decrease with increasing target thickness where rarefactions influenced the process. The same experiment could be carried out to verify the projectile thickness calculations by varying the projectile thickness and keeping the target thickness and impact velocity constant. A plot of the shock velocity as a function of projectile thickness would reveal the minimum allowable projectile thickness.

Unfortunately, time did not permit experimental verification of the effect of target and projectile thicknesses since a large number of shots would be required to determine these effects statistically even for one velocity and porosity. However, as previously mentioned, the velocities calculated by equation (38) were increased by 25 percent in all cases to insure that unforeseen effects such as elastic wave propagation in the shock compressed material would not affect the measurement. The ratio of elastic to plastic wave velocity should be less than 1.25. Furthermore, in most cases, the target thickness was considerably less and projectile thickness considerably greater than the thickness limits based on the preceding calculations. The actual projectile designs used in the studies will be discussed in Section IV. 4.

2. Technique of Measurement

To determine the characteristics required to specify the solid equation of state, namely the pressure, compressibility and the specific internal energy of a material after shock compression, 2 of the 10 parameters discussed in Section III. 2 must be measured. This assumes that the driver Hugoniot equation of state is known. If the driver Hugoniot is unknown it can be determined by using the unknown material as both the projectile and the target material, for this study, the flyer plate or projectile velocity U_f and the shock velocity in the target u_{It} were the two parameters measured and the Hugoniot of the 1100 aluminum used as the flyer plate was experimentally determined.

In shock wave measurements, it is customary to strive for accuracies of ± 1 percent or better. Because the projectile velocity would have to be measured over short distances (on the order of 0.125 to 0.250 inch) and times (about 1μ sec), a low inertia, high frequency and high resolution system was required. An optical technique employing a laser as a source mainly for its monochromaticity and power density, and a photomultiplier tube as optical sensor was developed to make the measurements.

The advantages of using ballistic guns together with optical techniques employing a monochromatic source and photomultipliers have several distinct advantages over other techniques in shock wave measurements. Namely,

- a. Planarity of impact can be easily controlled by a combination of careful machining of projectile and launch tube and proper alignment of target and projectile. By causing the impact to occur while the projectile is still partially in the launch tube, the projectile is constrained to impact planar.
- b. The use of a monochromatic light source such as a laser allows the use of narrow band interference filters, which allows the shock time of arrival to be measured without interference from the impact flash.
- c. Photomultipliers have extremely fast rise times, on the order of 5 nanoseconds, and can draw large currents operating in a dark-to-light mode.

A simplified schematic of the system is shown in figure 12. The laser beam is passed through a beam splitter which separates the beam into two beams, one of which is directed on the projectile face, the other on the target rear face. These beams are focused by a long focal length lens, so that small movements of the surfaces will not result in appreciable defocusing of the spots. Since the laser beams are well collimated, the size of the spots of light on the surface is small (approximately 0.005-inch diameter). Upon reflection from the surfaces, the spots are refocused by means of a wide aperture lens on to slit planes. As the projectile travels toward the target, it intersects the front beam and reflects it through the first slit. As the projectile moves it sweeps the front beam until the beam reaches the second slit. After the projectile impacts the target, a shock is generated in the target, and displaces the rear surface of the target, causing the rear surface laser beam to pass through the third slit. Behind each slit is a photomultiplier which detects the light and converts it to an electrical signal.

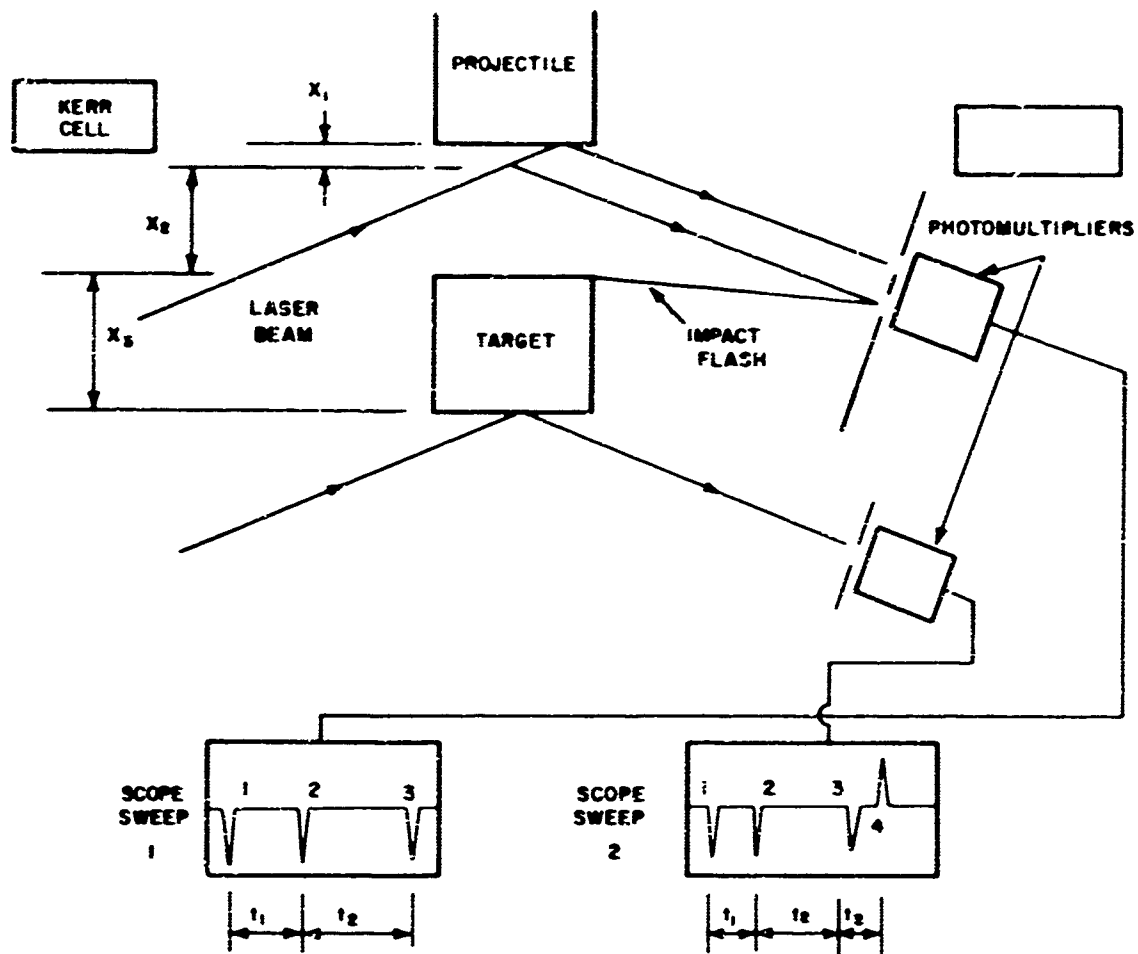


Figure 12 Simplified Schematic of System which Measures Impact and Shock Velocity,

Two notable features of this system are: first, the projectile may tilt within planarity tolerances, which was set at ± 5 milliradians, and not introduce error in the time when the refocused spot passes the slits even if the surface has a mirror finish. This is true because the spot of light on the surface acts as a point light source such as a hot spot on the surface. The effect is similar to that in a rotating mirror framing camera which employs the Miller (reference 16) optics. The surface finish, therefore, is only a factor in the quantity of light reaching the photomultiplier. To minimize the loss of light due to diffuse reflection, the lens on the photomultiplier side of the system is a wide aperture lens. A second feature is the fact that the photomultipliers operate in a dark-to-light mode rather than in the light-to-dark mode which exists in a beam interruption system. The advantage stems from the fact that much more current can be drawn from a photomultiplier exposed to a pulse of light than to a continuous light. Therefore, one can use lower impedances when working with a light pulse than with a dark pulse to obtain the same signal voltage. Lower impedances mean faster rise times, therefore, higher frequency response.

Three distance measurements are required to be known: first, the distance the projectile travels when the reflected beam passes through slits 1 and 2; second, the distance between the second projectile position and the face of the target; and third, the thickness of the target.

The procedure followed in this experiment is the following. Before the shot, the target is first positioned parallel to the face of a simulated projectile. The simulated projectile is then set back a known distance from the target face by a set off accurately machined spacers. This defines the distance between the second projectile position and the impact plane. The laser beam is then reflected off the simulated projectile face and the slit plane adjusted so that the reflected beam passes through slit 2 (see figure 20). Then the micrometer-driven simulated projectile is positioned until the reflected beam passes through slit 1. A plot of the relative slit current

as a function of projectile position is shown in figure 19. It can be seen that the current rise from 10 to 90 percent of full scale occurs over a 0.003-inch displacement of the projectile. By calibrating the slits on the mid-point of the rise portion of the curve, distance can be measured easily to within a 0.001 inch.

The final distance is obtained by accurately measuring the thickness of the target with a micrometer.

To accurately measure the velocities required, one must specify along with the position measurements discussed above, the time of arrival of the projectile at the known points in space along with the impact time and shock time of arrival at the rear surface of the target. This is done in the following manner. When the projectile arrives at the position in space where it reflects the laser beam through slit 1, the photomultiplier responds by converting the light pulse to an electrical signal which triggers both sweeps of a dual beam scope. The output of PM1 also is applied to the vertical deflection plates of both traces, giving a pulse at the first known projectile position. As the projectile moves toward the target, it reflects the laser beam, giving a second pulse on the scope trace. The impact time is measured by reflecting the flash of light generated on impact on to PM1 through slit 3 (see figure 20), giving a third pulse on the scope.

The impact flash has been and is still being studied by others (references 10 and 11) in the field of hypervelocity impact. These studies were made to determine the effects of various projectile and target parameters on the mechanism and nature of the impact flash. Gehring (reference 11) has showed that the flash occurs instantaneously on impact, and has a rise time which varies depending on the materials under impact, but in all cases reported, was less than a few tenths of a microsecond. Conversation with personnel of the Geophysics Corporation of America reveals that the nature of the impact flash is a fast rising (on the order of a tenth of a microsecond) pulse of continuum (i. e. gray-body) radiation followed by the characteristic

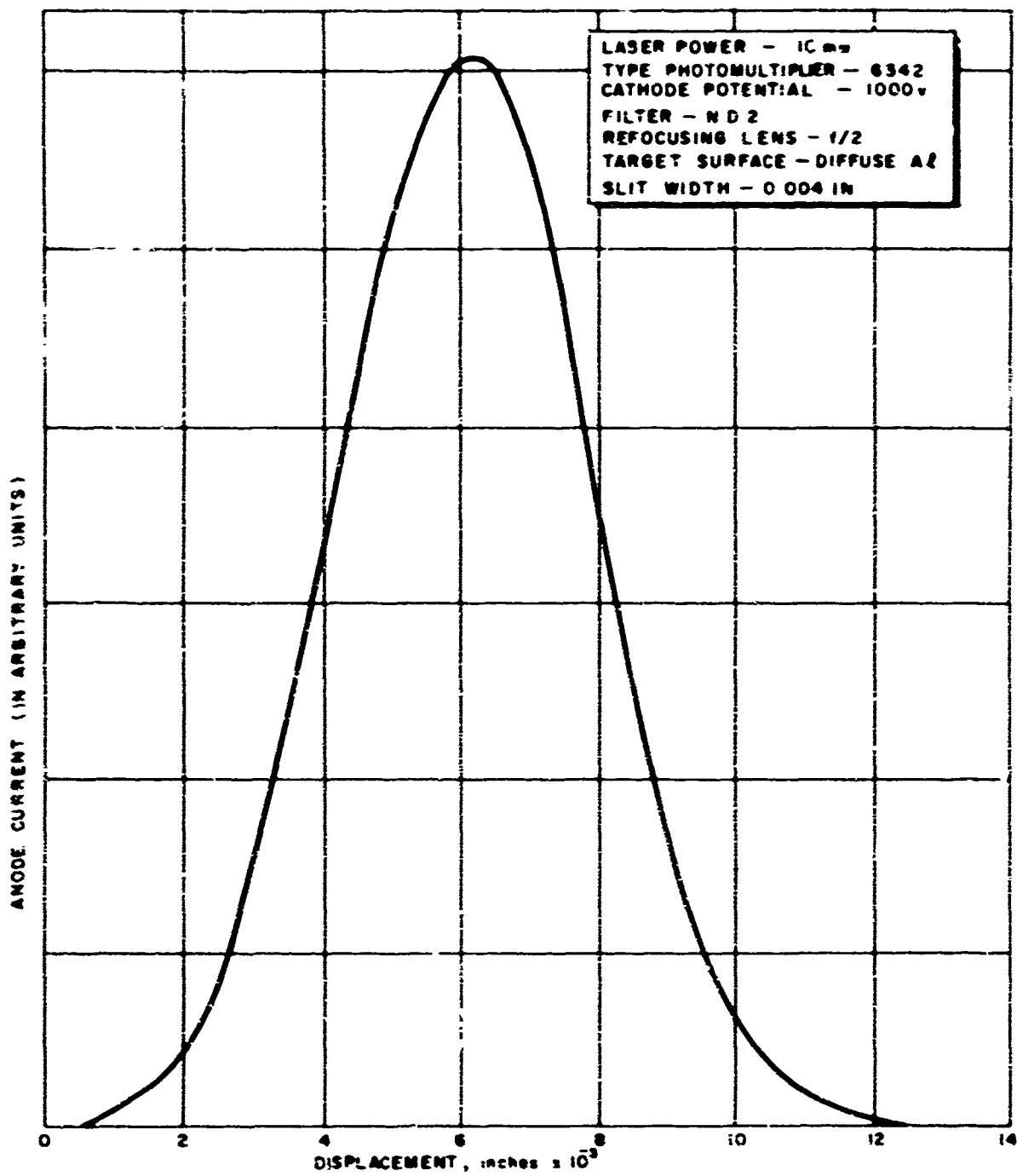


Figure 13. Plot of Relative Photomultiplier Anode Current as a Function of Projectile Displacement

band and/or line spectra of the materials under shock compression. Our observations indicate that PM1 does detect the initial continuum radiation, evidenced by the rise time (about 50 nanoseconds) and the fact that the flash is detectable with and without an interference filter. Another indication that this flash does indeed represent the instant of impact can be observed from the data, which showed that the measured and predicted times of impact generally agreed to within 1 percent.

The shock time of arrival is measured in the following way. Initially, during slit calibration, the laser beam reflected off the back face of the target is allowed to impinge directly adjacent to a slit in front of PM2 (see figure 20). When the shock reaches the rear surface of the target, this spot is swept onto PM2, giving the shock time. The output of PM1 and PM2 are passed through a differential amplifier where they are mixed and the difference applied to the bottom sweep of the scope. The polarity of a signal identifies from which photomultiplier the signal originated.

Time resolution is obtained by superimposing on the top and bottom sweeps, a 5 or 10 mc crystal controlled timing wave, and with the use of an optical comparator, time measurements can be made to an accuracy of about 5 to 10 nanoseconds.

An example of the oscilloscope record obtained is shown in figure 14. This shot was for aluminum on solid Teflon (shot 107) at a velocity of 1.88 km/sec. The distance the projectile traveled between the first two pulses is 0.118 inch and the distance the projectile travels from the second pulse to impact is 0.325 inch. The target thickness was 0.252 inch. The nature of the impact flash, that is its fast rise, which in this shot occurs in less than 50 nanoseconds, is characteristic of all impacts observed, including those on the porous materials.

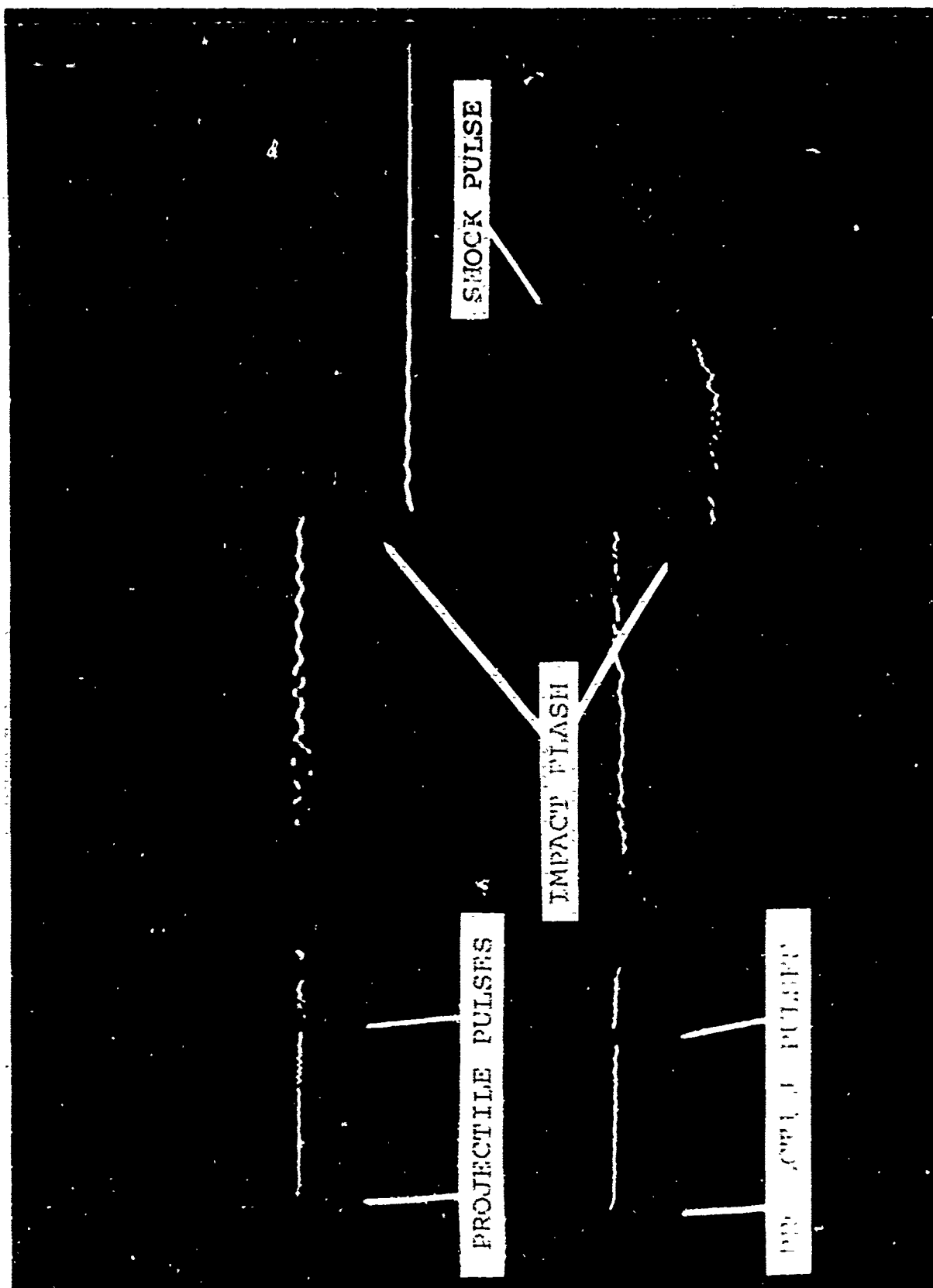


Figure 14. Oscilloscope Record of Shot 107 - Aluminum on Solid Teflon ($m = 1$)
Reference Time Marker Frequency is 5 mc - Sweep Speed 1 μ sec/cm

The last observation that must be made is that of the planarity of impact. A pair of orthogonal Kerr Cell Shadowgraph stations were used to observe the projectile in flight prior to impact to insure that the impact is planar. This system will be described in detail in section IV. 3. Typical records which are obtained are shown in figure 15. These pictures also allowed a determination of whether blowby gas was present in the field.

3. Description of Equipment

The basic requirements for the apparatus are:

- a. The impact between the target and projectile must be planar.
- b. The space between the projectile and target must be evacuated to eliminate air cushion effects between the projectile and target.

The enclosure which contains the vacuum must be rigid so that the windows which transmit the light beams will not move and deflect the beams when the enclosure is evacuated. Also, gas leakage past the projectile during acceleration down the barrel must be eliminated.

- c. The optical system must be mounted rigidly so that there is no appreciable motion either between the components themselves or between the optical system and the target.
- d. There should be mechanical isolation between the gun components and the instrumentation and test section to avoid any acoustical transmission between the two.

The following discussion describes the equipment used for this experiment which satisfies the above requirements.

a. Test Section

The test section refers to the enclosure which houses the sample under shock compression. To insure that the impact between target and projectile is planar, the target must be positioned near the end

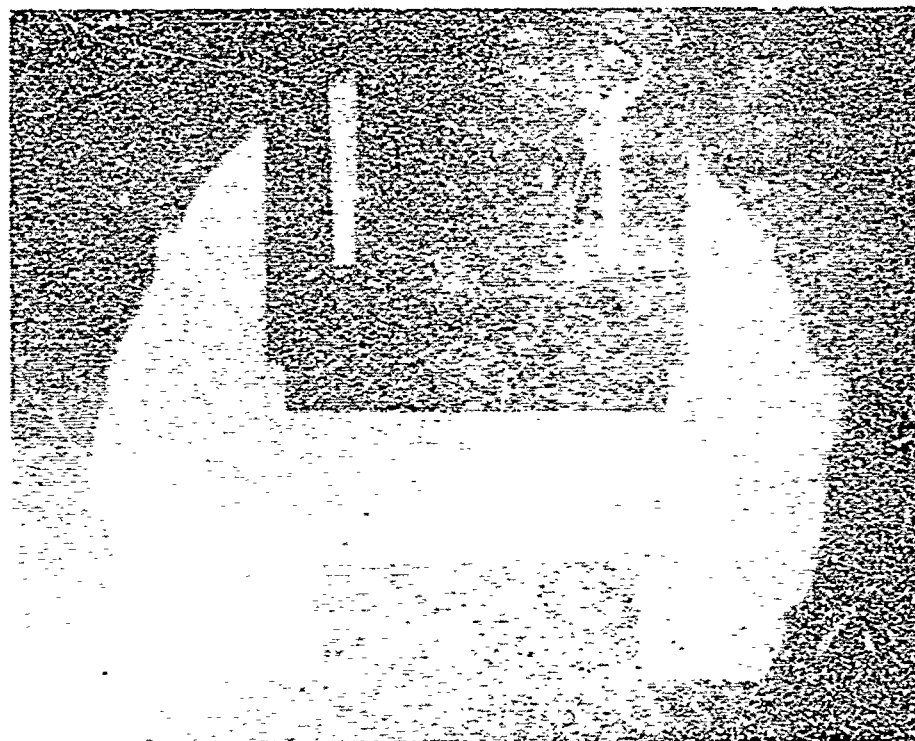
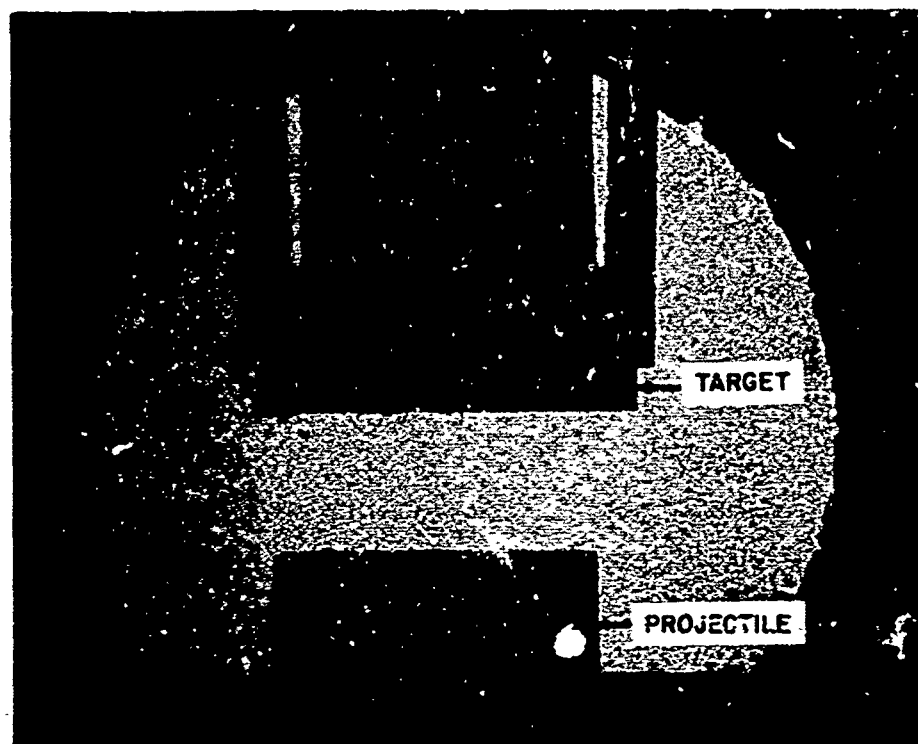


Figure 15. Orthogonal Shadowgraph Records of Shot 107 About 3.5 μ sec Prior to Impact - Magnification (2:1)

of the launch tube so that impact takes place while the projectile is still partially in the launch tube. The launch tube acts as a constraint against any motion other than one-dimensional and forces the impact to be planar. Thus the position of the test section in relation to the gun is required to be at the end of the launch tube. The test section was designed to be adaptable to present range sections, is extremely rigid in construction to maintain precise alignment between the projectile and the target sample during evacuation, and contains the necessary ports to view the projectile with the orthogonal Kerr Cell Shadowgraph System and to make the necessary velocity measurements with the laser-optical system.

Figure 16 is a cross-sectional print (normal to the optical plane of the shadowgraph stations) of the target tank, showing the sample, sample holder, and projectile prior to impact. The tank is cylindrical in shape and constructed of 7/8-inch-thick stainless steel. It contains six stainless steel ports, four of which are spaced at 90-degree intervals in the optical planes to the shadowgraph cameras, and the other two at an angle of ± 60 degrees to the longitudinal axis of the cylinder to enable the laser beam to enter and be reflected to the photomultipliers. Figure 17 shows a print of the tank (view in the plane defined by the incident and reflected laser beam) showing the sample, projectile and laser ports, along with the incident and reflected laser beams.

To properly align the sample face to the incoming projectile insuring planarity, a stainless steel gage block was designed and fabricated. The block is fitted to a flange which attaches to the face of the target tank. The block has a carefully machined face which is of a length comparable to the distance the projectile travels from the end of the barrel to impact. The sample is held in a slotted brass cylinder having an inside diameter such that a friction fit exists between the sample and sample holder. The slot is necessary to allow the laser beam to reflect from the back face of the sample. Figure 18 is a photograph of

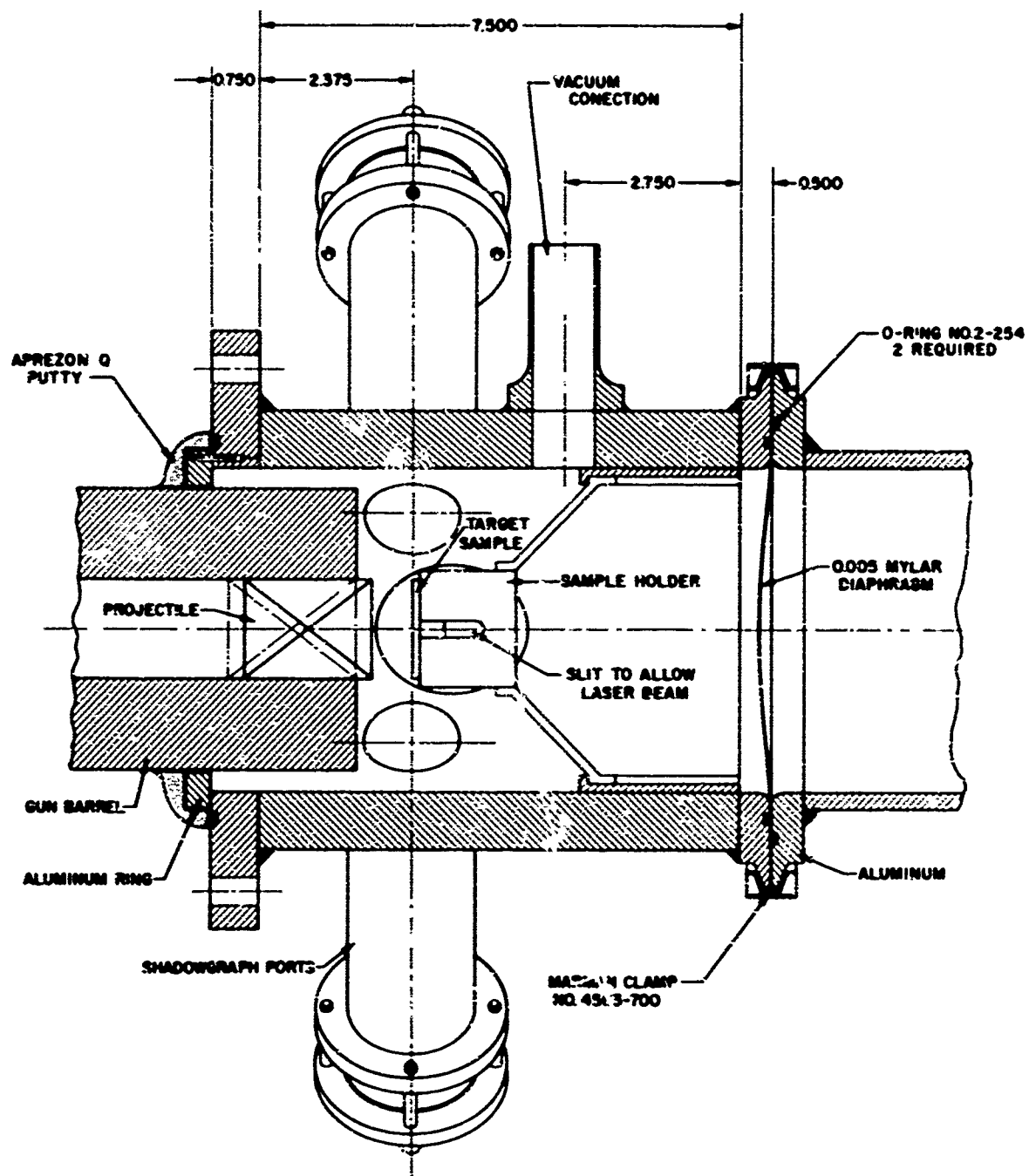


Figure 16. Grueneisen Parameter Tank Assembly - Vertical Plane

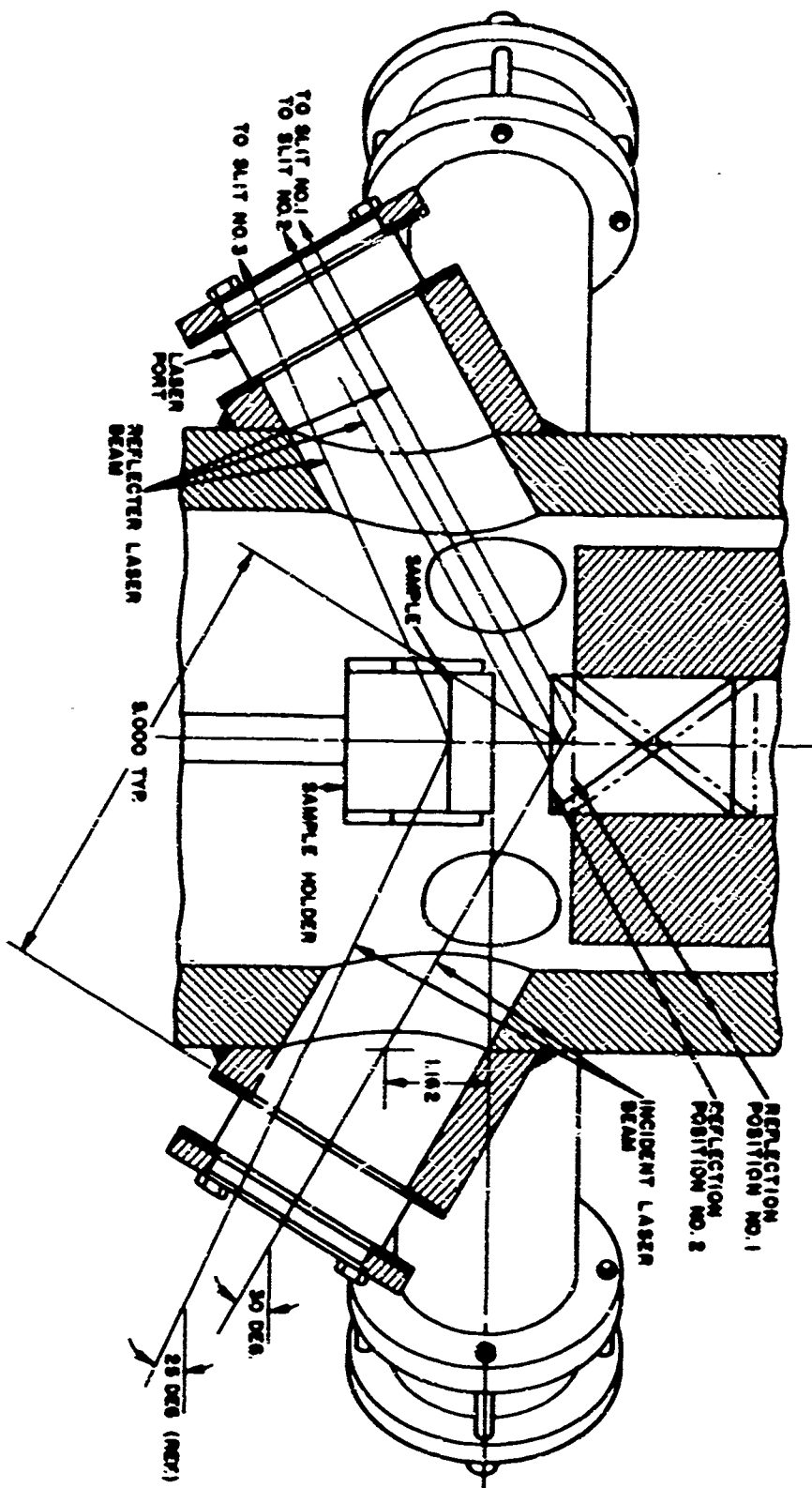


Figure 17. Grueneisen Parameter Tank Assembly - Horizontal Plane

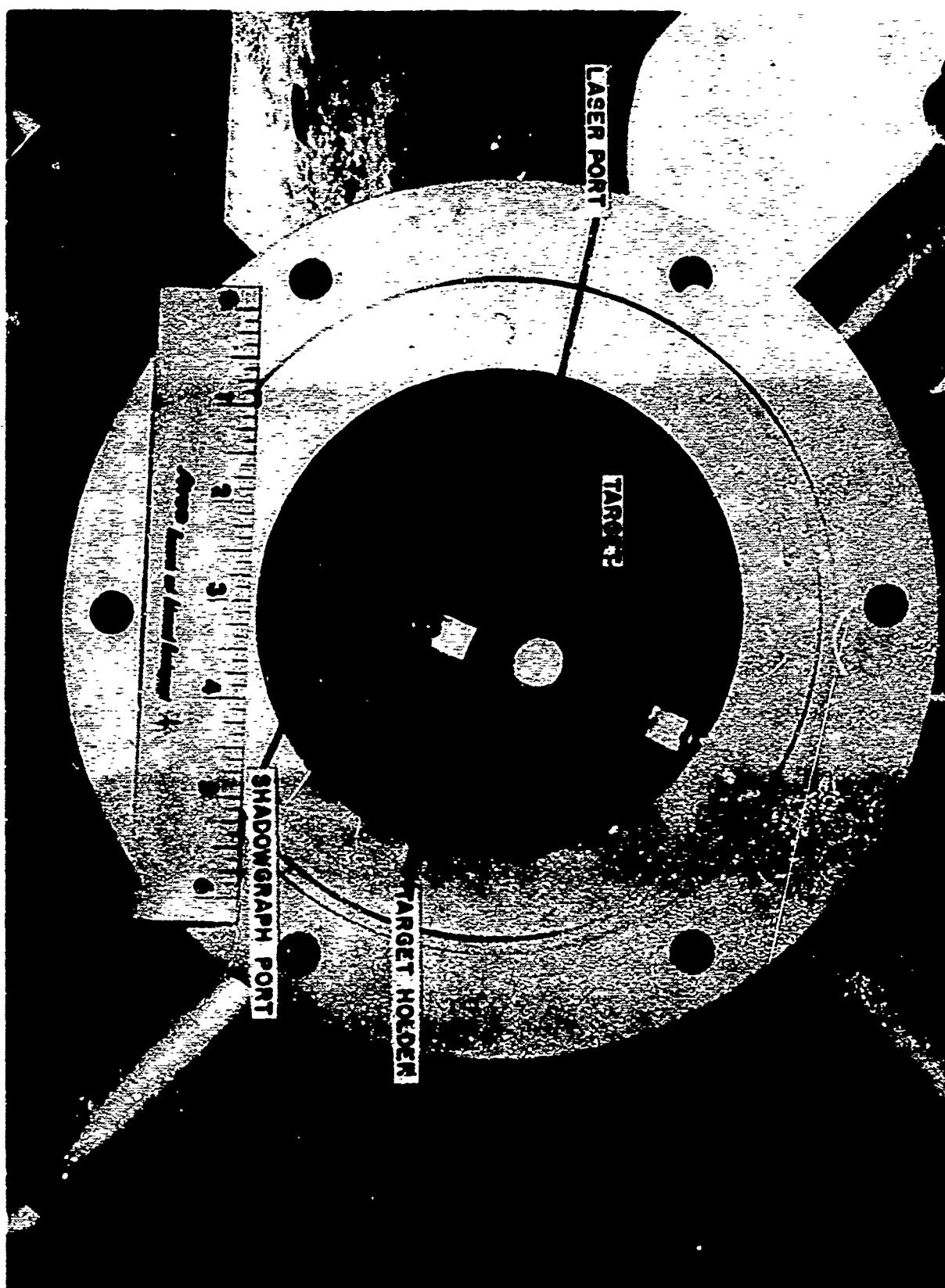


Figure 18. Photograph of Inside of Test Section Showing Target in Position in Target Holder

the inside of the test section showing the target in position inside the holder. Proper alignment of the sample to the gage block face is performed by manual adjustment of the sample until complete contact is made between the two faces. This is checked visually through the shadowgraph ports. A spacer of known thickness is then set between the gage block flange and the tank, setting the gage block back a known distance from the target surface to the point where it is desired that the reflected laser beam from the projectile passes through the second slit to PM1. The laser beam then is reflected off the gage block, and the slit plane is adjusted so that the reflected beam passes through slit 2 (see figure 20). The gage block flange is replaced by a micrometer-driven simulated projectile which then measures the distance the projectile will travel when the reflected beam laser from the projectile passes from slit 1 to slit 2.

The final part of the system which must be aligned is the launch tube or gun barrel. This is done by carefully machining the outside diameter of the barrel so that it is perfectly concentric to the axis of the gun. An alignment collar is then slipped over the outside diameter of the gun. This collar contains a flange which contacts the flange of the test section. The gun and/or the test section is then adjusted until both flanges are perfectly flush with each other over the entire areas of each. This insures that the projectile will impact parallel to the target surface, since both the end of the gun and the target are parallel to a common reference, the front flange of the test section.

The test section and the instrumentation system are all rigidly mounted to an I-beam to prevent any relative motion between the components of the instrumentation system or between the test section and the instrumentation system. This assembly is shown in figure 19. This I-beam is shock mounted on concrete piers in front of the gun muzzle and the test section is slipped partially over the muzzle with a

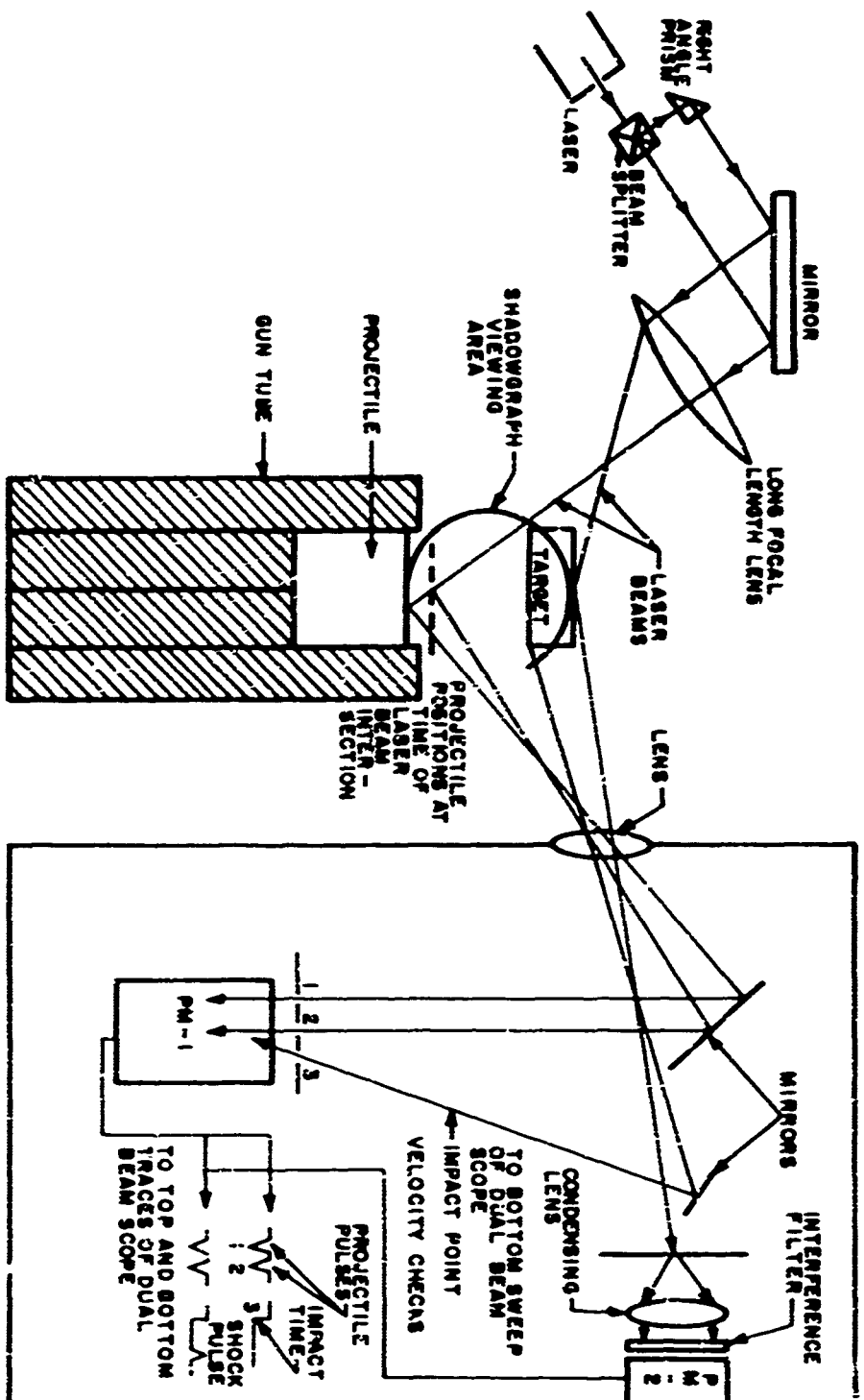


Figure 20. Schematic of Optical Instrumentation Used on Grinnelsen Parameter Study

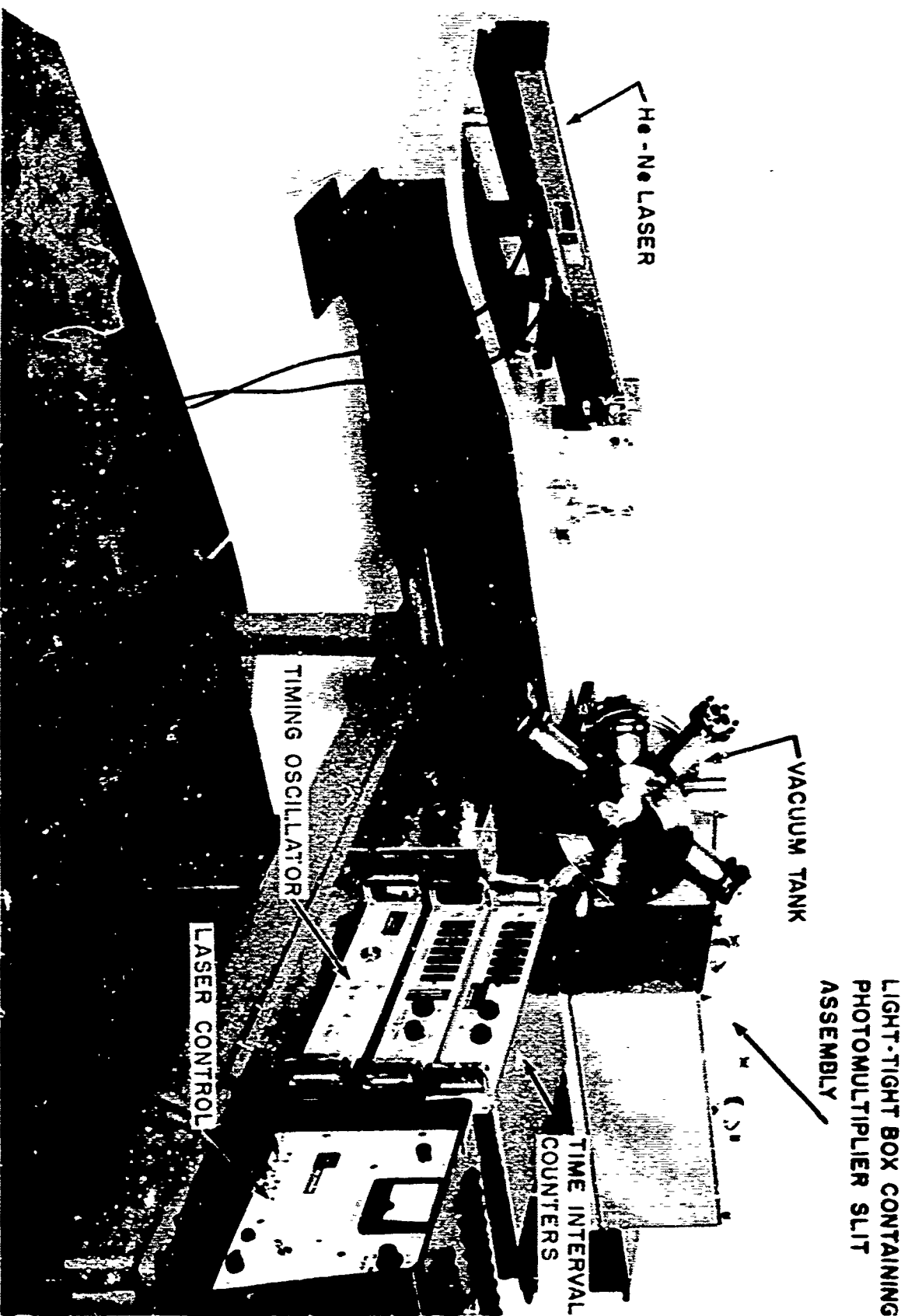


Figure 19. Photograph Showing Overall View of Vacuum Tank and Laser Optics Assembly on I-Beam

1/16 inch space between the two. This space is filled with Apiezon "Q" vacuum putty providing both a vacuum seal and acoustical isolation between the gun and the cylinder.

In order to insure that the sample is not affected by any air cushion effects due to trapped air in front of the projectile prior to impact, the test section was evacuated to a pressure of 10 to 20 microns of Hg prior to each shot. A Welch Duo Seal two-stage mechanical pump was used to evacuate the gun barrel and test section to this pressure, with a 5 mil diaphragm separating the target tank from the back of the range. A CVC Bourdon gage was used to monitor the pressure from atmosphere down to 2 mm of Hg and a thermocouple vacuum gage monitored the pressure down to the final level.

O-rings were used between the tank and transition section to the rear of the range, and neoprene flat gaskets were used to seal the ports at the windows.

b. Instrumentation

(1) Optical

A schematic of the optical instrumentation is presented in figure 20. The beam from a He-Ne gas laser is divided by a beam splitter into two beams, one of which is focused on the face of the projectile at a known point in space, and the other is focused on the center of the target back face. A long focal length lens is used to focus the beam, to minimize defocusing at both projectile positions where the velocity measurement is made. After reflection, the light reflected from the projectile and target is refocused by means of a wide aperture lens onto the slit planes in front of photomultipliers one and two (PM1 and PM2). The impact flash is reflected by a pickoff mirror onto the slit plane (through slit 3) onto PM1. In order not to saturate PM2 by the impact flash, a narrow band interference filter was used with a collimating lens in front of PM2.

The photomultipliers used were RCA 4459 having 12 dynodes and an S-20 response. The windows used on all ports were 5/8 inch thick lucite.

(2) Electronics

A block diagram of the electronics system associated with the optics is shown in figure 21. The output of photomultiplier 1 is used to trigger the electronics. This is fed to the external trigger of a 555 Tektronix Dual Beam Oscilloscope, Channel B of a dual channel amplifier, and Channel A of a differential amplifier. The dual beam scope was used because earlier in the program, three slit pulses were used to measure the projectile velocity, and the third pulse was fed to a different PM than the first two.

A trigger pulse from a built-in delay generator on the 555 Scope is then fed at a preset delay after the initial trigger to a pulse amplifier. The output of this latter unit is then fed to both shadowgraph units and a pedestal pulser. The pedestal pulser was used as a transient power supply for PM2. Initially this photomultiplier was to be operated with a high resistance (1.3 megohm) voltage divider and with capacitors across the last few dynodes to allow large dynode currents during the light pulse. This network was used on PM1 and is shown in figure 22. However, when the spot of light from the rear surface of the target was focused at the slit plane, a small halo caused by surface irregularities in the optics was observed around the focused spot. When the spot was placed just adjacent to the slit, the halo illuminated the slit and caused a certain amount of anode current. Although this current produced an insignificant voltage signal across the anode resistor, it was sufficient to drop the voltage across the last few dynodes, thereby discharging the capacitors and rendering the photomultiplier incapable of drawing large currents desired when

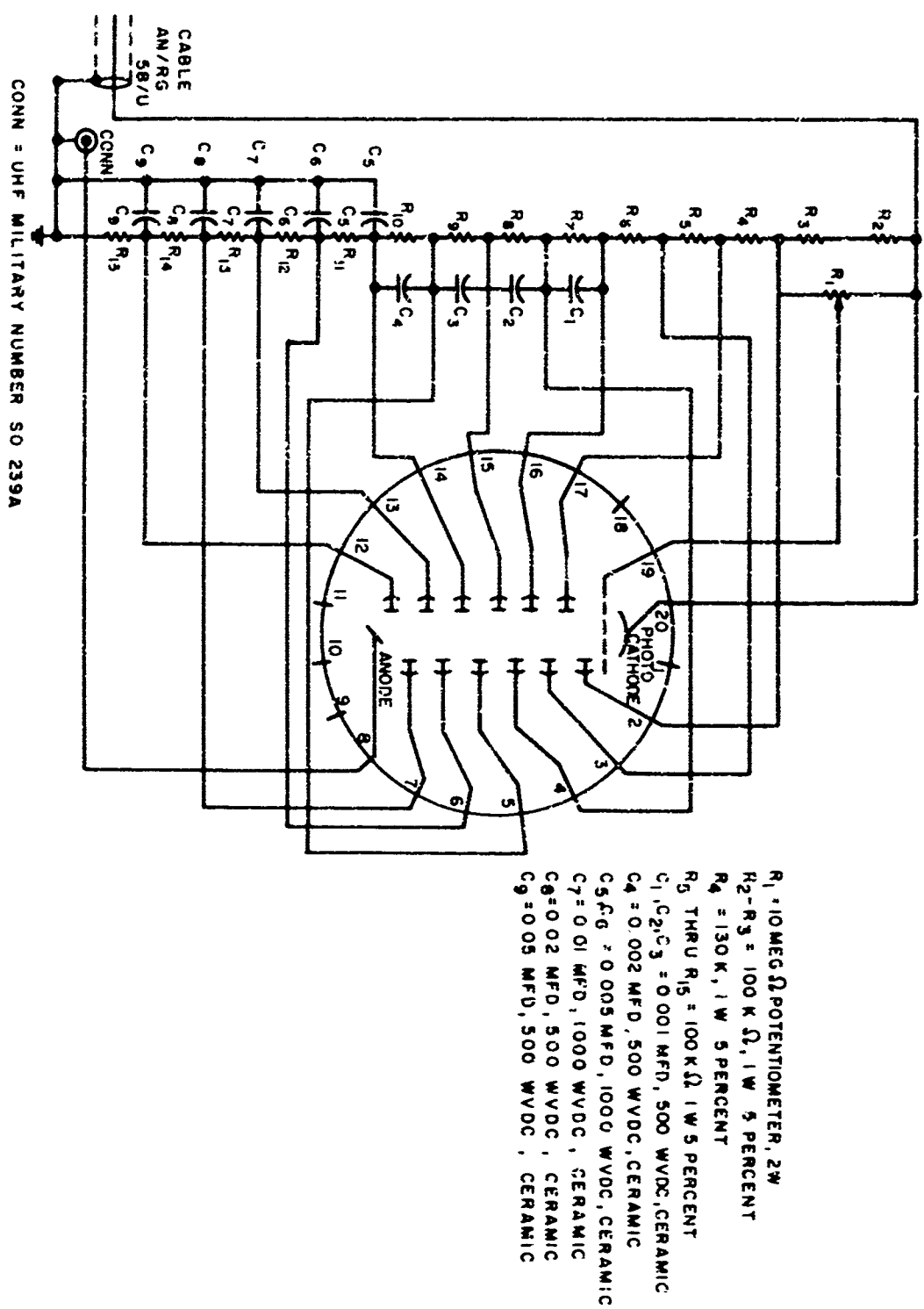


Figure 22. Schematic of PM 1

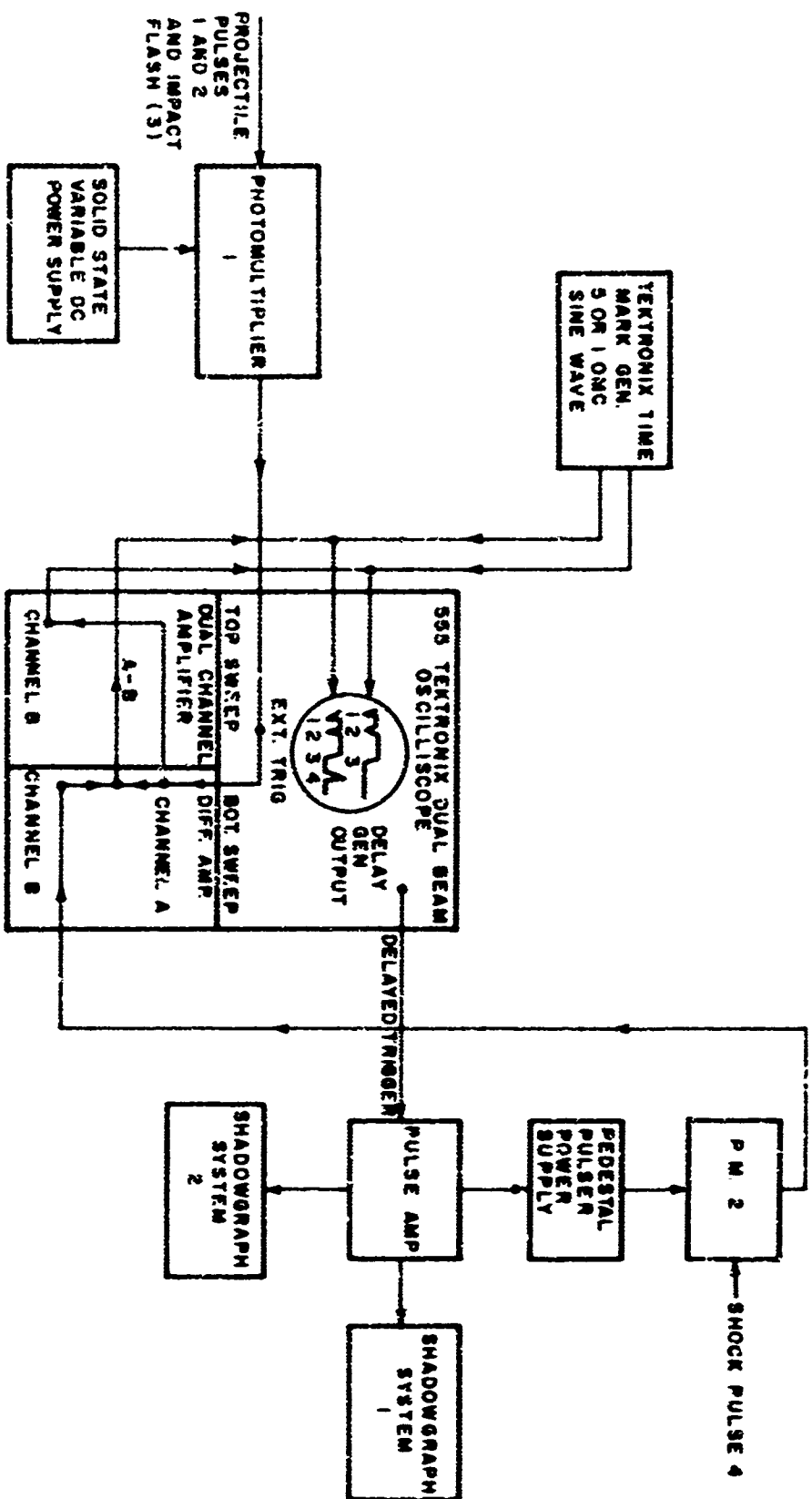


Figure 21. Block Diagram of Gruenelsen Parameter Electronics

the light pulses arrive. This difficulty was resolved by employing a pulsed mode of operation whereby the voltage dividing resistor was made a low value (950 ohms) and the high voltage was only switched on a few microseconds before the pulses so that excessive current would not injure the photomultiplier dynodes. This high voltage "pedestal pulse" is generated by a transmission-line pulse generator using a hydrogen thyratron as a switch. A schematic of the circuit and the voltage dividing network used on photomultiplier 2 are presented in figures 23 and 24.

Thus PM2 is 'turned on' prior to the arrival of the shock wave at the rear face of the target. The output of PM2 is fed to channel B of the differential amplifier where it is mixed with channel A, and the difference applied to the vertical deflection plates of the bottom sweep on the scope. The vertical deflection plates on the top sweep receive the output of PM 1.

Superimposed on the film record of a shot is a sine wave of a given frequency, which acts as the reference time system for determination of the time between pulses. A Tektronix Time Mark Generator 180-S1, which is crystal controlled, was used to generate both 5 or 10 megacycle sine waves on the film record. The frequency tolerance on the 180-S1 is 0.001 percent and the stability 3 parts in 10^6 . The unit was calibrated twice during the program with a Hewlett Packard Counter Model 524B, with the tolerance ratio between the two units being 10 to 1. The Hewlett Packard Counter is calibrated using the standard frequencies generated by the National Bureau of Standards.

The orthogonal Kerr Cell Shadowgraph Stations are used to observe the projectile in flight prior to impact to insure that the impact is planar. The Kerr Cell Shadowgraph system has been described in the literature (references 12 and 13) and will only briefly be touched

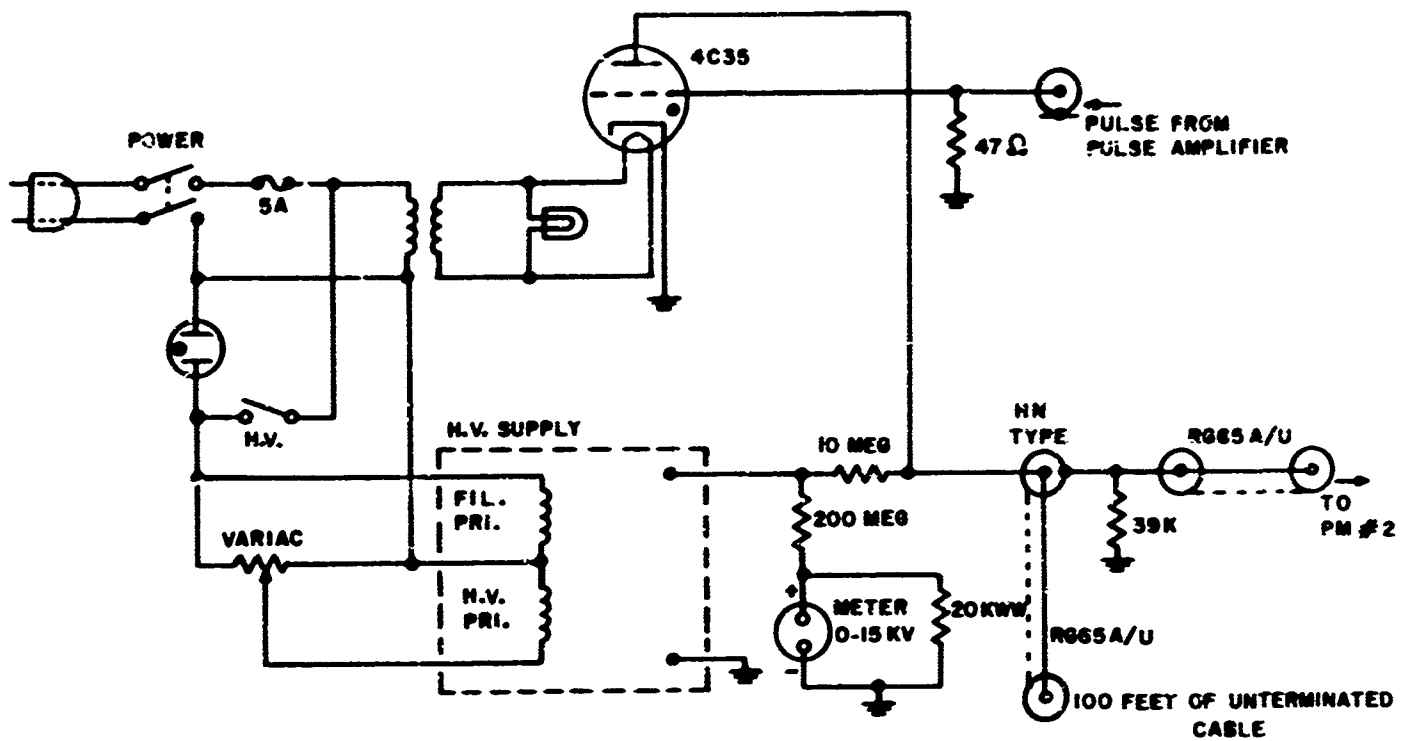


Figure 23. Schematic of Pedestal Pulser Power Supply for PM 2

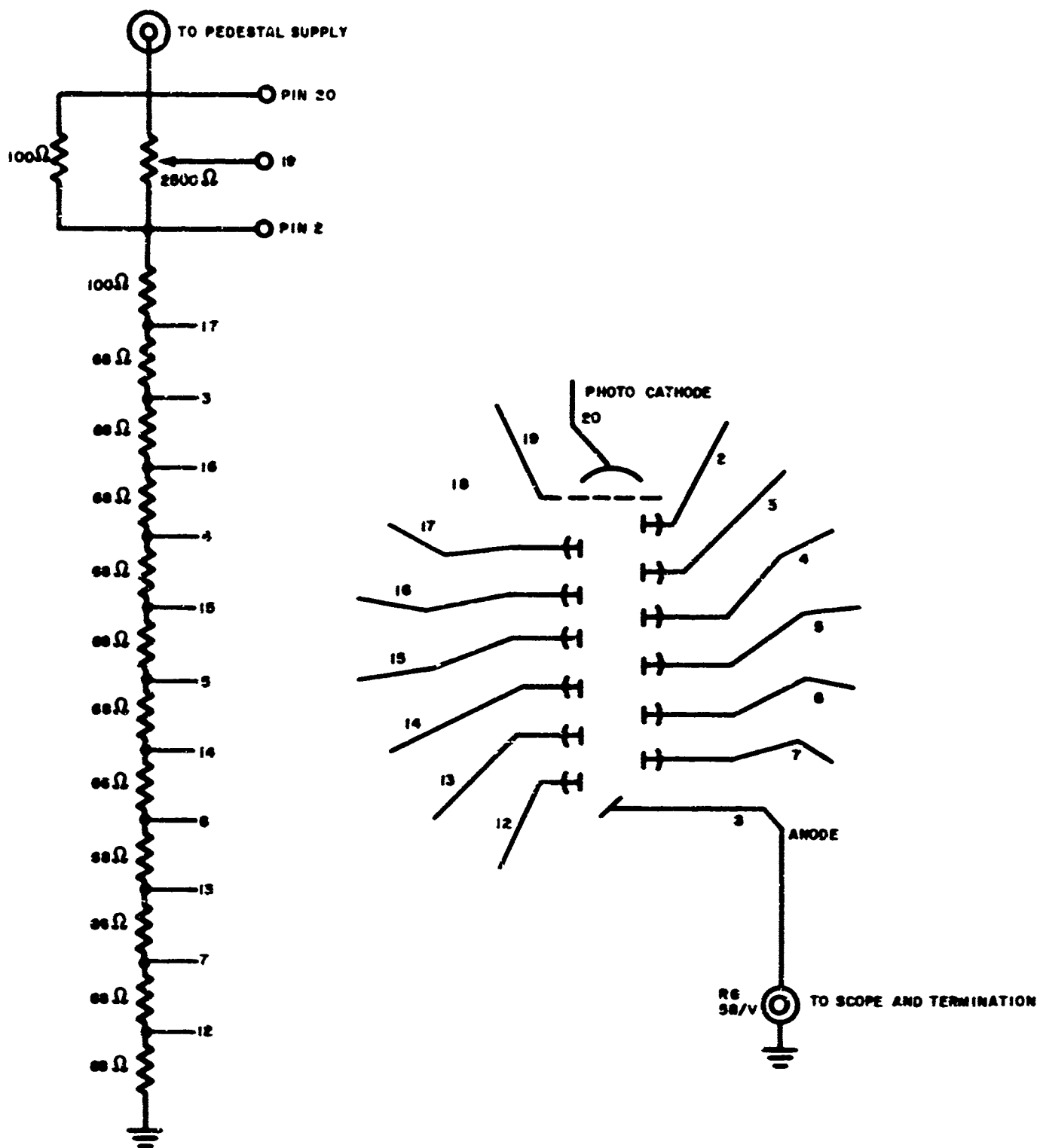


Figure 24. Schematic of PM 2

on here. Each system consists of a two-lens, collimated beam arrangement with the Kerr Cell placed at the focal length of the light source. The 1 1/4-inch-aperture Kerr Cell is pulsed by means of a transmission line pulse generator. The resulting exposure characteristic is a 50-nanosecond square wave. A triggered, series spark gap is used to switch the high voltage transmission line. This gap also acts as the light source insuring proper synchronization. The output of the pulse amplifier provides the necessary trigger to the spark gap circuitry. About 1-microsecond delay is experienced between the photomultiplier pulse and the time the Kerr Cell is triggered on. The separation distance between the projectile (at the first reflection) and the sample is greater than the distance the projectile travels in 1 microsecond for all velocities, insuring two orthogonal photographs of the projectile just prior to impact. A photograph of the overall instrumentation setup in place at the end of the range is shown in figure 25. A closeup view of the light tight enclosure housing the photomultiplier and slit assemblies is shown in figure 26.

4. Projectile Configurations

As mentioned previously, three requirements must be fulfilled in the design of a projectile to be used in shock wave measurements using guns as the accelerator. The first condition is that the thickness of the driver material be at least equal to or greater than the minimum thickness required to insure that no rarefaction wave emanating from the back face of the projectile reaches the shock front in the target before the shock velocity measurement is made. This was analyzed in Section IV.1. The second condition that must be fulfilled is the prevention of "blowby gas" from getting ahead of the projectile during the launch phase. The third condition which must be satisfied is that the projectile should be long enough so that the impact takes place with part of the projectile still in the launch tube to insure a planar impact. This section will present the designs which proved to be successful in achieving planar impacts and eliminating blowby gas.



Figure 26. View of Photomultiplier and Slit Assembly Inside Light Tight Box

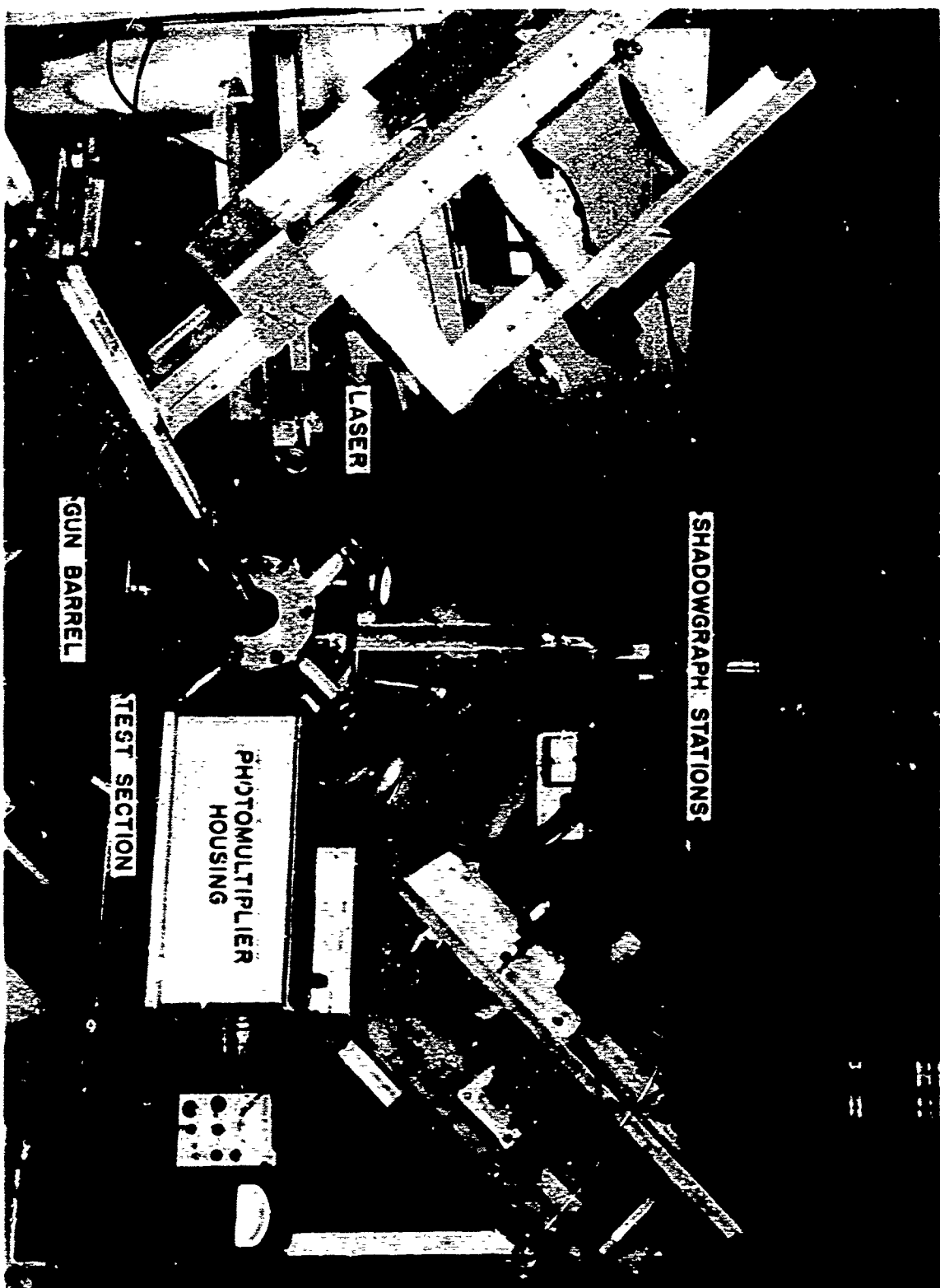


Figure 25. Apparatus for Grueneisen Parameter Study

Early trials were made with composite cylindrical projectiles using an aluminum cap over a plastic base. These proved to be unsuccessful because of gas leakage. Polyethylene and Teflon were used as the plastic material. Placing rubber O-rings on the plastic portion of the projectile was satisfactory in reducing gas leakage past the projectile for the 0.60-calibers and 1-1/2-inch powder guns. Figures 27 and 28 are a photograph and schematic respectively of the 1-1/2-inch projectile that was used with the 1-1/2-inch solid propellant gun. The projectile contained 3 O-rings on the polyethylene portion. The shear face of the projectile contained a hemispherical groove, which allowed the propelling gas to push out on the walls of the projectile, thus maintaining a seal during the launch cycle. Polyethylene was used because of its low density and plastic flow properties at high temperatures.

The designs used on the 0.060 caliber powder and light gas guns were extensions of the design shown in figures 27 and 28. Figure 29 shows schematics of the projectiles used on the 0.060 caliber guns. Design 16A was used with the 0.060-caliber powder gun. The mass of this projectile was 11 grams. Design 17A proved successful with the light gas gun up to a velocity of about 2.9 km/sec. The mass of this projectile was 15 grams. It should be noted that O-rings on the aluminum portion of the projectile were required to prevent blowby with the light gas gun. Finally, design 19a shown in figure 29 is the design that has been accelerated to 3.3 km/sec; although the front of the projectile looked somewhat deformed, this arrangement apparently seals adequately, but the solid aluminum portion of the projectile should be increased in thickness. At the time of writing, it was planned to increase the thickness to 1/2 inch.

Some conclusions can be made concerning the design of projectiles to prevent blowby gas. They are the following:

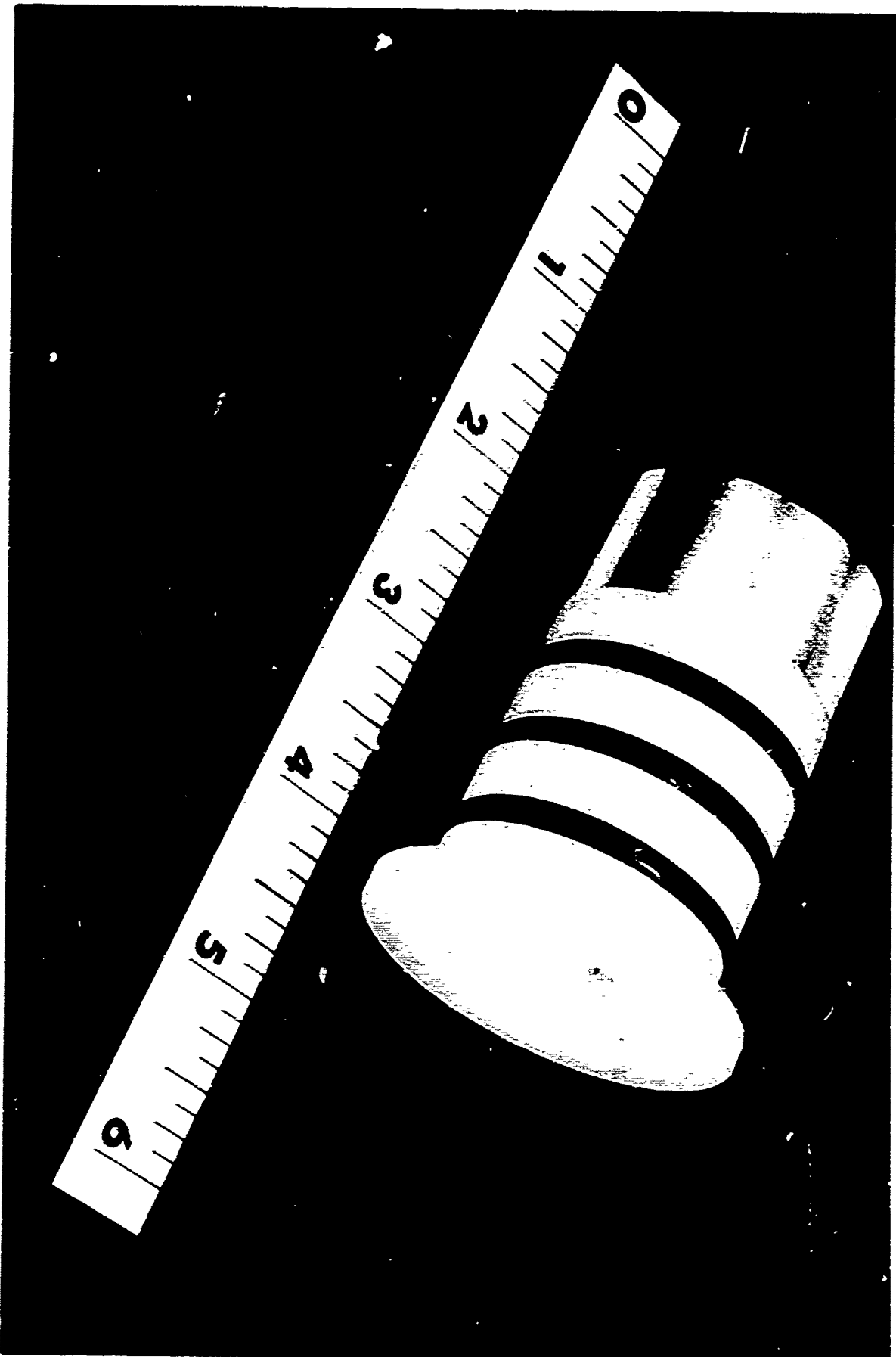


Figure 27. Photograph of 1 1/2 Inch Projectile Used on Gruenelsen Parameter Study



Figure 28. Schematic of 1 1/2 Inch Projectile Used on Grueneisen Parameter Study

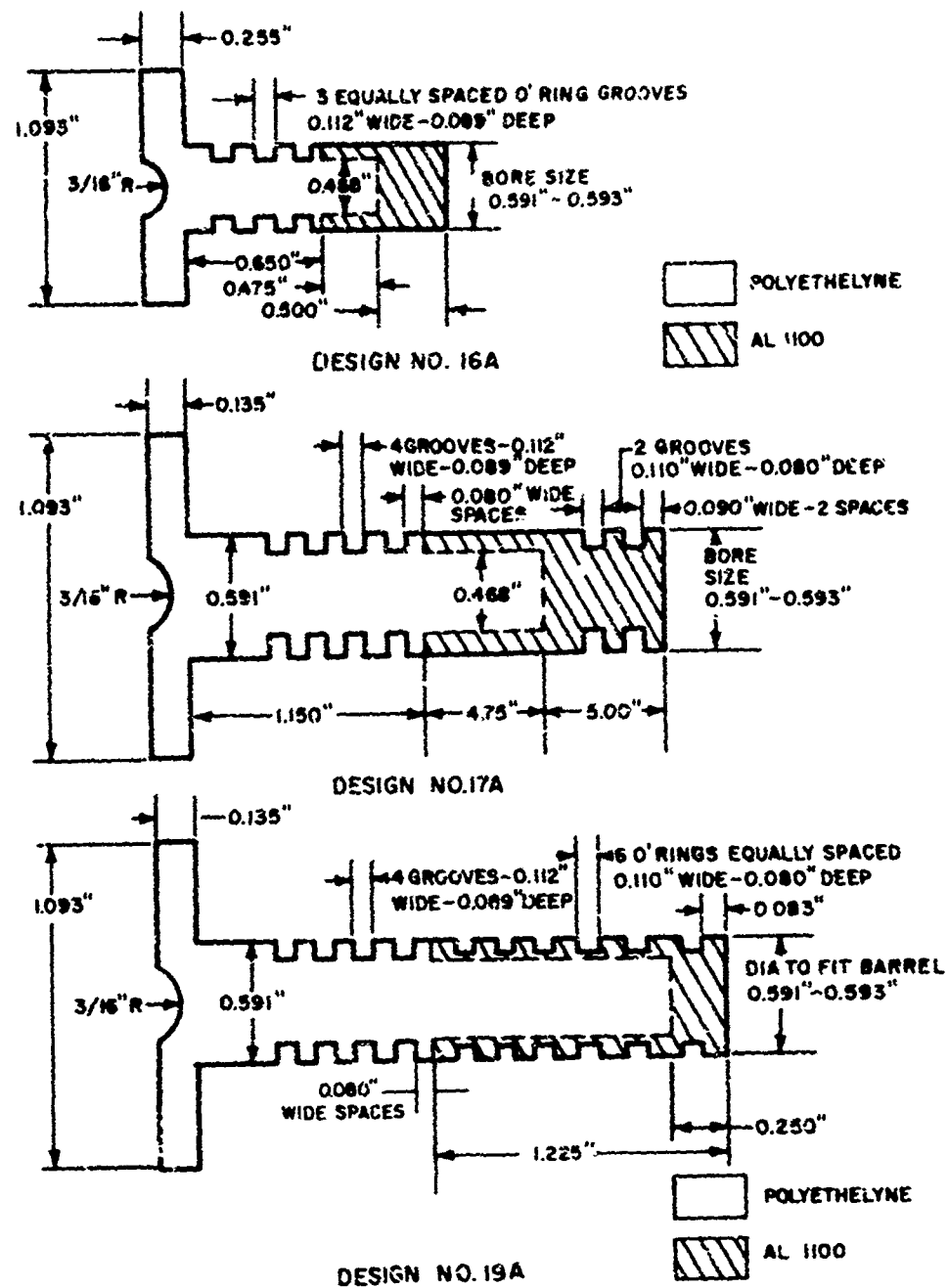


Figure 29. Schematics of 0.060 Caliber Projectiles Used on Grueneisen Parameter Study

- a. For the solid propellant gun, composite projectiles using an aluminum cap on a polyethylene base did not prevent blowby until O-rings were placed on the polyethylene.
- b. For the light gas gun, O-rings were required on both the metallic and nonmetallic portions of the projectile.
- c. The number of O-rings required increased with the driving pressure of the gas.

The problem of preventing blowby gas at velocities above 3.0 km/sec is one which will require some further development. Other materials, and configurations were only given cursory investigation due to the need to quickly obtain a design that worked. It should be emphasized that the above mentioned designs that prevented blowby gas do not represent the only solution to this problem but probably only one of several.

5. Method of Fabrication of Porous Materials

The primary feature of the determination of the solid equation of state by the method outlined in Section III is the use of open-celled porous samples along with the solid material as a means of obtaining a wide range of internal energies of a material for a given impact velocity. A range of porosities $2.20 \leq m \leq 1$ was chosen for Teflon, and $2.0 \leq m \leq 1$ was selected for aluminum. This represented a reasonable variation of internal energy without changing the discontinuous nature of the shock front. The task of fabricating open-celled porous aluminum and Teflon was undertaken by Avco RAD and this section will describe the process used to manufacture both materials.

a. Aluminum

The porous aluminum compacts were fabricated by cold-pressing and sintering aluminum powder. The powder was obtained from the Belmont Smelting and Refining Works, Inc., Brooklyn, New York. It was supplied as 325 mesh powder, i.e., the largest particles were less than 44 microns

in size. A quantitative chemical analysis of the powder was performed at RAD. The results, an average of four determinations, showed the aluminum content to be 99.6 percent with copper, iron, and manganese as the major impurities.

Two levels of porosity were necessary for the experimental program. They were 50 percent (volume) porosity, or a compact with a density of 1.35 gm/cc, and 33 percent porosity, or a compact with a density of 1.80 gm/cc. Initial attempts to press the aluminum to these densities were unsuccessful because the pressure necessary to cold-bond the aluminum powder to a free-standing shape produced densities in excess of those required for the program. To produce the necessary densities, chemical grade naphthalene powder was mixed with the aluminum powder. The mixture was cold-pressed in hardened steel dies at 30,000 psi. This technique produced free standing shapes which were of the desired density after the naphthalene was removed. For the 50 percent porosity billets, a mixture of 70 percent weight aluminum and 30 percent naphthalene was used and for the 33 percent porosity billets 85 percent aluminum - 15 percent naphthalene was used. The naphthalene was removed by heating the cold pressed shapes from room temperature to 250°C over a period of 15 hours in air. The resulting aluminum skeleton was free standing but quite fragile. The porous samples were sintered at 600°C for 15 hours in a vacuum of 5×10^{-5} to 5×10^{-4} mm Hg. This produced porous aluminum shapes with reasonable strengths but no density change occurred during sintering. This indicated that the aluminum sintered by a surface diffusion mechanism as only surface diffusion will produce a metallurgical bond without an increase in density of the compact (reference 15). Sintering did not occur in hydrogen, argon, or air indicating that the vacuum atmosphere is necessary for this particular aluminum powder.

b. Teflon

Dupont's Teflon 7 powder was used to fabricate all samples of fully dense as well as porous Teflon, and all were made from the same lot, 17224. Typically, the average particle size of this powder is 35 microns and the bulk density 250 grams per liter.

In the preparation of the samples, the powder was mixed with the calculated weight of a finely-divided leachable salt and ballmilled for 65 hours to achieve the desired uniformity of dispersion. The powder mixture was pressed at 3000 psi and then sintered at 72° F for at least 2 hours. The billet thus formed was cut into slightly oversized discs and leached. The lower density material (0.9 gm/cc) required 11 continuous days of leaching, while the higher density porous Teflon required 19 days. Periodically, the discs were removed and weighed to determine their approach to the theoretical density. When the weight change had ceased, the discs were all dried, radiographed, and tested ultrasonically. All samples submitted showed no inclusions that could be detected by X-rays. Also, there were no voids or gross areas of solid material that could be detected ultrasonically. The 0.9 gm/cc specimens did not respond to the ultrasonic test. The samples were finally machined to size and the exact densities determined. A photograph of the target samples used with the 1-1/2 inch diameter solid propellant gun is shown in figure 30.

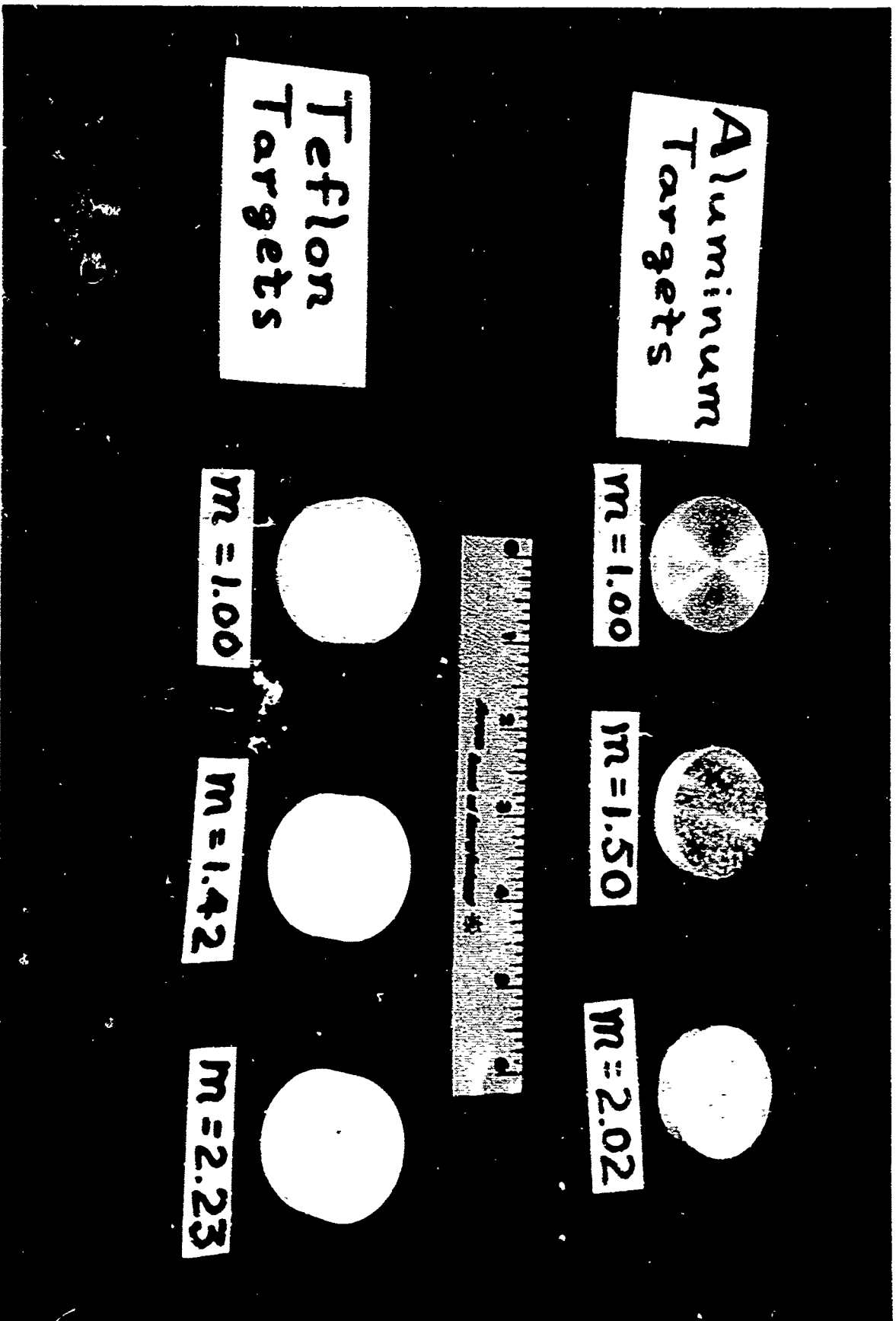


Figure 30. Photograph of 1 1/2 Inch Diameter Target Samples Used on Griseisen
Parameter Study

SECTION V

RESULTS

1. Aluminum

The data obtained on aluminum at the porosities investigated, that is $m = 1.0$, 1.50 , and 2.02 , are summarized in table II. Plots of the shock velocity as a function of the impact velocity are shown in figures 31, 32, and 33. In table II U_{f1} represents the average projectile velocity measured over the distance the projectile travels when reflecting the laser beam from slit 1 to 2 (see figure 20), and U_{f2} represents the average projectile velocity between the position where the laser beam reflects off the projectile through slit 2 until the impact plane. The average of the two velocities U_f , which was used in all the calculations, is also presented. The predicted and measured impact times are presented in the next two columns. Shots 70 through 80 did not incorporate the technique of measuring the time of impact. Finally, the shock velocity is given in the last column. The shock velocities were determined in all cases by using the measured time of impact.

The plot of the solid aluminum data shown in figure 31 shows reasonable agreement with the data obtained on 24ST by Rice (reference 3) et al. There is about 4 percent scatter in the data in the region of $U_f = 2.20$. Shots 70 through 80 were not plotted since the impact time for these data were not measured but predicted, and the uncertainties in the shock velocities were excessive in comparison to the rest of the data. In all but one case, the impact velocity and shock velocities were determined to an accuracy of ± 1 percent or better.

For all the solid aluminum cases, the pulse observed on the scope when the shock wave displaced the rear surface, passing the rear face laser beam through slit 4 onto PM2 was extremely fast rising, on the order of less than 50 nanoseconds, and was symmetrical in shape, indicating uniform rear surface motion.

Table II
SUMMARY OF DATA
ALUMINUM ON ALUMINUM
 $\rho_{\text{Al}} = 2.724 \text{ gm/cc}$

Shot No.	$\frac{\rho_{\text{Al}}}{\rho_{\text{Al}}}$	U_{11} , km/sec	U_{12} , km./sec	U_{IMPACT} , km/sec	*Predicted Impact Time μsec	Measured Impact Time μsec	Shock Vel., km/sec
70	1	1.40 \pm 0.01	1.36 \pm 0.01	1.38 \pm 0.01	11.671 \pm 0.120		6.81 \pm 0.20
71	1	1.41 \pm 0.01	1.40 \pm 0.01	1.40 \pm 0.01	11.504 \pm 0.110		6.98 \pm 0.45
72	1	1.43 \pm 0.01	1.40 \pm 0.01	1.41 \pm 0.01	11.424 \pm 0.091		6.49 \pm 0.35
73	1	1.51 \pm 0.01	1.46 \pm 0.01	1.48 \pm 0.01	10.905 \pm 0.092		6.97 \pm 0.41
74	1	1.53 \pm 0.01	1.52 \pm 0.01	1.53 \pm 0.01	10.594 \pm 0.083		6.33 \pm 0.29
75	1	1.59 \pm 0.01	1.60 \pm 0.01	1.59 \pm 0.01	10.124 \pm 0.086		6.79 \pm 0.34
77	1	1.64 \pm 0.01	1.62 \pm 0.01	1.63 \pm 0.01	9.991 \pm 0.079		6.76 \pm 0.30
80	1	1.64 \pm 0.01	1.64 \pm 0.01	1.64 \pm 0.01	9.824 \pm 0.098		6.75 \pm 0.39
89	1.50	1.62 \pm 0.01	1.65 \pm 0.01	1.64 \pm 0.01	9.867 \pm 0.098	9.938 \pm 0.015	3.23 \pm 0.03
92	1.50	1.61 \pm 0.01	1.63 \pm 0.01	1.62 \pm 0.01	9.960 \pm 0.096	10.012 \pm 0.007	2.97 \pm 0.02
93	2.02	1.61 \pm 0.01	1.64 \pm 0.01	1.63 \pm 0.01	9.932 \pm 0.099	10.039 \pm 0.005	2.63 \pm 0.02
94	2.02	1.64 \pm 0.01	1.64 \pm 0.01	1.64 \pm 0.01	9.836 \pm 0.098	9.812 \pm 0.009	2.65 \pm 0.01
96	1	1.50 \pm 0.01	1.51 \pm 0.01	1.50 \pm 0.01	5.490 \pm 0.055	5.475 \pm 0.005	6.17 \pm 0.04
102	1	2.21 \pm 0.02	2.16 \pm 0.02	2.18 \pm 0.02	3.728 \pm 0.037	3.823 \pm 0.008	7.07 \pm 0.11
103	1	2.31 \pm 0.02	2.28 \pm 0.02	2.30 \pm 0.02	3.578 \pm 0.036	3.622 \pm 0.005	7.09 \pm 0.04
104	1	2.09 \pm 0.02	2.03 \pm 0.02	2.06 \pm 0.02	3.954 \pm 0.040	4.065 \pm 0.005	6.92 \pm 0.04
105	1.50	2.06 \pm 0.02	2.03 \pm 0.02	2.04 \pm 0.02	4.015 \pm 0.040	4.076 \pm 0.005	3.94 \pm 0.02
106	1.50	2.25 \pm 0.02	2.25 \pm 0.02	2.25 \pm 0.02	3.671 \pm 0.035	3.670 \pm 0.005	4.28 \pm 0.03
120	2.02	2.31 \pm 0.02	2.27 \pm 0.02	2.29 \pm 0.02	3.574 \pm 0.035	3.632 \pm 0.005	3.50 \pm 0.03
146	1.0	1.81 \pm 0.02	1.81 \pm 0.02	1.81 \pm 0.02	5.249 \pm 0.050	5.275 \pm 0.020	6.46 \pm 0.13
149	1.0	2.88 \pm 0.02	2.86 \pm 0.02	2.87 \pm 0.02	3.309 \pm 0.033	3.328 \pm 0.005	7.14 \pm 0.05
151	1.0	2.27 \pm 0.02	2.18 \pm 0.02	2.22 \pm 0.02	4.187 \pm 0.042	4.377 \pm 0.005	6.79 \pm 0.04
152*	1.0		2.43 \pm 0.02	2.43 \pm 0.02			7.03 \pm 0.05
154	1.0	2.70 \pm 0.02	2.67 \pm 0.02	2.68 \pm 0.02	3.529 \pm 0.035	3.569 \pm 0.005	7.24 \pm 0.0
155	1.50	2.91 \pm 0.02	2.81 \pm 0.02	2.86 \pm 0.02	3.270 \pm 0.033	3.393 \pm 0.005	5.00 \pm 0.04
156	2.02	2.98 \pm 0.02	2.88 \pm 0.02	2.93 \pm 0.02	3.200 \pm 0.032	3.305 \pm 0.005	4.38 \pm 0.03

*From the position of the projectile when the second laser pulse is received, to impact.

†Ratio of the density of solid to porous material.

‡Only second pulse and impact flash recorded on shot 152.

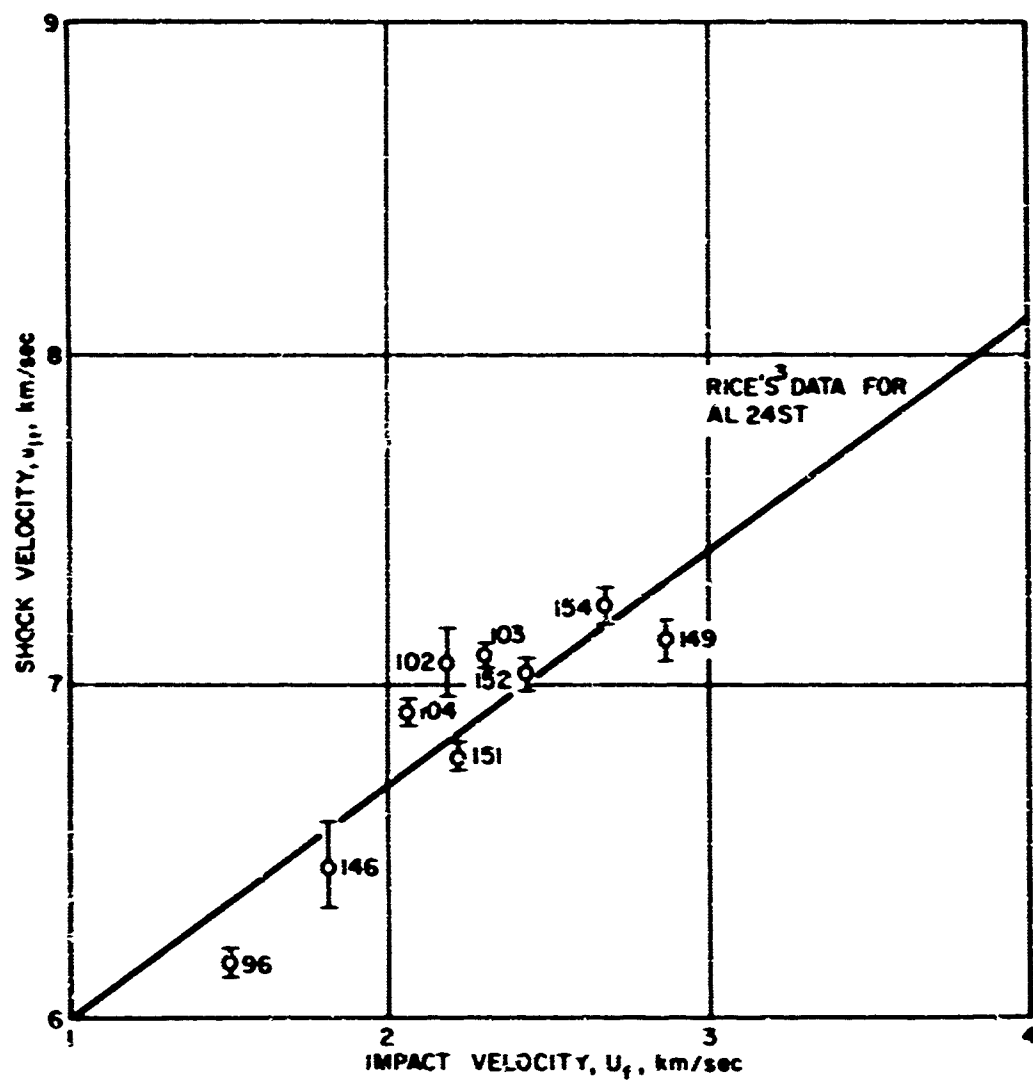


Figure 31. Shock Velocity Versus Projectile Impact Velocity for Al - Al, $m = 1$

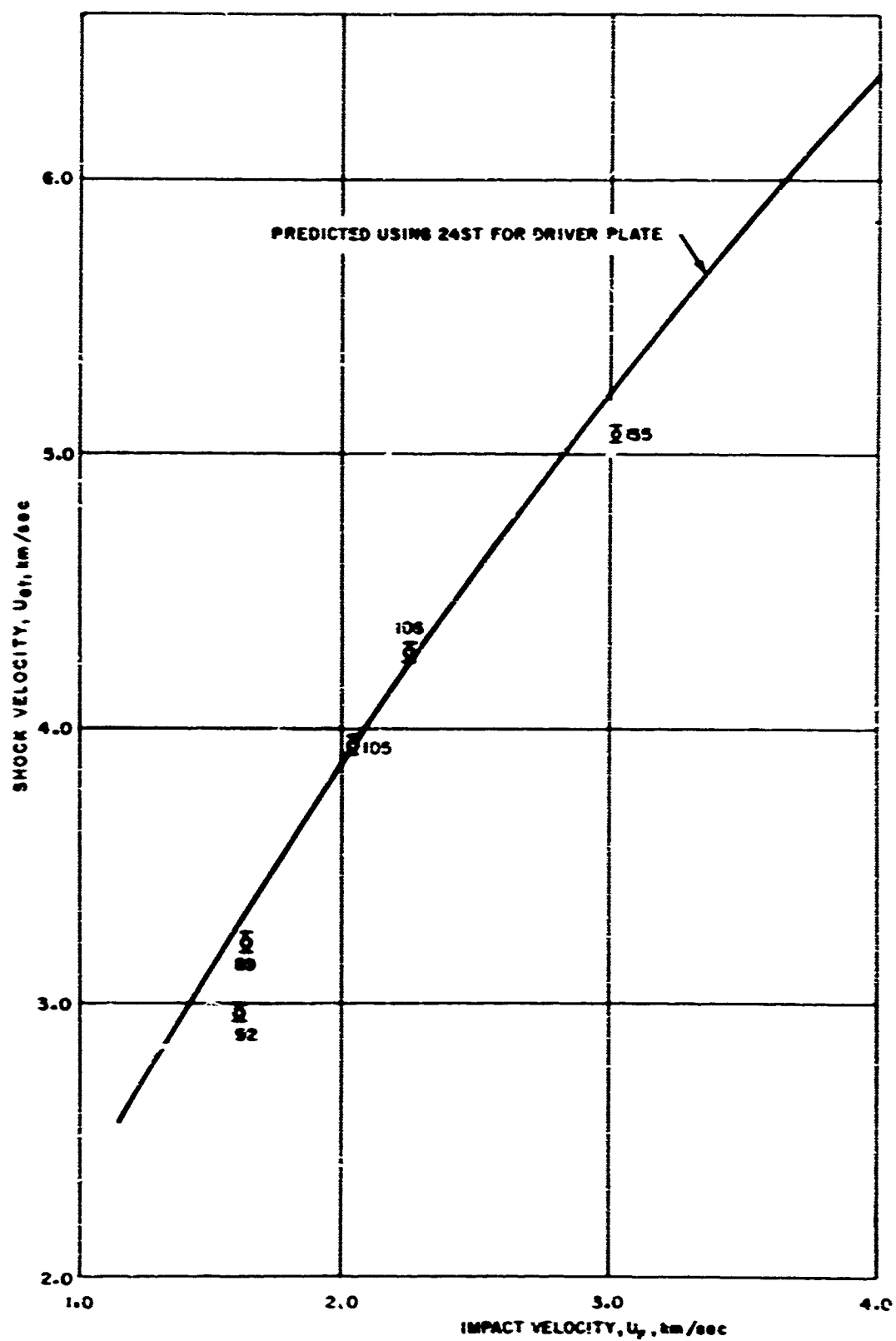


Figure 32. Shock Velocity Versus Projectile Impact Velocity for Al 1100 on Porous Al, $n = 1.5$

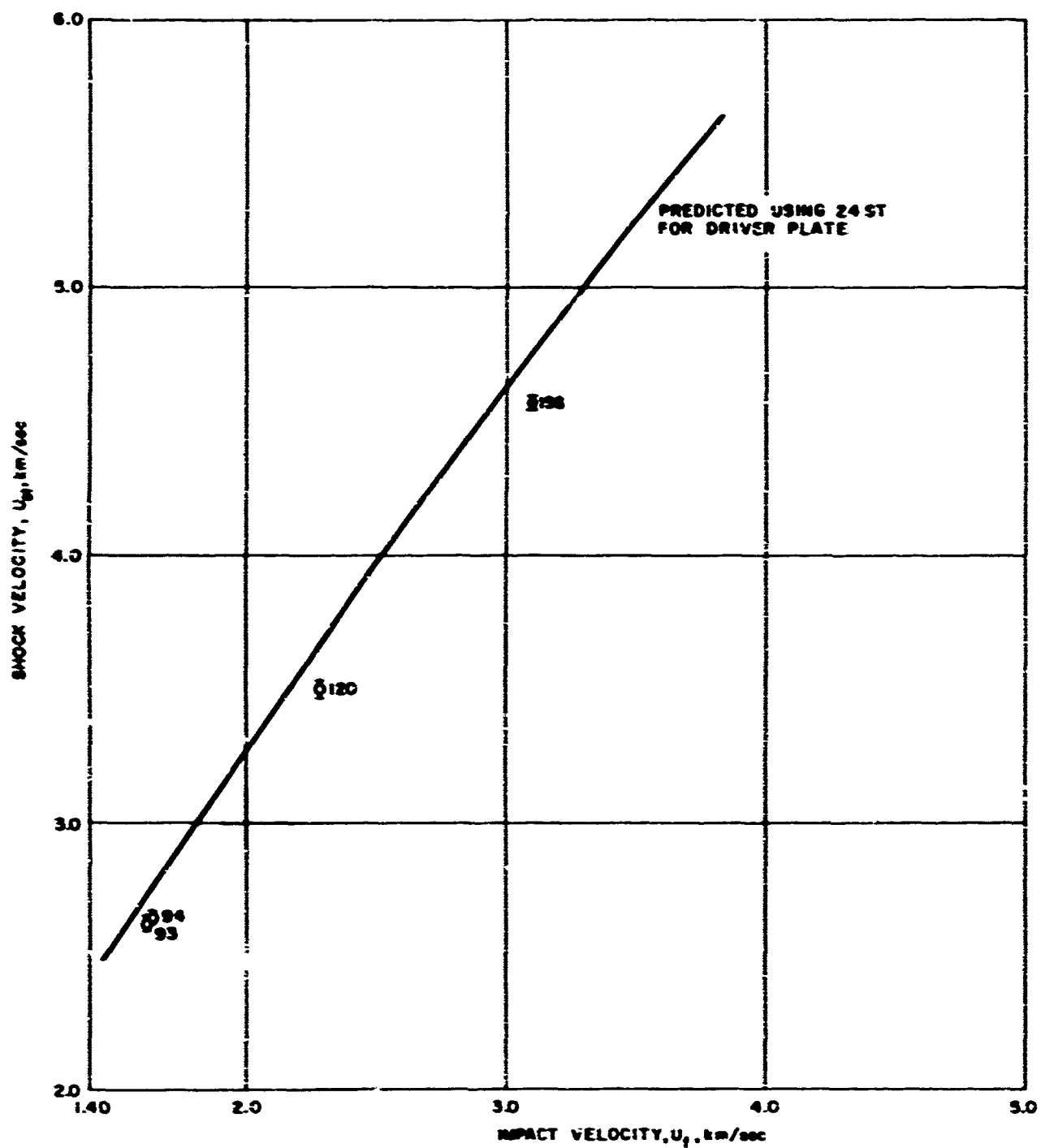


Figure 33. Shock Velocity Versus Projectile Impact Velocity for Al 1100 Porous
Al, $n = 2.02$

From the shock pulse, one can get an indication of the nature of the rear surface motion. The overall conclusion concerning the target rear surface motion for solid aluminum is that it occurs as an abrupt discontinuity and is uniform in velocity, as near as one can determine from the nature of the shock pulse.

Figure 32 shows the data obtained on porous aluminum ($m = 1.50$) along with a predicted curve calculated using 24ST aluminum as the driver plate and Rice's derived Hugoniot for the 24ST. There is very good agreement between the predicted curve and experimental data for this case.

The nature of the shock pulses observed for this material when the laser beam was reflected directly off the back face was significantly different from the solid aluminum, as one might expect. It became obvious early in the program that in order to obtain sufficient reflected light off the back face of the porous materials, it would be necessary to provide a better reflecting surface than the open-celled porous back. Thus, a small piece of 1-mil-thick brass shim was bonded to the back face of the porous sample, and the laser beam reflected off the brass. For the data at 2 km/sec and above, the shock pulse has a fast rise time, comparable to the solid aluminum, and is also symmetrical in shape. The two shots at about 1.61 km/sec have different pulse shapes, which does not allow any conclusion to be made. Shot 92 has a slow rise time on the order of 0.20 μ sec and is reasonably symmetrical in shape, whereas shot 89 has a faster rise time, on the order of 50 nanoseconds, but is weak in amplitude not allowing a comment on its shape.

Thus for porous aluminum ($m = 1.50$) at 2 km/sec and above, the rear surface motion appears to begin in an abrupt discontinuous fashion, and is reasonably uniform over the distance that the rear surface moves in the time the rear face beam sweeps the slit 4.

The data for aluminum of porosity $m = 2.02$ are shown in figure 33. A linear fit to the data is quite reasonable, with the fit lying below the predicted curve using 24ST aluminum.

The characteristics of the shock pulse observed for the most porous aluminum were similar in nature to those observed for solid aluminum, that is, extremely fast rise times and symmetrical in shape.

Thus the overall conclusions concerning the aluminum data at the three porosities investigated over the range covered are the following:

- a. The shock velocity versus impact velocity data reasonably agrees with the predicted curves using 24ST aluminum as the driver material.
- b. The nature of the shock pulse observed, which is a qualitative indication of the rear surface motion over a very short distance, 0.010 in., is quite similar in shape for all porosities, that is it has a fast rise time, on the order of 50 nanoseconds, and is symmetrical. This suggests a consistency, for all three porosities, in the mechanism which causes the rear surface to move when the shock reaches it. The shock pulse shape observed indicates for all porosities that the rear surface goes from rest to some velocity in an abrupt discontinuous fashion, and that the rear surface motion is uniform, at least over the short distance that it can be observed.

The next paragraph will discuss the results obtained on Teflon.

2. Teflon

The data obtained on Teflon at the porosities investigated, that is $m = 1.0$, 1.42, and 2.23, are summarized in table III. Plots of the shock velocity as a function of impact velocity are shown in figures 34, 35, and 36.

The plot of the solid Teflon data looks consistent over of the range of conditions covered. The data lie above the predicted curve obtained using 24ST aluminum as the driver plate. The predicted curves were calculated by using the Teflon equation of state presented in reference 14.

The shock pulse observed for the solid Teflon was low in amplitude, when the observation was made directly off the Teflon rear surface. One-mil brass

Table III
SUMMARY OF DATA
1100 AL - TEFLON - $\mu_{cr} = 2.18 \pm 0.01$

Shot No.	$\rho_{cr} = \frac{\rho_{cr}}{\rho_{cr}}$	U_{f1} km/sec	U_{f2} km/sec	U_f km/sec	*Predicted Impact Time μ sec	Measured Impact Time μ sec	Shock Velocity km/sec
76	1	1.31 ± 0.01	1.36 ± 0.01	1.33 ± 0.01	12.109 ± 0.131		3.42 ± 0.13
81	1	1.62 ± 0.01	1.59 ± 0.01	1.61 ± 0.01	10.043 ± 0.125	9.910 ± 0.044	3.73 ± 0.10
84	1.42	1.66 ± 0.01	1.64 ± 0.01	1.65 ± 0.01	9.775 ± 0.097	9.803 ± 0.010	2.99 ± 0.06
86	1.42	1.6 ± 0.01	1.64 ± 0.01	1.63 ± 0.01	9.926 ± 0.093	9.841 ± 0.013	3.10 ± 0.07
87	2.23	1.66 ± 0.01	1.67 ± 0.01	1.66 ± 0.01	9.717 ± 0.097	9.685 ± 0.023	2.41 ± 0.02
88	1.42	1.62 ± 0.01	1.64 ± 0.01	1.63 ± 0.01	9.915 ± 0.099	9.842 ± 0.005	3.24 ± 0.17
95	2.23	1.61 ± 0.01	1.62 ± 0.01	1.61 ± 0.01	10.005 ± 0.100	9.906 ± 0.006	2.51 ± 0.05
107	1	1.87 ± 0.01	1.89 ± 0.01	1.88 ± 0.01	4.410 ± 0.044	4.348 ± 0.005	3.84 ± 0.02
108	1	2.29 ± 0.02	2.27 ± 0.02	2.28 ± 0.02	3.606 ± 0.036	3.639 ± 0.005	4.33 ± 0.03
113	1.42	2.03 ± 0.02	1.99 ± 0.02	2.00 ± 0.02	4.066 ± 0.041	4.171 ± 0.005	3.52 ± 0.12
114	1.42	2.30 ± 0.02	2.36 ± 0.02	2.34 ± 0.02	3.585 ± 0.036	3.502 ± 0.006	3.86 ± 0.02
115	2.23	1.97 ± 0.02	1.99 ± 0.02	1.98 ± 0.02	5.707 ± 0.057	5.680 ± 0.005	2.66 ± 0.07
116	2.23	2.26 ± 0.02	2.25 ± 0.02	2.25 ± 0.02	3.645 ± 0.036	3.675 ± 0.005	3.54 ± 0.12
131	1	2.96 ± 0.02	2.90 ± 0.02	2.93 ± 0.02	3.215 ± 0.032	3.290 ± 0.005	4.90 ± 0.06
150	1.42	2.90 ± 0.02	2.85 ± 0.02	2.87 ± 0.02	3.289 ± 0.033	3.344 ± 0.007	4.10 ± 0.03
158	2.23	2.91 ± 0.02	2.94 ± 0.02	2.93 ± 0.02	3.275 ± 0.033	3.237 ± 0.005	3.86 ± 0.02

* From the position of the projectile when the second laser pulse is received, to impact.

+ Ratio of the density of solid to porous material.

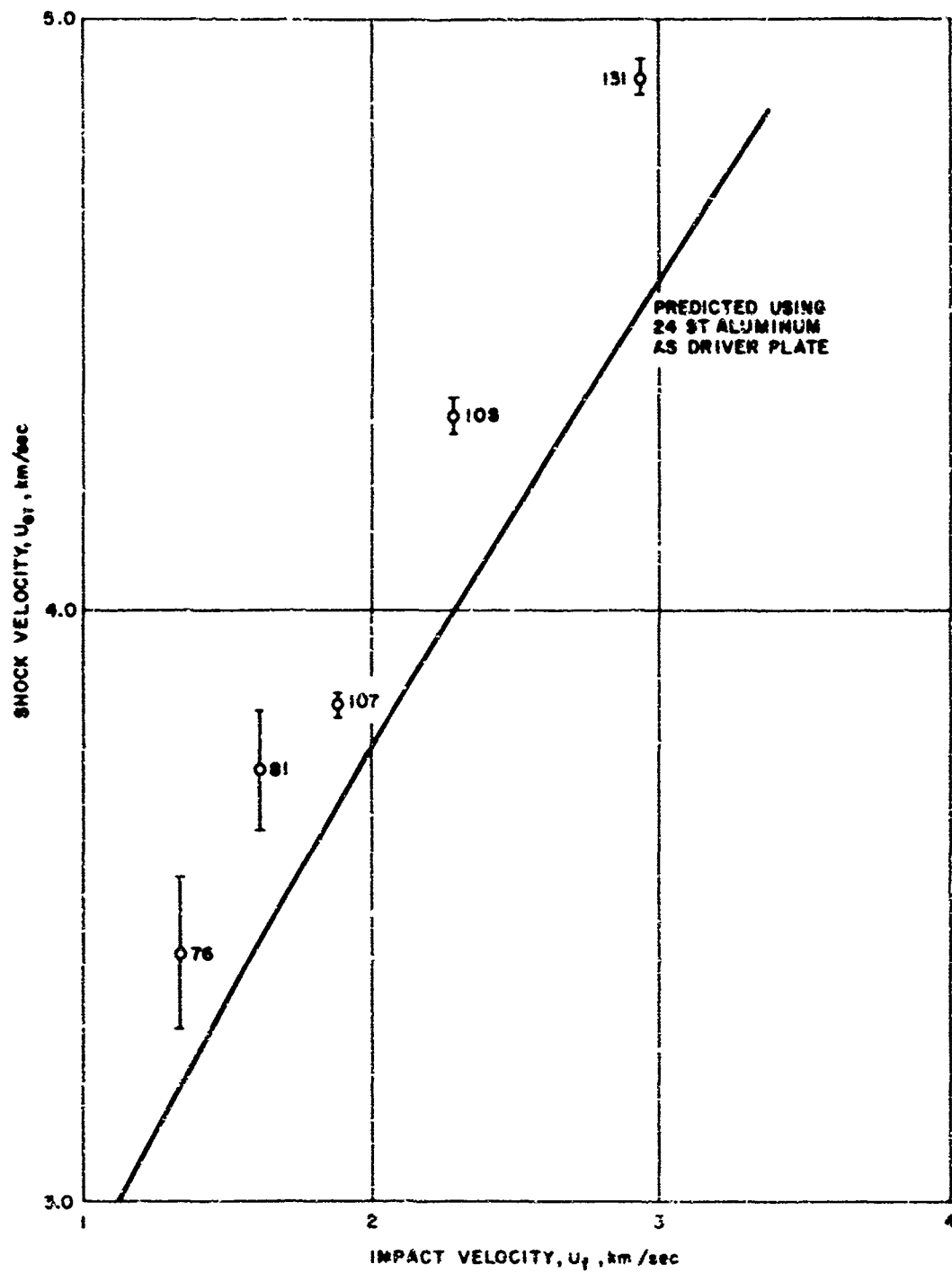


Figure 34. Shock Velocity Versus Projectile Impact Velocity for Al 1100 on Teflon, $m = 1.0$

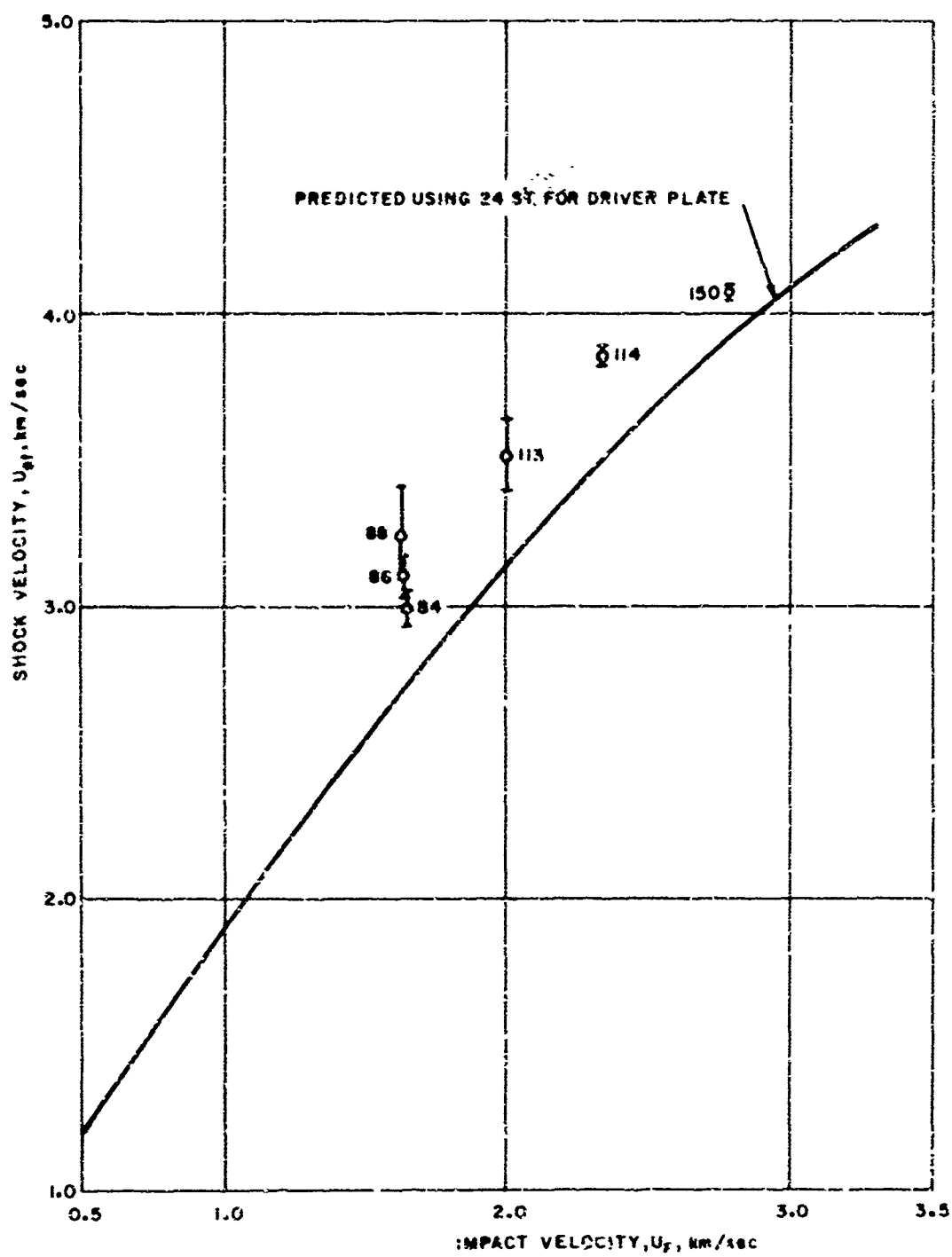


Figure 35. Shock Velocity Versus Projectile Impact Velocity for Al 1100 on Porous Teflon, $n = 1.42$

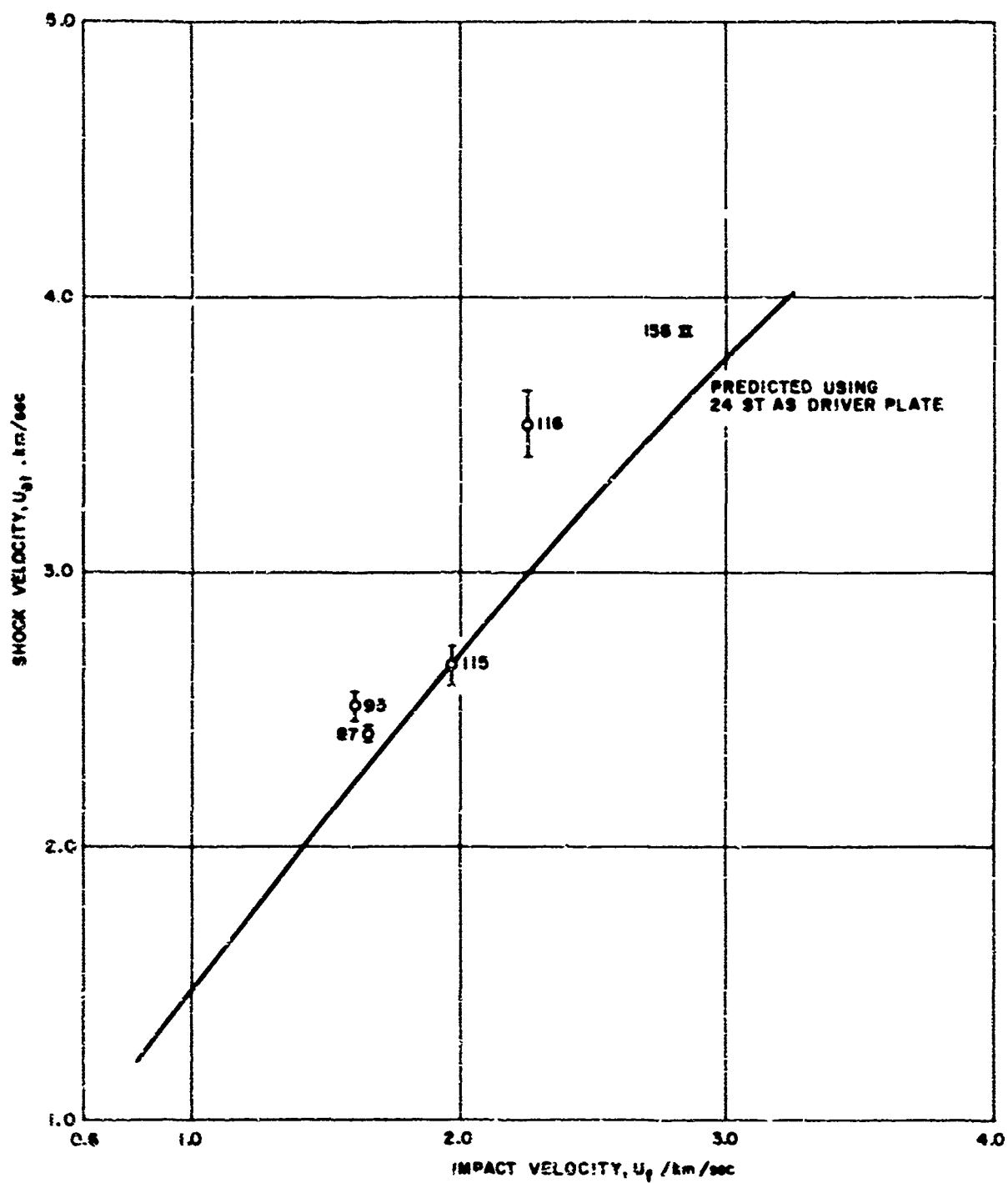


Figure 36. Shock Velocity Versus Projectile Impact Velocity for Al 1100 on Porous Teflon, $n = 2.23$

shim stock was bonded to the Teflon, and the resultant shock pulses observed were considerably stronger in amplitude, indicating the reflective properties of the rear surface change after shock compression. The nature of the shock pulses observed was similar to that experienced with aluminum, that is, fast rise times, on the order of 50 nanoseconds, and symmetrical in shape.

The data obtained on the porous Teflon ($m = 1.42$) are presented in figure 35. The trend is consistent, that is, increasing shock velocity with increasing impact velocity, with about 8 percent scatter in the data at an impact velocity of about 1.62 km/sec. The scatter in the data is due to trying to interpret the shock time of arrival from the scope traces for the data at 1.6 km/sec. The shape of the shock pulses observed for shots 84, 86, and 88, were characteristically slow on the rise portion of the pulse (on the order of $0.4 \mu\text{sec}$ from the base line to peak), and extremely fast on the fall portion of the pulse (on the order of 50 nanoseconds). This is indicative of non-uniform rear surface motion, or the existence of a pressure gradient behind the first wave reaching the back face of the target. The same shock pulse shape is evident in shot 113, at an impact velocity of 2.0 km/sec. At an impact velocity of 2.34 km/sec the shock pulse has a considerably faster rise time (on the order of $0.15 \mu\text{sec}$) and is reasonably symmetrical in shape. At 2.87 km/sec, the shock pulse is similar in nature to that observed with the solid Teflon. The data lie above the predicted curve over the range of conditions covered. All the data with the porous Teflon targets were obtained using 1-mil brass foil on the rear surface of the target.

The data obtained on porous Teflon ($m = 2.23$) are shown in figure 36. There is some scatter in the data if one considers a linear fit. It was intended to repeat shot 116 to verify it towards the end of the program, but time did not permit this.

The nature of the shock pulses observed on porous Teflon ($m = 2.23$) was similar to that discussed above for $m = 1.42$. The data between $U_i = 1.60$ and

2.25 km/sec, showed characteristically slow rise times and fast decay times for the shock pulses observed. The numbers for the rise and decay times are similar in magnitude to those obtained for $m = 1.42$ at impact velocities below 2.0 km/sec. At $U_i = 2.93$ km/sec, the shock pulse has a rise time of about $0.1 \mu\text{sec}$. Nothing can be concluded about the symmetry of the shock pulse for this case, because almost immediately following the peak of the pulse, a slow rising, continuous pulse appears, indicative of a large burst of radiation emanating from a point which was originally at the target rear face, but at the time of the observation is somewhere within the shock-compressed material. This could be indicative of the large internal energies created in the porous samples, since this effect was not observed with the solid Teflon.

The data on Teflon can be summarized as follows:

- a. The shock velocity versus impact velocity plots show that the data in general lie above those predicted using 24ST aluminum, i.e., for a given impact velocity, the measured shock velocity was greater than the predicted. This is probably due to uncertainties in the Teflon Hugoniot rather than the 24ST aluminum.
- b. The shock pulses observed for solid Teflon were quite similar in nature to those observed for aluminum, that is, fast rise times on the order of 50 nanoseconds, and symmetrical in shape, suggesting that the motion of the rear surface goes from rest to some value in a discontinuous fashion and is uniform over the slit distance.
- c. The shock pulses observed for porous Teflon varied with impact velocity and porosity. For $m = 1.42$, and for impact velocities up to $U_i = 2.0$ km/sec, the shock pulse was asymmetrical in shape, with slow rise times, on the order of $0.4 \mu\text{sec}$, and fast decay times, on the order of 50 nanoseconds. This is indicative of nonuniform rear surface motion, or the existence of a pressure gradient behind the first wave reaching the back face of the target. For $m = 1.42$, at an impact velocity of 2.87

km/sec, the shock pulse looks similar in nature to that observed with solid Teflon. For $m = 2.23$, characteristic slow rise, fast decay shock pulses were observed up to an impact velocity of 2.25 km/sec. At $U_f = 2.93$ km/sec, the shock pulse has a rise time of $0.1 \mu\text{sec}$, which is approaching that observed for compression of solid Teflon at all impact velocities.

The next section will present an analysis of the results.

SECTION VI

ANALYSIS OF RESULTS

1. Shock Velocity Versus Projectile Velocity

The basic measurements made for each data point were the projectile velocity and the shock velocity in the impacted target. In figures 37 and 38, plots are presented of the shock velocity versus projectile velocity for aluminum and Teflon respectively for each initial density used. It is seen that within the range and scatter of the data, the data are linear for each material and each initial density. For each set of data, a linear equation has been fit to the data by the method of least squares and the equations are tabulated in table IV. The lines in these figures represent these equations.

The accuracy of the curve fits is limited by the short range of projectile velocities covered and small number of data points for each material and initial density. Thus, if a larger range of projectile velocities had been covered, it is doubtful if the data would have been linear. Also, with the small number of data points for each material and initial density, an error in one data point has a large effect on the least squares curve fit even though the data points were weighted in the least squares fit by the inverse square of their estimated experimental uncertainty. As an example, the $m = 2.23$ curve for Teflon is strongly dependent on the data point for shot 158.

2. Pressure -- Volume Relationships

The equations of Section III were used with the data to calculate the pressure, P , volume, V , and internal energy, E , in the shock compressed material using the measured projectile and shock velocities comprising each data point. In these calculations, the aluminum Hugoniot for the projectile was based on measurements at Avco RAD using solid 1100 aluminum as both projectile and target. The solid aluminum Hugoniot was derived from the linear curve-fit of figure 38 and table IV:

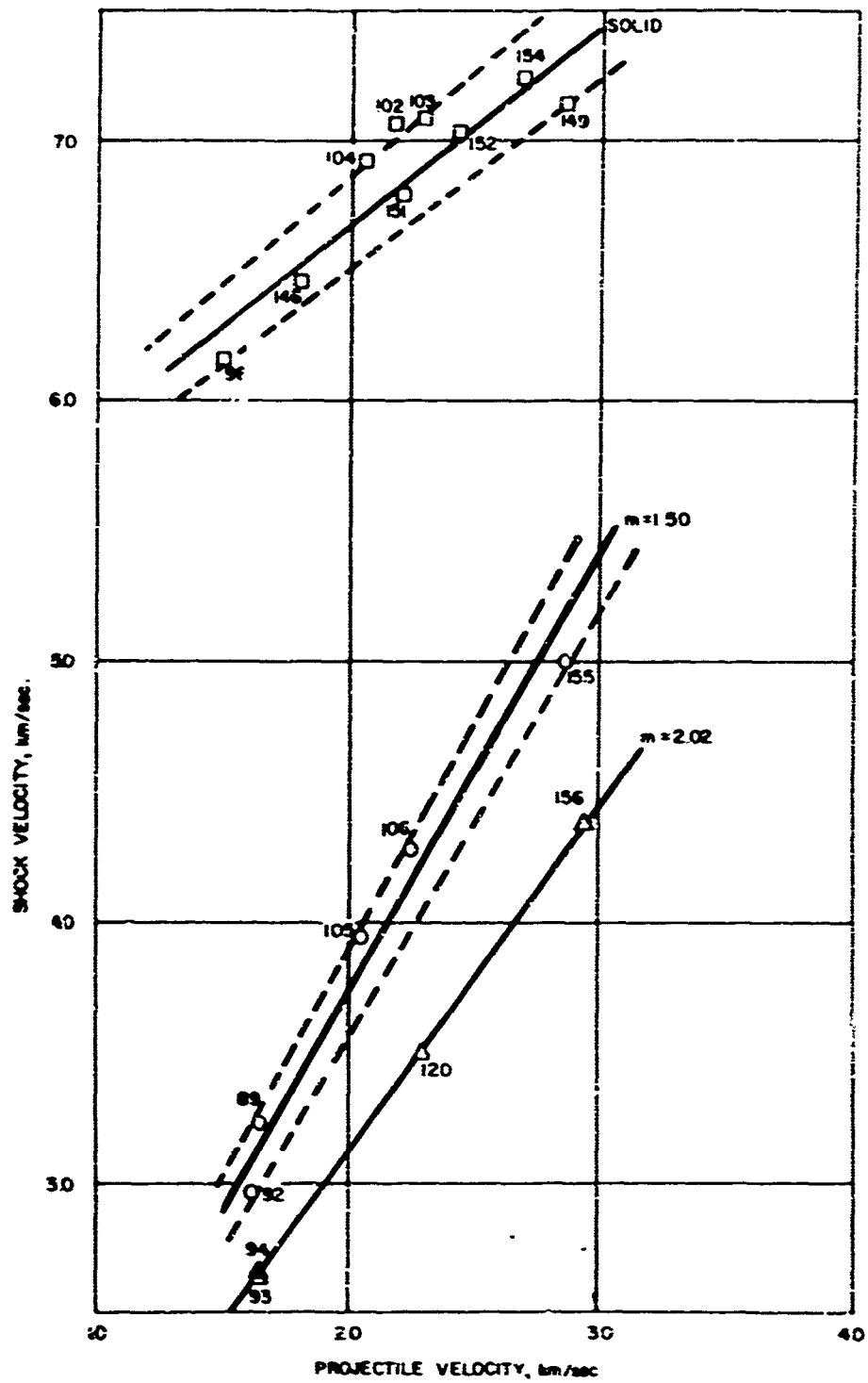


Figure 37. Shock Velocity Versus Projectile Velocity for Aluminum

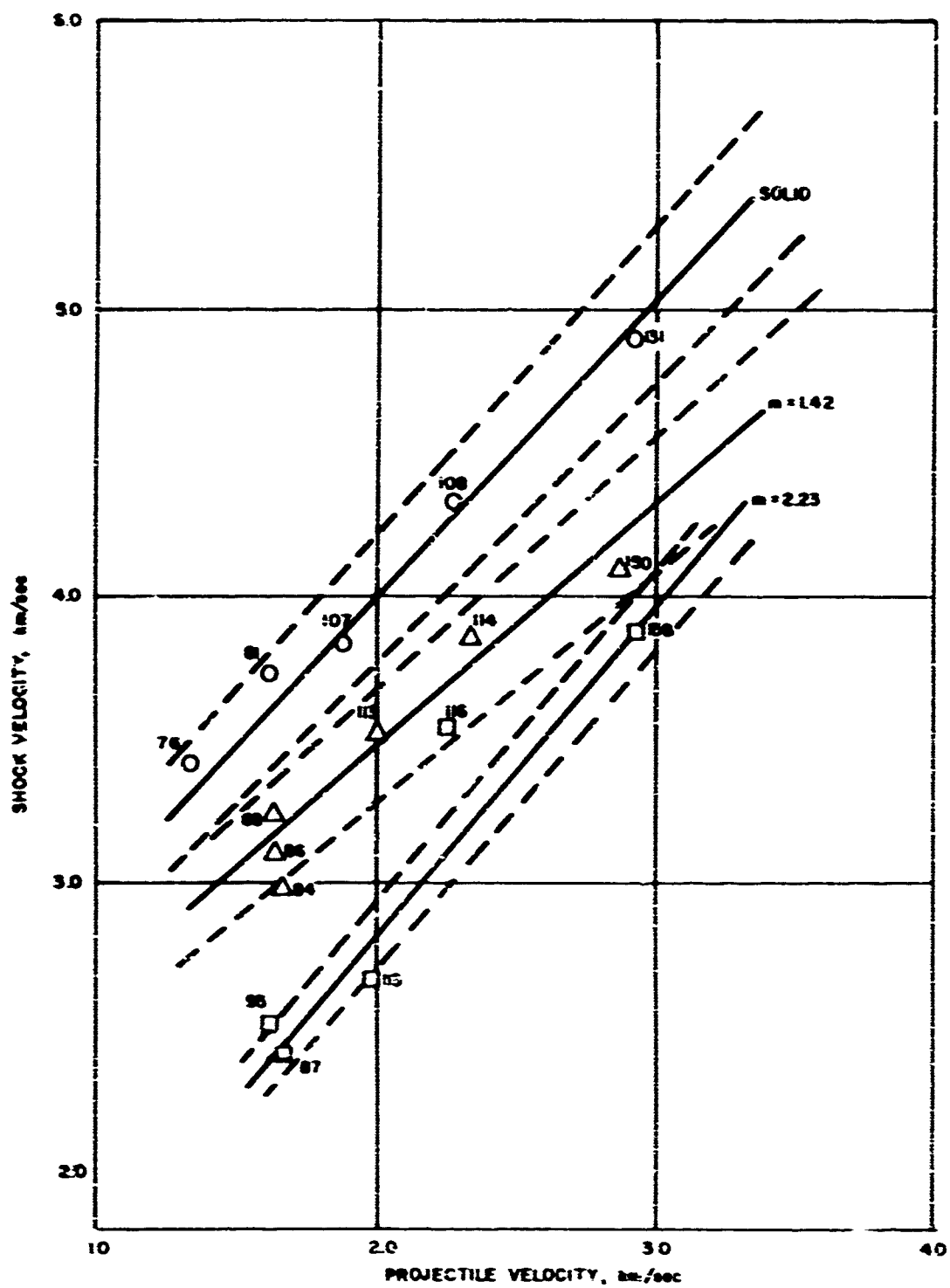


Figure 38. Shock Velocity Versus Projectile Velocity for Teflon

Table IV

LINEAR EQUATIONS GIVING SHOCK VELOCITY AS
FUNCTION OF PROJECTILE VELOCITY

Aluminum

$$m = 1.0$$

$$u_{1t} = (5.144 \pm 0.093) - (0.764 \pm 0.041) U_f \quad \text{km/sec}$$

$$m = 1.50$$

$$u_{1t} = (0.368 \pm 0.080) + (1.682 \pm 0.041) U_f \quad \text{km/sec}$$

$$m = 2.02$$

$$u_{1t} = (0.476 \pm 0.010) - (1.314 \pm 0.006) U_f \quad \text{km/sec}$$

Teflon

$$m = 1.0$$

$$u_{1t} = (1.95 \pm 0.11) + (1.019 \pm 0.054) U_f \quad \text{km/sec}$$

$$m = 1.42$$

$$u_{1t} = (1.82 \pm 0.11) - (0.829 \pm 0.045) U_f \quad \text{km/sec}$$

$$m = 2.23$$

$$u_{1t} = (0.567 \pm 0.061) - (1.125 \pm 0.029) U_f \quad \text{km/sec}$$

$$u_{1f} = a + bU_f \quad (45)$$

Assuming this linear relationship, it can be shown that the form of the equation for the Hugoniot is:

$$P = \rho_0 a^2 \frac{\mu(1+\mu)}{[1+(1-2b)\mu]^2} \quad (46)$$

With the constants given in table IV, the Hugoniot for solid aluminum is thus given as:

$$P_{H, Al} = (721 \pm 26) \frac{\mu(1+\mu)}{[1 - (0.528 \pm 0.083)\mu]^2} \text{ kilobars} \quad (47)$$

This equation was used as the projectile Hugoniot for the data reduction. The calculational procedure for calculating P , V , μ , and E for each data point is summarized in Section III. The calculated values for aluminum and Teflon are summarized in tables V and VI, respectively.

In figure 39, the pressure - volume relationship for aluminum is presented using data generated by both Avco RAD and SRI (reference 17). Also presented for comparison are the zero degree isotherm and the Hugoniot for solid aluminum reported by Altshuler (reference 18), et al. With reference to the solid state Hugoniot, the data obtained at Avco RAD on 1100 aluminum are presented with the dotted line through the points representing equation (47). It is seen that the agreement with the Soviet Hugoniot given by the solid line on both ends of the Avco RAD data is excellent.

For the porous measurements, data for $m = 2.0$ are available from both Avco RAD and SRI, the Avco RAD data being at low pressure and the SRI data being at high pressure. It is seen that the data from both sources are consistent and can be represented by the same smooth curve in both cases. The data for $m = 1.70$ from SRI are also plotted and are seen to be consistent with the data for $m = 1.40 - 1.50$ and $m = 2.0$. It should also be noted that for $m = 2.0$, the curve is very close to a vertical line at $V = V_0$, indicating that $\gamma = 2.0$ (See section III.1) so that the Grueneisen for aluminum is approximately 2.0.

Table V
CALCULATED SHOCK PARAMETERS FROM MEASURED
PROJECTILE AND SHOCK VELOCITIES FOR ALUMINUM

Proximity to	Shot No.	Measured Projectile Velocity, v_p km/sec	Measured Shock Velocity, v_s km/sec	Calculated Material Velocity, $v_m = v_s - v_p$ km/sec	Calculated Compression $\rho_t = \rho_0 - 1$	Calculated Specific Volume, v cm ³ /gm	Calculated Shock Pressure, P_s kilobars	Calculated Internal Energy, I joules/gm
10	96	1.50 ± 0.0	6.17 ± 0.11	0.77	0.1398 ± 0.0060	0.1221 ± 0.002	127.2 ± 1.5	286 ± 11
	102	2.18 ± 0.02	7.07 ± 0.04	1.072	0.1787 ± 0.0033	0.1114 ± 0.001	236.4 ± 2.2	574 ± 11
	03	2.30 ± 0.02	7.09 ± 0.04	1.156	0.1768 ± 0.0035	0.1083 ± 0.001	219.4 ± 2.2	646 ± 12
	04	2.06 ± 0.02	6.92 ± 0.02	1.016	0.1722 ± 0.0025	0.1132 ± 0.001	191.6 ± 2.1	516.5 ± 2.5
	146	1.81 ± 0.02	6.46 ± 0.13	0.969	0.1638 ± 0.0083	0.2154 ± 0.002	160.0 ± 2.	413 ± 19
	149	2.87 ± 0.02	7.34 ± 0.05	1.452	0.2553 ± 0.0053	0.2924 ± 0.001	242.4 ± 2.5	1054 ± 2
	151	2.22 ± 0.002	6.79 ± 0.04	1.117	0.1962 ± 0.0037	0.1969 ± 0.001	206.0 ± 2.2	620 ± 12
	152	2.43 ± 0.02	7.01 ± 0.05	1.213	0.2085 ± 0.0044	0.3038 ± 0.001	232.2 ± 2.3	735 ± 15
	154	2.68 ± 0.02	7.24 ± 0.05	1.336	0.2263 ± 0.0046	0.2094 ± 0.001	263.5 ± 2.4	693 ± 17
	150	1.64 ± 0.01	3.23 ± 0.03	1.197	0.0592 ± 0.0130	0.3465 ± 0.004	70.22 ± 0.66	717 ± 16
2.02	92	1.62 ± 0.01	2.97 ± 0.02	1.206	0.123 ± 0.012	0.3279 ± 0.003	65.07 ± 0.53	226 ± 13
	105	2.04 ± 0.02	3.94 ± 0.02	1.425	0.0443 ± 0.0088	0.515 ± 0.003	102.0 ± 1.1	1015 ± 19
	106	2.28 ± 0.02	4.28 ± 0.03	1.543	0.0424 ± 0.0103	0.3527 ± 0.003	119.9 ± 1.3	1190 ± 24
	155	2.56 ± 0.02	5.70 ± 0.04	1.901	0.0757 ± 0.0122	0.3413 ± 0.004	172.6 ± 1.6	1807 ± 34
	93	1.63 ± 0.01	2.63 ± 0.02	1.323	-0.0038 ± 0.0177	0.3685 ± 0.007	46.92 ± 0.41	875 ± 17
	94	1.64 ± 0.01	2.65 ± 0.01	1.329	-0.0065 ± 0.0102	0.3695 ± 0.004	47.51 ± 0.33	883 ± 11
Internal Energy Relative to 300°K	120	2.2 ± 0.02	3.50 ± 0.03	1.772	0.0630 ± 0.0211	0.3660 ± 0.005	83.66 ± 0.94	1171 ± 17
	156	2.93 ± 0.02	4.38 ± 0.03	2.179	-0.0143 ± 0.0159	0.3126 ± 0.006	128.7 ± 1.1	2374 ± 44

Table V3
CALCULATED SHOCK PARAMETERS FROM MEASURED
PROJECTILE AND SHOCK VELOCITIES FOR TEFLON

Purity in	Shot No.	Measured Projectile Velocity, V_p km/sec	Measured Shock Velocity, V_s km/sec	Calculated Material Velocity, $V_M = V_s - V_p$ km/sec	Calculated Compression $\rho_1 = \rho_0 \gamma - 1$	Calculated Specific Volume, γ cm^3/gm	Calculated Shock Pressure, P_1 kilobars	Calculated Internal Energy, E_1 joules/gm
1.90	76	1.13 ± 0.01	3.42 ± 0.13	0.903	0.359 ± 0.039	0.3375 ± 0.010	67.3 ± 1.9	408 ± 35
	81	1.61 ± 0.01	3.73 ± 0.10	1.073	0.404 ± 0.032	0.3268 ± 0.007	87.2 ± 1.7	536 ± 15
	107	1.88 ± 0.01	3.84 ± 0.02	1.251	0.4329 ± 0.0089	0.3193 ± 0.002	104.6 ± 0.70	742 ± 11
	108	2.28 ± 0.02	4.33 ± 0.03	1.473	0.518 ± 0.014	0.3023 ± 0.003	139.4 ± 1.5	1090 ± 26
	131	2.93 ± 0.02	4.90 ± 0.06	1.857	0.610 ± 0.026	0.2859 ± 0.005	1.98 ± 2.2	1324 ± 50
	142	1.95 ± 0.01	3.99 ± 0.06	1.274	0.227 ± 0.040	0.3173 ± 0.012	58.50 ± 0.99	612 ± 38
	86	1.63 ± 0.01	3.10 ± 0.07	1.249	0.179 ± 0.039	0.3889 ± 0.015	59.4 ± 1.1	780 ± 41
	88	1.63 ± 0.01	3.24 ± 0.17	1.217	0.139 ± 0.079	0.4021 ± 0.028	61.5 ± 2.5	765 ± 92
	113	2.00 ± 0.02	3.52 ± 0.12	1.498	0.226 ± 0.067	0.3743 ± 0.020	80.3 ± 2.1	1.21 ± 89
	114	2.34 ± 0.02	3.46 ± 0.02	1.724	0.272 ± 0.015	0.3605 ± 0.002	102.15 ± 0.99	1476 ± 26
2.23	150	2.87 ± 0.02	4.19 ± 0.03	2.101	0.445 ± 0.026	0.3175 ± 0.006	132.3 ± 1.2	2208 ± 15
	87	1.60 ± 0.01	2.41 ± 0.02	1.434	0.107 ± 0.031	0.4142 ± 0.012	33.78 ± 0.12	1028 ± 62
	95	1.61 ± 0.01	2.51 ± 0.05	1.383	-0.00120 ± 0.054	0.4592 ± 0.025	33.94 ± 0.62	956 ± 65
	115	1.98 ± 0.02	2.66 ± 0.07	1.691	0.231 ± 0.125	0.3726 ± 0.038	44.0 ± 1.1	1450 ± 91
	116	2.25 ± 0.02	1.54 ± 0.12	1.444	-0.0642 ± 0.075	0.4932 ± 0.039	63.8 ± 1.9	2703 ± 136
	158	2.93 ± 0.02	3.86 ± 0.02	2.379	0.169 ± 0.024	0.3924 ± 0.008	89.78 ± 0.4	2831 ± 44

Internal Energy Relative to 300°K

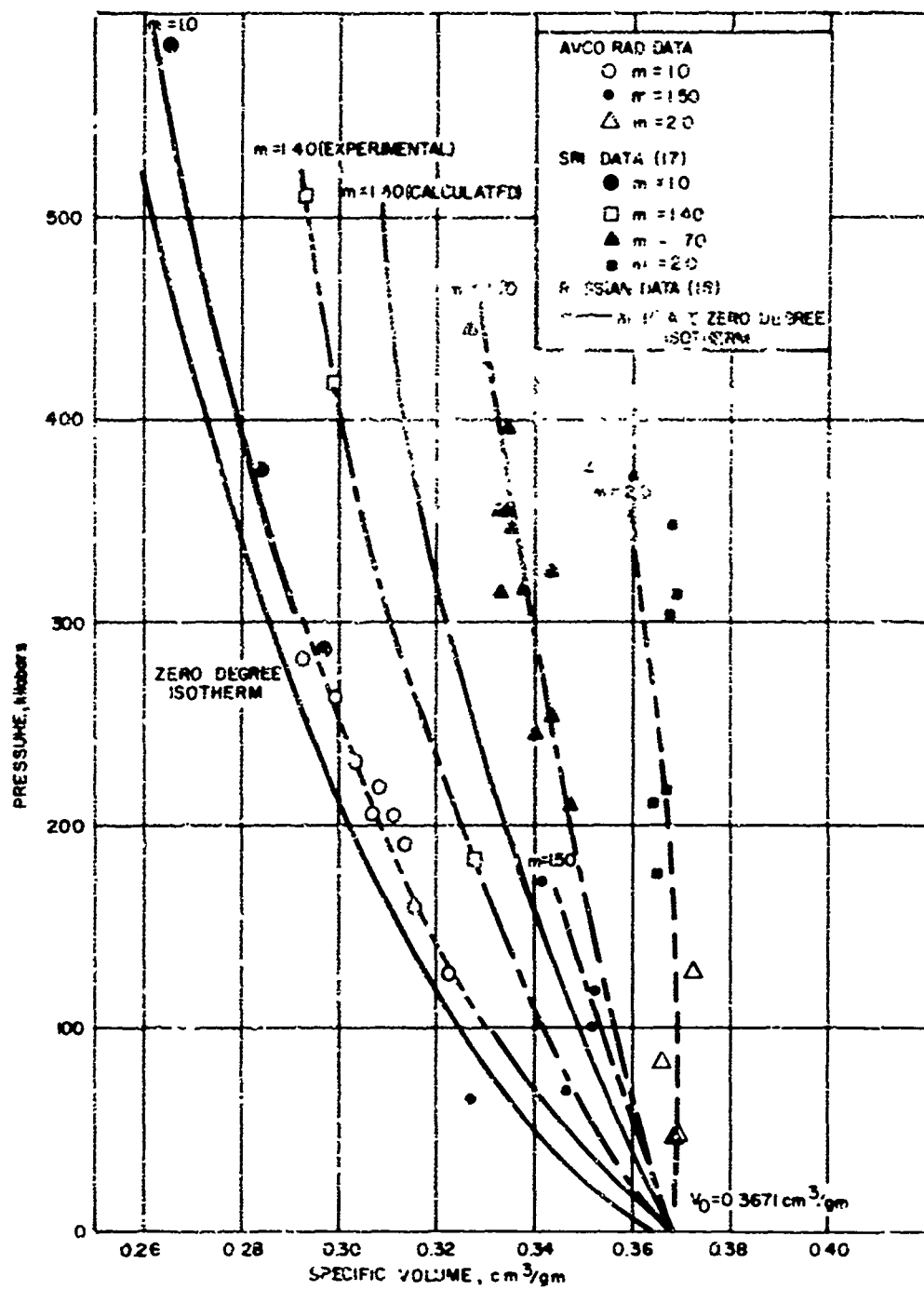


Figure 39. Pressure - Volume Relationship for Aluminum

In figure 40, the pressure - volume data for Teflon obtained at Avco RAD are presented and compared with available data from other sources. For the solid Hugoniot, the Avco RAD data are at higher pressure than previously available and cover the pressure range from 68 to 198 kilobars. Presented also are dynamic data in the lower pressure regions by Fowles and Curran (reference 19) and by Wagner (reference 20), et al.; for comparison, the static isothermal measurements of Bridgman (reference 21) are also presented. It is seen that the lower pressure data agree well with the Avco RAD data and the entire set of data are well represented by a smooth curve such as the solid line drawn through the data.

The data for porous Teflon have a relatively large scatter. For $m = 1.42$, the dotted line has been drawn through the data as a reasonable representation of the data. However, additional data points are required before the Hugoniot for $m = 1.42$ can be reliably established. For the $m = 2.23$ data, the five data points available show a very large scatter and no trend of the data is apparent. The large scatter is believed to result from the sensitivity of the calculated specific volume to small errors in the measured projectile and shock velocities at this porosity. Additional data, particularly at higher pressures, are required for this porosity before any meaningful data analysis can be made.

3. Evaluation of Grueneisen Parameter

As discussed in Section III.1, the Grueneisen parameter is defined as:

$$\Gamma = v \left(\frac{\partial P}{\partial E} \right)_v \quad (48)$$

Assuming the parameter is independent of internal energy at a given volume, this relation can be written in terms of the Hugoniot equation of state for porous and solid materials as:

$$\Gamma = v \frac{P_p - P_s}{E_p - E_s} \quad (49)$$

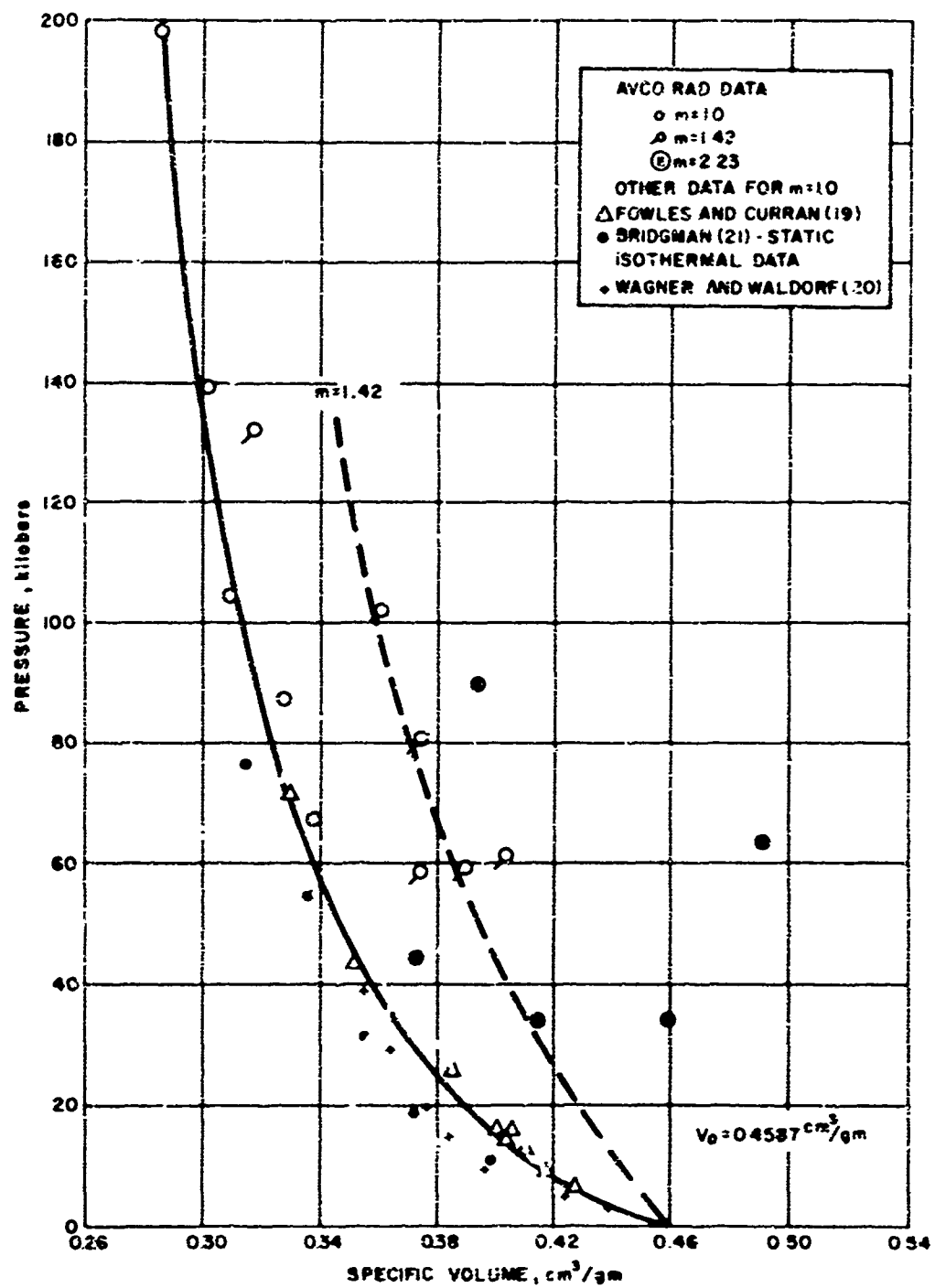


Figure 40. Pressure - Volume Relationship for Teflon

where the subscript p refers to the porous material and the subscript s to the solid material. The internal energy along the Hugoniot for the porous and solid samples can be written respectively as:

$$E_p = \frac{1}{2} P_p (m V_o - V) \quad (50a)$$

$$E_s = \frac{1}{2} P_s (V_o - V) \quad (50b)$$

The above expression can be converted to the form:

$$\Gamma = \frac{2}{\frac{V_o}{V} \frac{P_p - P_s}{P_p - P_s} - 1} \quad (51)$$

Using this relation and the curves from the plots of figures 39 and 40, the Grueneisen parameter has been calculated for aluminum and Teflon. In figure 41, the results of the parameter computations for aluminum are presented as a plot of Grueneisen parameter versus specific volume. It is seen that a different curve for each porosity is obtained and that the Grueneisen parameter for each porosity is dependent on volume. This indicates that the Grueneisen parameter for aluminum is not independent of internal energy as is frequently assumed. Presented in figure 41 also is the Grueneisen parameter reported by Rice (reference 3), et al, and based on application of the Dugdale-MacDonald relation to their Hugoniot data on solid 24ST aluminum. Presented also for comparison are two data points for porous aluminum measured at the Lawrence Radiation Laboratory and reported in reference 7.

In figure 42, a plot is presented of the experimentally determined internal energies for aluminum using both Avco RAD's data and SRI's data. The behavior of the internal energy is consistent with the expected behavior. Presented also is the zero degree (0°K) isotherm based on Altshuler (reference 18) and McCloskey (reference 23). It should be noted that the experimental internal energy difference between 0°K and 300°K at 1 atm pressure should be added

to the data points if they are to be consistent with the 0°K isotherm, that is have the same reference state. McCloskey (reference 23) has reported this internal energy difference to be 160 joules/gram.

Krupnikov (reference 1) in analyzing data for porous tungsten found that E_{th} was a function of only, VP_{th} and could be represented by the following equation:

$$E_{th} = a (VP_{th}) + b (VP_{th})^2 \quad (52)$$

Using this relation, the Grueneisen parameter could then be derived as follows:

$$\Gamma = V \left(\frac{\partial P_{th}}{\partial E_{th}} \right)_V \quad (53)$$

$$\left(\frac{\partial E_{th}}{\partial P_{th}} \right)_V = a V + 2 b V^2 P_{th} \quad (54)$$

Thus,

$$\Gamma = \frac{1}{a + 2 b V P_{th}} \quad (55)$$

Since VP_{th} is a function of E_{th} only, this relation implies that Γ is a function only of E_{th} .

This procedure was followed in the present case using the aluminum data plotted at porosities of $m=1.59$, 1.70 and 2.02 in figures 39 and 42. The calculation was made as follows:

- a. A value of V was assumed.
- b. From figure 39, the pressure, P , on the Hugoniot for the porous material and the pressure, P , on the zero degree isotherm were read.

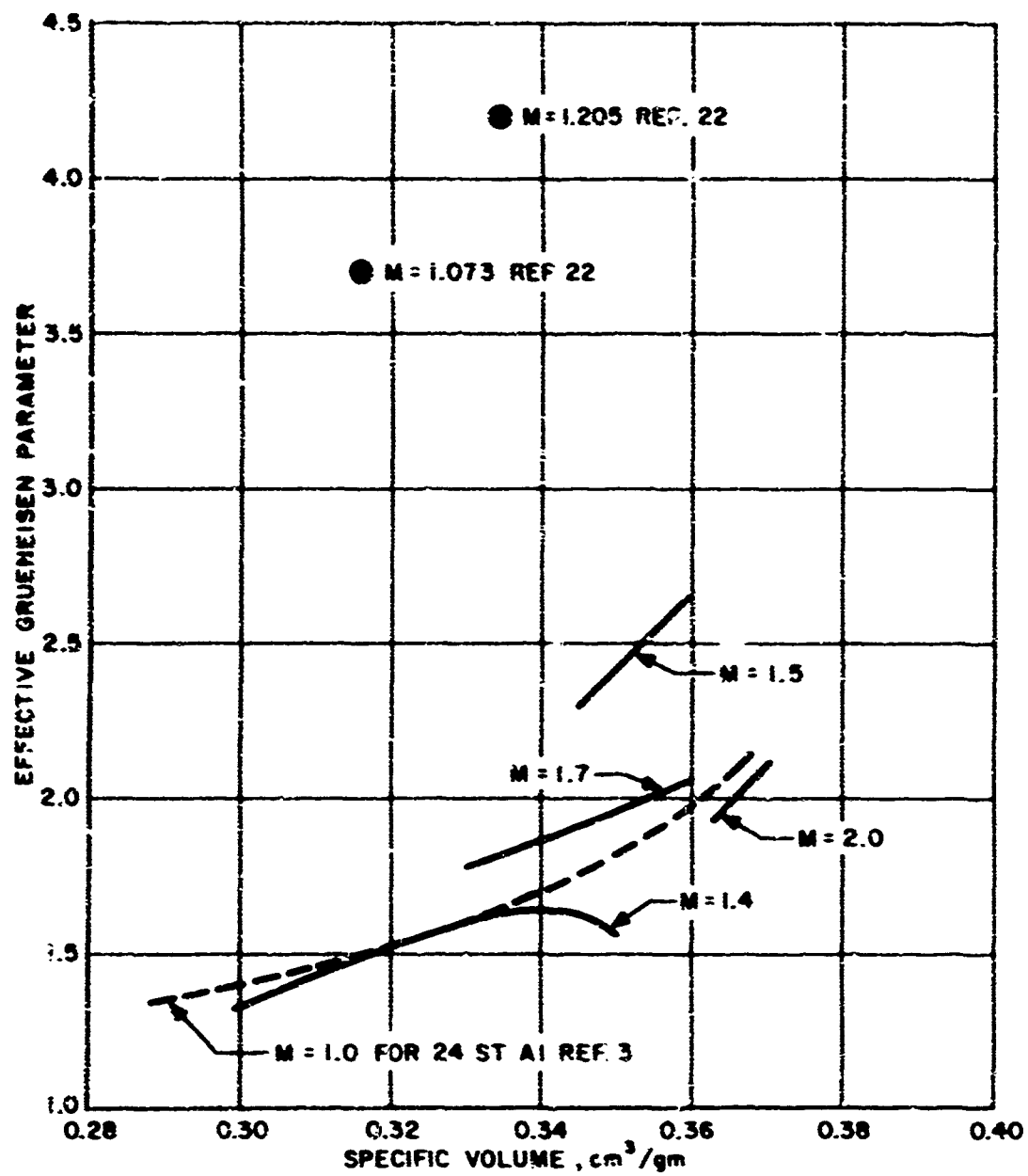


Figure 41. Effective Grueneisen Parameter for Aluminum

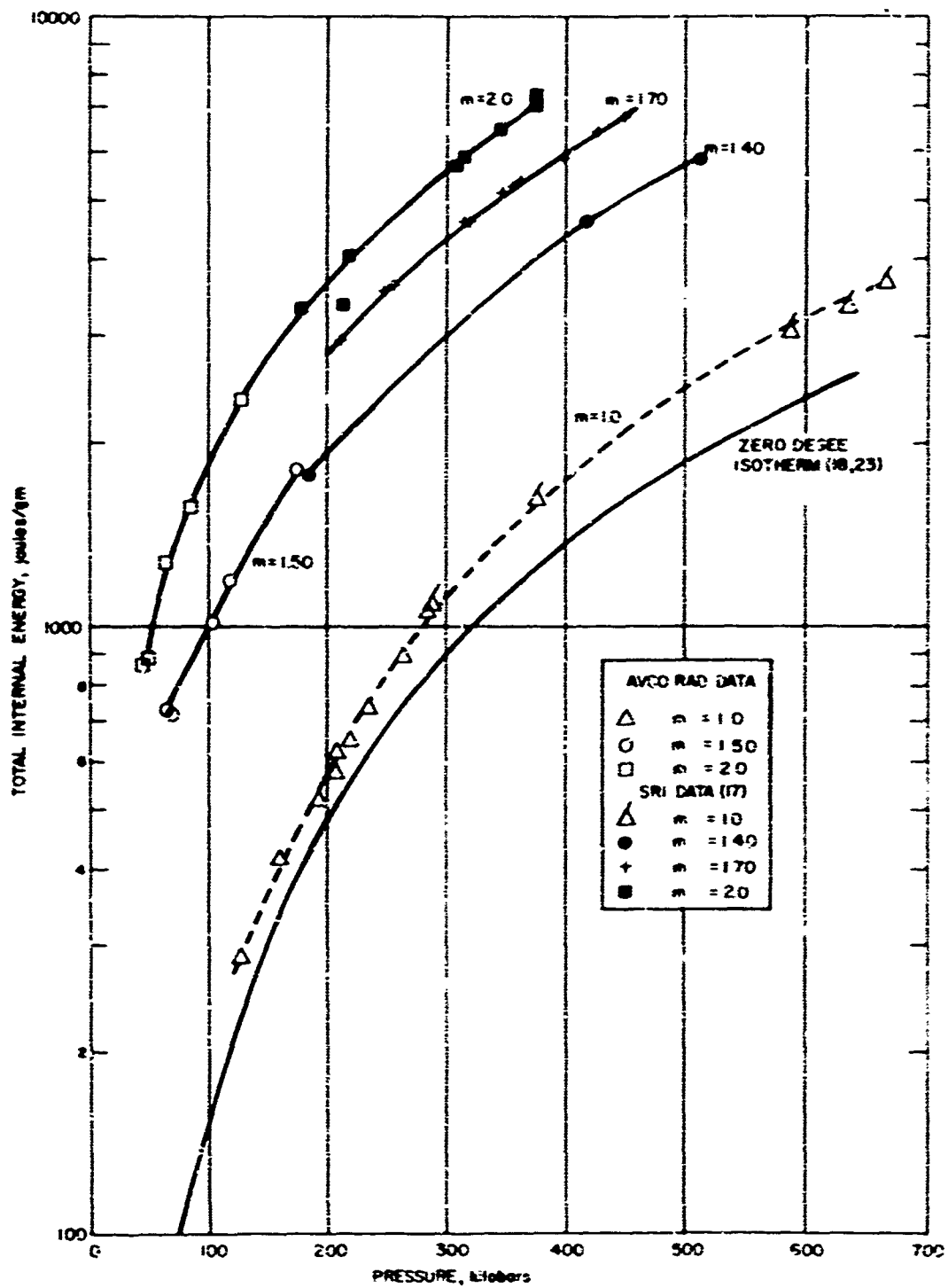


Figure 42. Internal Energy as Function of Pressure for Aluminum

This determined $VP_{th} = V(P - P_0)$.

c. From figure 43, the internal energies, E and E_0 , corresponding to P and P_0 were read on the corresponding porous and zero isotherm curves respectively. This determined $E_{th} = E - E_0$.

The results of the calculation for the three porosities for aluminum are given in figure 43, which is a plot of E_{th} versus VP_{th} . It is apparent that the calculated points can be well-represented by one smooth curve as shown, in agreement with the results of Krupnikov¹ for tungsten. The solid curve plotted is represented by the following equation:

$$E_{th} = 39.9 (VP_{th}) + 0.142 (VP_{th})^2 \quad (56)$$

where E_{th} is in joules/gram and VP_{th} in $(cm^3 \text{ kilobars})/gm$. The relationship for the Grueneisen parameter is thus (with a conversion factor of $1 cm^3$ -kilobar = 100 joules)

$$\Gamma = \frac{100}{39.9 + 0.284 (VP_{th})} \quad (57)$$

with units on VP_{th} as above. In figure 44, a plot is given of the Grueneisen parameter as a function of E_{th} .

Recent data obtained by SRI (ref 17) at a porosity of $m=1.40$ did not agree with the correlation presented, and this suggests the need for additional work on aluminum. An indication of the discrepancy between the correlation and the data obtained by SRI can be observed in figure 39, where for a porosity of $m=1.40$, a calculated Hugoniot is presented along with a curve through the experimental points. The method of calculation was the following:

- From figure 43, choose a point E_{th} , VP_{th} on the curve.
- Assume a value of V
- From figure 39, determine P_0 from the zero degree isotherm.
- From figure 42, determine E_0 .

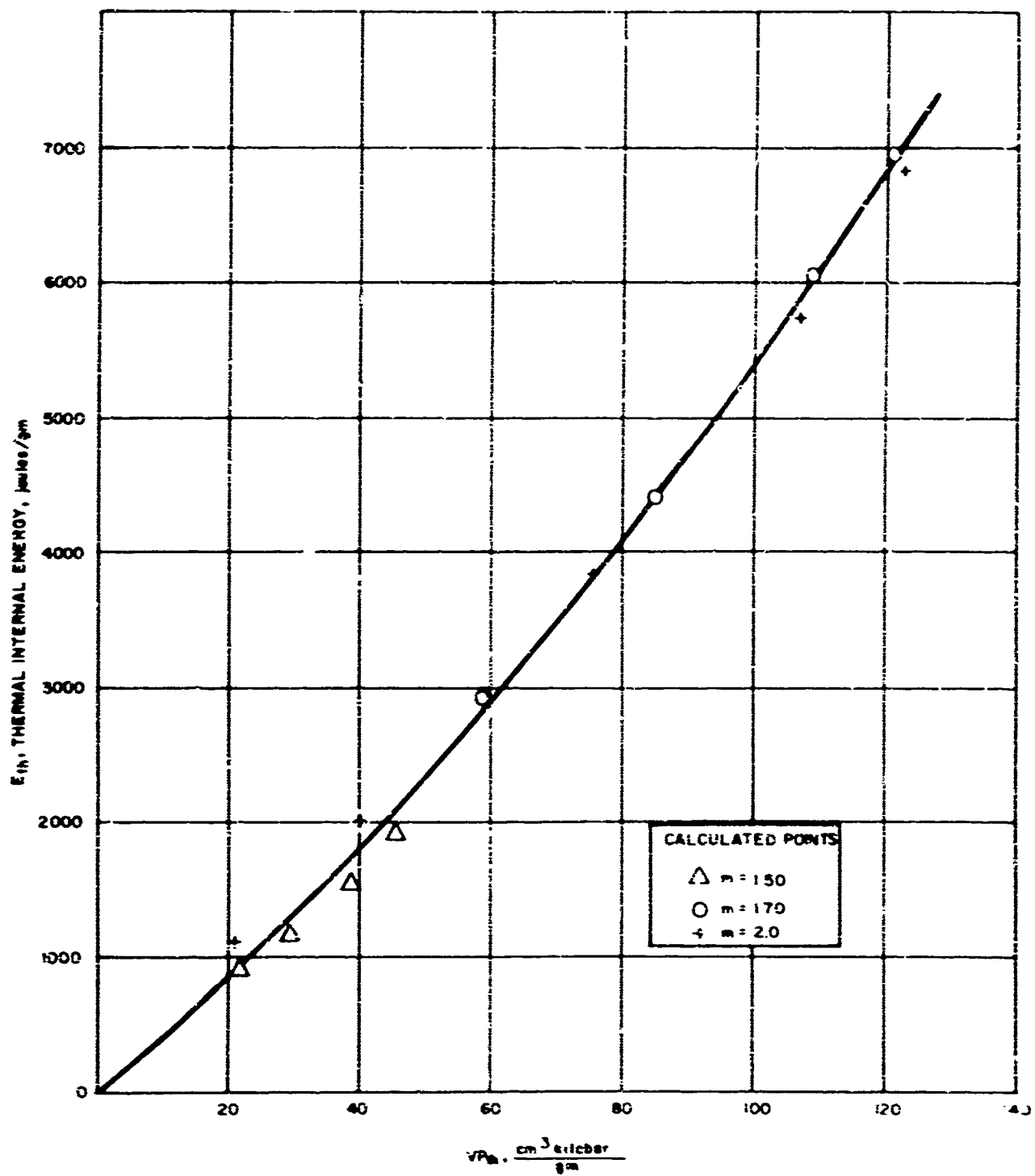


Figure 43. Thermal Internal Energy, E_{th} , Versus v , for Aluminum

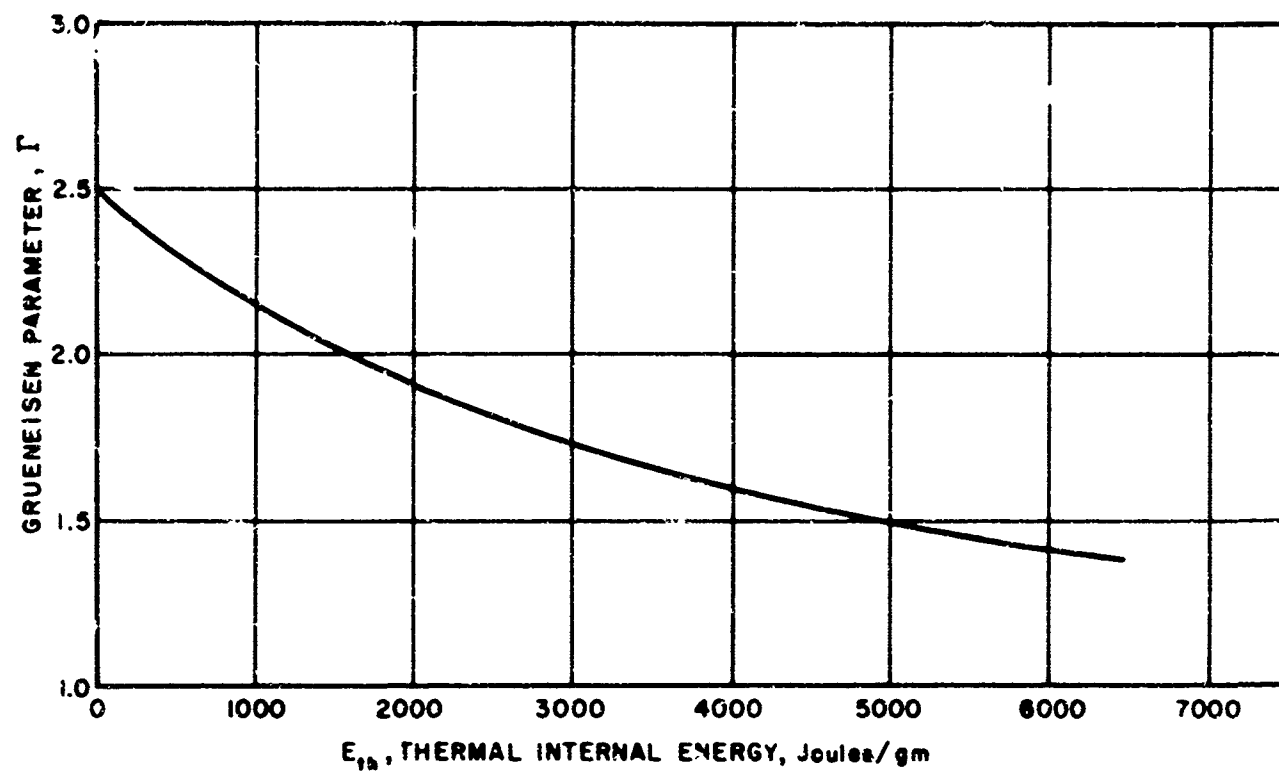


Figure 44. Grueneisen Parameter as Function of Thermal Internal Energy for Aluminum

- e. Knowing E_{th} and E_0 , E can be determined, since $E = E_{th} + E_0$. This value of E must be reduced by 166 joules/gm to convert to the same reference state.
- f. The assumption is made, and this can be verified by inspecting figures 39, 42, and 43 that over the range of specific volumes of interest, $0.30 \leq v \leq 0.367$, the total internal energy is relatively insensitive to changes in volume, and one can use as a good approximation, the experimental curve of E versus P for $m = 1.40$ in figure 42, as a basis for determining the calculated P .
- g. Determine P_{th} from P and P_0 , since $P_{th} = P - P_0$.
- h. Determine VP_{th} and compare it with the value chosen originally
- i. If the obtained value of VP_{th} disagrees with that chosen, repeat the iteration until agreement is obtained.

For Teflon, a detailed analysis such as that presented above for aluminum is not feasible due to the limited quantity of data available as well as the large scatter of the data for porous Teflon. Using the dotted curve of figure 40 and equation (51), an effective Grueneisen parameter was calculated and is presented in figure 45. The accuracy of figure 45 is highly questionable, however, until more data are obtained.

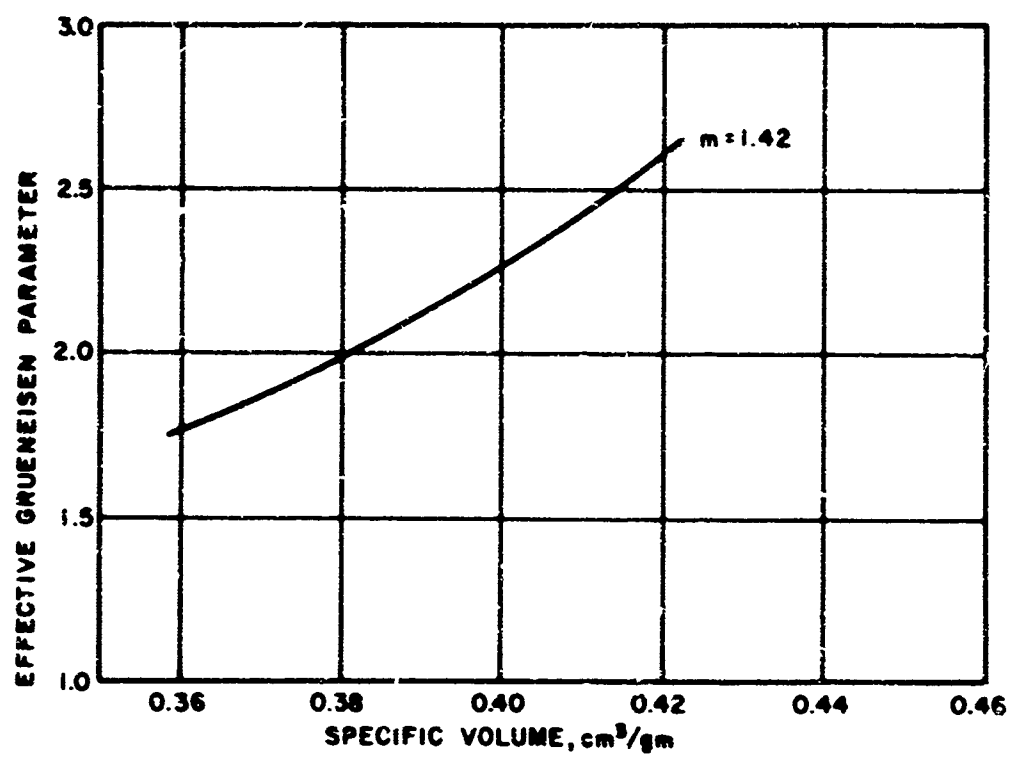


Figure 45. Effective Grueneisen Parameter for Teflon

SECTION VII

CONCLUSIONS AND RECOMMENDATIONS

1. The experimental technique developed at Avco RAD using the laser beam and photomultipliers works satisfactorily for Hugoniot measurements. The powder and light gas guns have been used in the present work to accelerate projectiles to velocities in the range of 1 to 3.5 km/sec and have the potential for velocities up to 6 km/sec. Development work on the gas-leakage problem is required for the higher velocities however.
2. The use of Hugoniot measurements on porous as well as solid samples of a material is an excellent technique of experimentally varying the internal energy in shock-compressed materials for equation of state measurements.
3. The data obtained by Avco RAD and SRI on aluminum is consistent and meshes well together. For porosities of $m = 1.5$, 1.7 and 2.02 , the Grueneisen parameter is dependent only on the thermal component of the internal energy within the accuracy of the data. A discrepancy exists between this correlation and some recent data obtained by SRI at a porosity of $m = 1.40$. It is thus recommended that additional data be taken at this porosity to verify whether the correlation holds.
4. Additional data on Teflon as well as other polymeric materials should be emphasized in future work since much less is known about these materials than for most metals and they are of prime interest in weapon studies.

REFERENCES

1. Krupnikov, K. K., et al., "Shock Compression of Porous Tungsten," Soviet Physics, JETP, 15, No. 3 (September 1962).
2. Kormer, S. B., et al., "Dynamic Compression of Porous Metals and the Equation of State with Variable Specific Heat at High Temperatures," Soviet Physics, JETP, 15, No. 3 (September 1962).
3. Rice, M. H., R. G. McQueen, and J. M. Walsh, "Compression of Solids by Strong Shock Waves, Solid State Physics, 6, Academic Press, Inc., New York, (1958).
4. Poczatek, J. J., A Theoretical Study of Response of Solids to Impulsive Loads of High Pressure, AFSWC-TDR-62-5 (November 1962)
5. Zener, C., Elasticity and Anelasticity of Metals, U. of Chicago (1948)
6. Bada, W. L., "Overtaking of Shock by Rarefaction Head in Plate-Slap Experiments," Technical Release to D. T. Morgan, Avco RAD (25 October 1962)
7. Walsh, J. M., M. H. Rice, R. G. McQueen, and F. L. Yargen, Physical Review, 108, 196 (1957)
8. Charters, A. C., B. P. Denardo, and V. J. Rossow, Development of a High Velocity Free Flight Launcher - The Ames Light Gas Gun, NACA RM A55G11, (December 28, 1955), Confidential
9. Baer, P. G. and H. C. Smith, "Experimental and Theoretical Studies on the Interior Ballistics of Light Gas Guns," Proc. of 6th Symp. on Hypervelocity Impact, Vol. 1 (August 1963).
10. MacCormack, R. W., "Investigation of Impact Flash at Low Ambient Pressures," Proc. of 6th Hypervelocity Impact Symposium, Vol. II Pt. 2, (August 1963)

11. Gehring, J. W., and R. L. Warnica, "An Investigation of the Phenomena of Impact Flash and its Potential Use as a Hit Detection and Target Discrimination Technique," Proc. of 6th Hypervelocity Impact Symposium, Vol. II, Part 2, (August 1963)
12. Hull, J. A. and G. A. Theophanis, "Ballistic Range Applications of Millimicrosecond Photography," JSMPTE 69, 5, 355-357 (May 1960)
13. Theophanis, G. A., "Millimicroseconds Triggering of High Velocity Spark Gaps," Rev. of Sci. Inst., Vol. 31, 4, 427-432 (April 1960)
14. Morgan, D. T. et al, Optimizing Reentry Vehicle Materials to a High Altitude Nuclear Effect (U), Avco RAD-TR-63-27, Vol. I & II (July 1963)
15. Herring, C., Jour. of App. Phys. 21, 1950, pp. 301-303
16. Miller, C. D., JSMPTE, 53, 479-88 (November 1949)
17. Anderson, G.D. et al, AFWL TR65-147 (Sepr. 65)
18. Altshuler, L. V., et al., "Equation of State for Aluminum, Copper, and Lead in the High Pressure Region," Soviet Physics JETP, Vol. II No. 3 p. 573, (September 1960)
19. Fowles, G. R., and Curran, D. R., Experimental Testing of Shock Attenuating Materials. AFSWC-TDR-62-22, (March 1962)
20. Wagner, M. H., W. F. Waldorf, Jr., and N. A. Louis, Determination of Hugoniot Equations of State for Polymers and Reentry Vehicle Materials and Investigations of Fracture Phenomena, Vol. I and II AFSWC-TDR-62-66, (August 1962)
21. Bridgman, P. W., Proc. Am. Acad. Arts Sci, 76, 71 (1948), as reported in American Institute of Physics Handbook, McGraw-Hill Book Company, Inc., New York, (1957)

22. Adler, B. J., "Physics Experiments with Strong Pressure Pulses,"
Solids Under Pressure, editors W. Paul and D. M. Warschauer,
McGraw-Hill Book Company, Inc., (1963)
23. McCloskey, D. J., "An Analytic Formulation of Equations of State,"
Memorandum RM-3905-PR, Rand Corporation, (February 1964)

Unclassified

Security Classification

DOCUMENT CONTROL DATA - R&D		
(Security classification of title, body of abstract and index and abstract must be entered when the report is classified)		
1. ORIGINATING ACTIVITY (Corporate author) Research and Advance Development Division AVCO Corporation Wilmington, Massachusetts		2a. REPORT CLASSIFICATION <u>Unclassified</u> 2b. GROUP
3. REPORT TITLE MEASUREMENT OF THE GRUENEISEN PARAMETER AND THE INTERNAL ENERGY DEPENDENCE OF THE SOLID EQUATION OF STATE FOR ALUMINUM AND TEFLON		
4. DESCRIPTIVE NOTES (Type of report and inclusive dates) Final Report 1 May 1964 to 31 May 1965		
5. AUTHOR(S) (Last name, first name, initial) Morgan, D. T.; Rockowitz, M.; and Atkinson, A. L.		
6. REPORT DATE September 1965	7a. TOTAL NO. OF PAGES 128	7b. NO. OF REFS 23
8a. CONTRACT OR GRANT NO. AF 29(601)-6394	9a. ORIGINATOR'S REPORT NUMBER(S) AFWL-TR-65-117	
b. PROJECT NO. 5710	9b. OTHER REPORT NO(S) (Any other numbers that may be assigned this report)	
c. Subtask 15.018	AVCO RAD-TR-65-24	
d.		
10. AVAILABILITY/LIMITATION NOTICES Defense Documentation Center release to Clearinghouse for Scientific and Technical Information is authorized.		
11. SUPPLEMENTARY NOTES	12. SPONSORING MILITARY ACTIVITY Air Force Weapons Laboratory (WLRPX) Kirtland Air Force Base, New Mexico	
13. ABSTRACT Experimental measurements of the solid state equation of state of aluminum and Teflon, including the internal energy dependence, were made. The data for aluminum mesh well with the data of other investigators. Using the aluminum data, it was found that for initial aluminum densities of 1.36, 1.60, and 1.82 gms/cc, the thermal internal energy, E_{th} , is dependent only on the product VP_{th} where V is the specific volume and P_{th} is the thermal pressure. The Grueneisen parameter was found to be given by $100/(39.9 + 0.284 VP_{th})$ with VP_{th} in $(cm^3 \text{ kilobars})/gm$. At $VP_{th} = 0$, the Grueneisen parameter = 2.5. The solid Hugoniot for Teflon was found to mesh well with lower pressure measurements by other investigators. The scatter in the porous Teflon samples was too large and the data were too limited to permit evaluation of the Grueneisen parameter.		

14	KEY WORDS	LINK A		LINK B		LINK C	
		ROLE	WT	ROLE	WT	ROLE	WT
	Equation of State Mie- Gruneisen Equation of State Gruneisen Parameter Hugoniot Aluminum Equation of State Teflon Equation of State High Pressure Equation of State						

INSTRUCTIONS

1. **ORIGINATING ACTIVITY:** Enter the name and address of the contractor, subcontractor, grantee, Department of Defense activity or other organization (*corporate author*) issuing the report.

2a. **REPORT SECURITY CLASSIFICATION:** Enter the overall security classification of the report. Indicate whether "Restricted Data" is included. Marking is to be in accordance with appropriate security regulations.

2b. **GROUP:** Automatic downgrading is specified in DoD Directive 5200.10 and Armed Forces Industrial Manual. Enter the group number. Also, when applicable, show that optional markings have been used for Group 3 and Group 4 as authorized.

3. **REPORT TITLE:** Enter the complete report title in all capital letters. Titles in all cases should be unclassified. If a meaningful title cannot be selected without classification, show title classification in all capitals in parenthesis immediately following the title.

4. **DESCRIPTIVE NOTES:** If appropriate, enter the type of report, e.g., interim, progress, summary, annual, or final. Give the inclusive dates when a specific reporting period is covered.

5. **AUTHOR(S):** Enter the name(s) of author(s) as shown on or in the report. Enter last name, first name, middle initial. If military, show rank and branch of service. The name of the principal author is an absolute minimum requirement.

6. **REPORT DATE:** Enter the date of the report as day, month, year, or month, year. If more than one date appears on the report, use date of publication.

7a. **TOTAL NUMBER OF PAGES:** The total page count should follow normal pagination procedures, i.e., enter the number of pages containing information.

7b. **NUMBER OF REFERENCES:** Enter the total number of references cited in the report.

8a. **CONTRACT OR GRANT NUMBER:** If appropriate, enter the applicable number of the contract or grant under which the report was written.

8b, 8c, & 8d. **PROJECT NUMBER:** Enter the appropriate military department identification, such as project number, subproject number, system numbers, task number, etc.

9a. **ORIGINATOR'S REPORT NUMBER(S):** Enter the official report number by which the document will be identified and controlled by the originating activity. This number must be unique to this report.

9b. **OTHER REPORT NUMBER(S):** If the report has been assigned any other report numbers (*either by the originator or by the sponsor*), also enter this number(s).

10. **AVAILABILITY/LIMITATION NOTICES:** Enter any limitations on further dissemination of the report, other than those

imposed by security classification, using standard statements such as:

- (1) "Qualified requesters may obtain copies of this report from DDC."
- (2) "Foreign announcement and dissemination of this report by DDC is not authorized."
- (3) "U. S. Government agencies may obtain copies of this report directly from DDC. Other qualified DDC users shall request through _____."
- (4) "U. S. military agencies may obtain copies of this report directly from DDC. Other qualified users shall request through _____."
- (5) "All distribution of this report is controlled. Qualified DDC users shall request through _____."

If the report has been furnished to the Office of Technical Services, Department of Commerce, for sale to the public, indicate this fact and enter the price, if known.

11. **SUPPLEMENTARY NOTES:** Use for additional explanatory notes.

12. **SPONSORING MILITARY ACTIVITY:** Enter the name of the departmental project office or laboratory sponsoring (*paying for*) the research and development. Include address.

13. **ABSTRACT:** Enter an abstract giving a brief and factual summary of the document indicative of the report, even though it may also appear elsewhere in the body of the technical report. If additional space is required, a continuation sheet shall be attached.

It is highly desirable that the abstract of classified reports be unclassified. Each paragraph of the abstract shall end with an indication of the military security classification of the information in the paragraph, represented as (TS), (S), (C), or (U).

There is no limitation on the length of the abstract. However, the suggested length is from 150 to 225 words.

14. **KEY WORDS:** Key words are technically meaningful terms or short phrases that characterize a report and may be used as index entries for cataloging the report. Key words must be selected so that no security classification is required. Identifiers, such as equipment model designation, trade name, military project code name, geographic location, may be used as key words but will be followed by an indication of technical context. The assignment of links, rules, and weights is optional.